NEI-NO--963

NO9805456

RECEIVED
DEC 22 1998
OSTI

Vidar Mathiesen

An experimental and computational study of multiphase flow behavior in circulating fluidized beds

MASTER

NTNU Trondheim
Norges teknisk-naturvitenskapelige
universitet

Doktor ingeniøravhandling 1997:81
Høgskolen i Telemark

DISTRIBUTION OF THIS DOCUMENT IS UNLIMITED
FOREIGN SALES PROHIBITED
al

AN EXPERIMENTAL AND COMPUTATIONAL STUDY OF MULTIPHASE FLOW BEHAVIOR IN CIRCULATING FLUIDIZED BEDS

by

VIDAR MATHIESEN

Department of Process Technology (IPT)
Telemark Institute of Technology (HiT-TF)
Kjølnes Ring, N-3914 Porsgrunn
NORWAY

Thesis submitted to
Norwegian University of Science and Technology (NTNU)
for the degree of Dr. Ing.

Porsgrunn, June 1997

ABSTRACT

An experimental and computational study of flow behavior in gas/solids circulating fluidized beds are performed. In gas/solids systems, the particle diameter and particle size distributions are among the most essential parameters controlling the flow behavior and a special emphasis is given to study these effects and their influences on the flow pattern.

An experimental study has been performed at two different circulating fluidized bed systems. LDA and PDA techniques are used to measure mean and fluctuating velocity, diameter and solids concentration. A typical core-annulus flow is obtained in both circulating fluidized beds. The measurements show a relative mean velocity as well as a relative fluctuating velocity between different particle sizes. An axial segregation by size and its variation with the superficial gas velocity are demonstrated. Also a significant radial segregation is measured in both risers. A behavior which has apparently not been observed or reported in earlier studies.

A three-dimensional Computational Fluid Dynamics (CFD) model has been developed based on earlier works at Telemark Institute of Technology. The model is based on an Eulerian description of the phases where the kinetic theory for granular flow forms the basis for the turbulence modelling in the solids phases. The model is generalized for one gas phase and *N* number of solids phase to enable a realistic description of particle size distributions and a non-uniform diameter distribution in gas/solids systems. Each solids phase is characterized by a diameter, form factor, density and restitution coefficient. The granular temperature and momentum equations are solved for each phase.

The flow behavior in three different circulating fluidized bed systems have been computed. Both two and three-dimensional geometry descriptions are considered. The simulations show altogether good agreements with experimental data. Typical core-annulus flow is computed in all three risers. Relative velocities, volume fractions and fluxes are predicted fairly well. It is shown that the model is able to handle axial segregation by size for different superficial gas velocities and particle size distributions.

Discussions and analyzes of the experimental as well as the computational results are conducted. The experimental observations together with the computed results should increase the depth of understanding of the underlying mechanisms.

ACKNOWLEDGEMENTS

This work has been carried out at Telemark Technological Research and Development Centre (Tel-Tek) and Department of Process Technology, Telemark Institute of Technology (HiT-TF) under the supervision of professor Bjørn H. Hjertager.

First of all I would like to thank professor Bjørn H. Hjertager, his guidance and interesting discussions throughout this work are gratefully acknowledged. I would also like to express my gratitude to my colleagues at Tel-Tek and HiT, and especially senior scientist Dr. Tron Solberg for his useful help and advice. Interesting discussions with Dr. Eirik Manger and Dr. Ing. student Trond Solbakken are also acknowledged.

Many thanks also goes to professor Hamid Arastoopour and his co-workers at Illinois Institute of Technology (IIT), Department for Chemical and Environmental Engineering, with whom I had the pleasure of working with during the autumn of 1996. Special thanks to Dr. Michael S. Shao for his help and advice during my LDA measurements at IIT.

This work has been sponsored by the Norwegian Research Council (NFR).

Finally, very special thanks to Gro Irene for her patience, encouragement and moral support. I would also like to thank my mother and father for their support.

June, 1997 Vidar Mathiesen

TABLE OF CONTENTS

ABSTRACT I
ACKNOWLEDGEMENTS II
TABLE OF CONTENTS III
NOMENCLATURE VI

1 INTRODUCTION 1
  1.1 Motivation 1
  1.2 A Short Overview of Previous Work 3
    1.2.1 Experimental Work with LDA and PDA in Gas/Solids Systems 3
    1.2.2 Modelling of Gas/Solids Flow Systems 4
  1.3 Outline of Thesis 6

2 LASER AND PHASE DOPPLER ANEMOMETRY 8
  2.1 Particle Velocity Measurement 9
  2.2 Particle Size Measurement 10
    2.2.1 Shape Discrimination Technique 10
    2.2.2 Phase Doppler Anemometry 15
  2.3 Particle Concentration Measurement 16

3 GOVERNING EQUATIONS IN MULTIPHASE GAS/SOLIDS MODEL 17
  3.1 Transport Equations 18
    3.1.1 Continuity Equations 18
    3.1.2 Momentum Equations 18
    3.1.3 Turbulent Kinetic Energy Equations 21
  3.2 Consistency of the Multiphase Model 22
    3.2.1 Single Solids Phase 23
    3.2.2 Two Identical Solids Phases 24

4 NUMERICAL ALGORITHMS AND SOLUTION PROCEDURE 26
  4.1 Numerical Scheme 26
    4.1.1 Convective Term 27
    4.1.2 Diffusive Term 27
    4.1.3 Source Term 27
    4.1.4 Transient Scheme 27
  4.2 Initial Conditions 28
  4.3 Boundary Conditions 28
    4.3.1 Symmetry Boundaries 28
    4.3.2 Wall Boundaries 28
    4.3.3 Inlet and Outlet Boundaries 29
  4.4 Multiphase Solution Algorithm 29

4.5 Solving Algebraic Equations 30
4.6 Solution Procedure 30
4.7 Computer Code Outline 30

5 AN EXPERIMENTAL AND COMPUTATIONAL STUDY OF A 0.032 m I.D. CFB 33
5.1 Experimental Setup 33
5.1.1 Circulating Fluidized Bed 33
5.1.2 Laser and Phase Doppler Anemometry 34
5.2 Numerical Flow Parameters, Initial and Boundary Conditions 35
5.3 Experimental and Numerical Results 37
5.3.1 Particle Diameter Profiles 37
5.3.2 Volume Fraction Profiles 42
5.3.3 Particle Velocity Profiles 45
5.3.4 Fluctuating Particle Velocity 48
5.4 Dependence of Flow Parameters 52
5.4.1 Particle-Wall Conditions 52
5.4.2 Restitution Coefficient 56
5.5 Summary 58

6 2D MODELLING OF A PILOT SCALE CFB 59
6.1 Experimental Setup 59
6.2 Numerical Flow Parameters, Initial and Boundary Conditions 60
6.3 Numerical Results 62
6.3.1 Temporal Evolutions 62
6.3.2 Mean Diameter Profiles 65
6.3.3 Velocity Profiles 66
6.3.4 Particle RMS Velocity Profiles 70
6.3.5 Mass Flux Profiles 72
6.4 Summary 74

7 AN EXPERIMENTAL AND COMPUTATIONAL STUDY OF A 2" I.D. RISER 75
7.1 Experimental Setup 75
7.1.1 Circulating Fluidized Bed 75
7.1.2 Laser Doppler Anemometry 76
7.2 Numerical Flow parameters, Initial and Boundary Conditions 77
7.3 Experimental and Numerical Results 79
7.3.1 Particle Diameter Calibration Curves 79
7.3.2 Particle Diameter Profiles 82
7.3.3 Particle Velocity Profiles 84
7.3.4 RMS Velocity Profiles 88
7.4 Summary 91

8 3D MODELLING OF A PILOT SCALE RISER 92
8.1 Numerical Flow Parameters, Initial and Boundary Conditions 92
8.2 Numerical Results 93
8.2.1 Volume Fraction 93
8.2.2 Particle Velocity 97
8.2.3 Particle RMS Velocity 101
8.2.4 Comparison of 2D and 3D 103
8.3 Summary 104

9. CONCLUSIONS AND RECOMMENDATIONS 106
9.1 Conclusions 106
9.2 Recommendations for Further Work 110

REFERENCES 111

NOMENCLATURE

A_D	-	amplitude of a Doppler burst	[V]
A_{D0}	-	amplitude of a Doppler burst in center of a measuring volume	[V]
a	-	coefficient in discretization equation	[ ]
b	-	constant term in discretization equation	[ ]
b_0	-	dimension in direction perpendicular to optical axis	[m^2]
C	-	Courant number	[-]
C_d	-	drag coefficient	[-]
c	-	instantaneous particle velocity	[m/s]
c_t	-	constant in Sub Grid Scale model	[-]
D_i	-	particle diameter	[m]
D_{Number}	-	number averaged particle diameter	[m]
D_{Volume}	-	volume averaged particle diameter	[m]
d	-	particle diameter	[m]
d_{sn}	-	mean particle diameter $=\frac{1}{2}(d_s+d_n)$	[m]
e	-	restitution coefficient	[-]
e_{sn}	-	mean restitution coefficient $=\frac{1}{2}(e_s+e_n)$	[-]
F	-	sum of forces acting on a particle per unit mass	[N/kg]
f	-	single particle velocity distribution function	[-]
f_D	-	Doppler frequency	[Hz]
f_l	-	focal length of transmitting lens	[m]
g_j	-	j-direction component of gravity	[m/s^2]
g_0	-	radial distribution function for a single solids phase	[-]
g_{sn}	-	binary radial distribution function	[-]
I	-	intensity	[V]
I_0	-	intensity in center of a measuring volume	[V]
K	-	optical constant	[-]
l	-	length of the traveling path for a particle through a measuring volume	[m]
l	-	mean free path	[m]
l_{max}	-	maximum length of path a particle may have to travel	[m]
M	-	number of phases	[-]
m	-	mass of a particle	[kg]
m_0	-	$m_s + m_n$	[kg]
N	-	number of solids phases	[-]
$N_{Doppler}$	-	number of Doppler bursts	[-]
N_i	-	number of measured particles	[-]
N_{peak}	-	number of peaks within one Doppler burst	[-]
$N_{peak,max}$	-	maximum number of peaks within one Doppler burst	[-]
n	-	number of particles	[m^{-3}]
P	-	fluid pressure	[Pa]
P_C	-	collisional pressure	[Pa]
P_s	-	solid phase pressure	[Pa]

q	-	collisional heat flux	[kg/s^3]
R	-	radius of a tube	[m]
r	-	radius, coordinate in radial direction	[m]
Re	-	Reynolds number	[-]
S	-	scaling factor	[-]
S	-	source term	[ ]
S_C	-	constant part of source term	[ ]
S_P	-	coefficient of variable part of source term	[ ]
S_{ij}	-	rate of deformation tensor	[m/s^2]
T_{Sample}	-	sampling time period	[s]
t	-	time	[s]
U_i, U_j	-	*i* and j-components of velocity	[m/s]
u_{rs}	-	terminal velocity correlation for phase *s*	[-]
$\vec{u}$	-	velocity vector	[m/s]
V	-	mean particle velocity	[m/s]
V_{focus}	-	volume of measuring volume	[m^3]
V_{RMS}	-	root mean square velocity	[m/s]
V_{SUP}	-	superficial gas velocity	[m/s]
v_i	-	measured particle velocity	[m/s]
x	-	coordinate in x-direction	[m]
y	-	coordinate in y-direction	[m]
z	-	coordinate in z-direction	[m]

Greek letters:

α	-	volume fraction	[-]
$\alpha_{s,\max}$	-	maximum total volume fraction of solids	[-]
β_i	-	area porosity in *i*-direction	[-]
β_v	-	volume porosity	[-]
γ	-	collisional energy dissipation	[kg/ms^3]
Γ	-	general diffusion coefficient	[kg/ms]
ΔL	-	distance between two photo detectors	[m]
Δx	-	*x*-direction width of a control volume	[m]
δx	-	*x*-direction distance between two adjacent grid points	[m]
Δy	-	*y*-direction width of a control volume	[m]
Δz	-	*z*-direction width of a control volume	[m]
Δt	-	time step	[s]
$\overline{\Delta\tau}$	-	average time duration for a period in a Doppler burst	[s]
$\Delta\tau_k$	-	time duration for k-th period in a Doppler burst	[s]
δ_f	-	fringe spacing	[m]
δ_{ij}	-	Kroenecker delta	[-]
θ	-	granular temperature $=\frac{1}{3}<C_s^2>$	[m^2/s^2]
ϑ	-	angle between two incident laser beams	[°]

κ	-	transport coefficient of granular temperature	[kg/ms]
μ	-	shear viscosity	[kg/ms]
λ	-	wavelength	[m]
ξ	-	bulk viscosity	[kg/ms]
Π_{ij}	-	stress tensor, solids phase	[kg/ms^2]
π	-	3.14159265	[-]
ρ	-	density	[kg/m^3]
σ	-	standard deviation	[]
τ_i	-	time duration for one Doppler burst	[s]
$\tau_{ij,g}$	-	stress tensor, gas phase	[kg/ms^2]
Φ	-	drag coefficient	[kg/m^{3}s]
ϕ	-	phase difference	[°]
ϕ	-	general dependent variable	[ ]
ψ	-	particle form factor	[-]
ω	-	specularity factor	[-]

Subscript:

av	-	average
col	-	collisional
cor	-	correction
dil	-	dilute
e	-	east control volume face
eff	-	effective
g	-	gas phase
i,j	-	i and j-direction respectively
kin	-	kinetic
lam	-	laminar
m	-	gas phase or solids phase *m*
max	-	maximum
min	-	minimum
n	-	solids phase n
nb	-	neighbor points
P,E,W,N,S,T,B	-	main grid points, central, east, west, north, south, top and bottom, respectively
RMS	-	Root Mean Square
s	-	solids phase s
SUP	-	superficial
turb	-	turbulent
U1,U2,U3	-	photo detectors, number 1, 2 and 3 respectively
w	-	wall
1	-	solids phase number *1*
2	-	solids phase number *2*
ϕ	-	general dependent variable

CHAPTER 1

INTRODUCTION

Winkler introduced the fluidized bed technique in the gasification of lignite as early as 1926, Jahing et al. (1980) and Squires (1986). The size of the first commercial large scale unit was 13 meter high and had a cross section area of 12 m^2, and was fed with powdered coal. After that a number of fluidized beds were constructed primarily in Japan and Germany, but also in the rest of Europe and USA. Around 1940, due to the World War II, the motivation for further development was the need for vast quantities of high-octane aviation gasoline. This led to the Thermofor Catalytic Cracking (TCC) process. The system consists of a reactor regenerator circuit which was using two moving beds of catalyst solids and transported from unit to unit by bucket elevator or gas lift. At the same time researchers at Standard Oil Company in New Jersey, USA developed a pneumatic transport system for the solids. Finally, both the generator and the regenerator were operated under transport conditions. It was later found that the dense mixtures of solids and gas behaved in many aspects like a fluid, and this made the control of streams much more convenient. This was the start of Fluid Catalytic Cracking (FCC). In 1962 Mobil developed a new type of catalyst, high activity zeolite, and this was the real breakthrough for the fluidized bed technology.

Although fluidized beds originally came from the petroleum industry, they are also used in numerous other applications where solids have to be handled. Examples are roasting of ores and in catalytic reactors for highly exothermic reactions, where the high turbulence created by the gas/solids flow leads to much higher heat transfer coefficients than in fixed beds. Thus fluidized bed reactors are widely used in exothermic processes requiring close temperature control such as oxidation of naphthalene into phthalic anhydride, amoxidation of propylene into acrylonitrile, oxychlorination of ethylene into ethylene dichloride, Froment and Bischoff (1990).

Another important application of fluidized bed is combustion of coal, which is less suited for conventional boilers. Fluidized beds are also widely used in drying of solids, coating and growth of solids and in environmental engineering.

1.1 Motivation

The subject of gas/solids flow has for several decades been studied quite extensively, mainly because of its important applications in nuclear, chemical and petroleum industries. Recently experimental observations of the flow behavior have increased the depth of understanding of the underlying mechanisms, which in turn has provided the basis for improved field information of the basic conservation equations and constitutive laws for gas/solids flow systems.

Although fluidized beds are successfully and widely used in commercial industrial operations, much remains to be done due to the complexity of the gas/solids flow. In order to gain fundamental knowledge about the complex multiphase flow behavior, much research is still needed. Furthermore the design and operation of fluidized beds and transport reactors are by no means a simple task, particularly when the circulation of solids is involved. Several books have been published on the subject, Zenz and Othmer (1960), Davidson and Harrison (1963), De Groot (1967), Angelino et al.

(1974), Froment and Bischoff (1990) and Kunii and Levenspiel (1991).

Numerous factors are influencing the flow behavior in a circulating fluidized bed. The complex geometry, the particle size and distribution, the velocity distribution of the gas as well as the solids, variation of concentrations, pressure and velocity fluctuations, effective viscosity and agglomeration of particles are probably some of the main reasons for the flow complexities. The hydrodynamics of gas and solids will again affect the heat transfer, reaction kinetics and catalyst activity.

In gas/solids systems the particle size and distribution are among the most important parameters controlling the flow behavior. Under the same flow condition, particles of different size may have significantly different flow behavior. Thus the objective of this work is to provide a better understanding of the complex flow behavior in gas/solids systems and to investigate the effects of particle size and size distribution on the flow pattern. To limit the research, only dilute gas/solids circulating fluidized beds (CFB) are studied in the present work.

Geldart (1973) classified solids into four types, characterized by the density difference between particles and fluid and by mean particle size. In this work solids classified as group A and B are studied extensively, experimentally as well as numerically. Group A is aeratable solids and materials which have a small mean particle size and/or low particle density (< 1400 kg/m^3). These solids fluidize easily, with smooth fluidization at low gas velocities and controlled bubbling with small bubbles at higher gas velocities, Kunii and Levenspiel (1991). FCC catalysts are representative of these solids. Group B is sandlike and a mean diameter between 40 and 500 μm and a density range from 1400 to 4000 kg/m^3. These solids fluidize well with vigorous bubbling action and bubbles that grow large. Glass particles are typical of these solids.

To get detailed knowledge about the flow behavior of gas/solids systems, experimental work are obviously important. In this area of gas/solids two phase flow, experimental research has been done for over thirty year. Soo et al. (1964) did experiments using optical fibre instrument to measure concentration and electrostatic ball probe to estimate the mass flow distribution. Later Reddy (1967) used stereo photo-grammetry to obtain information about the flow. There have further been done a lot of experimental work with a numerous different techniques. However, almost all of these methods are invasive techniques which disturb the flow.

During the recent years, Laser Doppler Anemometry (LDA) has become one of the most commonly used experimental techniques in dilute gas/solids flow systems. The major reason is that LDA is a non-invasive optical technique which does not disturb the flow. The LDA system has also a high spatial resolution with a fast dynamic response and range. The LDA diagnostic is capable to detect reversal flow and there are no requirement for calibration. In addition to the mean and fluctuating velocity, LDA has the capabilities to measure size and concentration of the dispersed phase.

In this work experimental investigation with Laser Doppler Anemometry and Phase Doppler Anemometry (PDA) are done in two different circulating fluidized bed systems. Axial and radial particle size distributions in the risers are measured. Also mean and turbulent velocity profiles are measured for different sizes of the particles.

During the recent years computer techniques for fluid flow processes have been a well accepted tool. A multiphase three-dimensional Computational Fluid Dynamics (CFD) model is developed, based on the work by Hjertager and Samuelsberg (1992), Samuelsberg (1994) and Manger (1996). The model allows the user to classify the solids into several classes, referred to as different phases. This allows the model to calculate segregation by size, different velocities for different sizes and will obviously give a better understanding of the underlying flow mechanisms. The fluid dynamic model is based on an Eulerian description of the phases. The conservation equations for the solid phases use the kinetic theory for granular flow, e.g. Gidaspow (1994). By comparing the numerical results with data from the literature and own measurements, a verification of the model is possible.

1.2 A Short Overview of Previous Work

Much work has been conducted within both modelling and experimental study of fluidized bed technology and gas/solids flow in general. The intention of this overview is to give a short summary/introduction to experimental work with LDA and PDA techniques and turbulence modelling of gas/solids flow. Goldsmith (1978), Hewitt (1978) and Doeblin (1990) give a summary of different multiphase measurements techniques. Froment and Bischoff (1990) give a complete description of classical hydrodynamic modelling. These two subjects will not be treated further here.

1.2.1 Experimental Work with LDA and PDA in Gas/Solids Systems

As early as 1968 James et al. (1968) reported the first successful measurement with LDA. They were able to measure the velocity of a particle in air. Then followed numerous scientists, e.g. Birchenough et al. (1976), Lee and Srinivasan (1978), Lesinski et al. (1981) and Tsuji et al. (1984). They were all able to estimate the velocity of the dispersed phase in gas/solids systems.

Particle size measurements using laser systems are very challenging. Dunning (1967) was the first to show that LDA could be used to indicate the particle size. He showed that if a number of assumptions were made regarding the spatial and kinetic properties of very small particles, spectral analysis of the signal used in conjunction with Rayleigh-Gans scattering theory would indicate the particle size.

Andrews and Seifert (1971) estimated the particle size by measuring the absolute value of the scattered intensity and correlating this value with a value predicted by using Mie cross-section calculation.

Farmer (1972) analyzed a method for determining particle size, number density and velocity using a laser interferometer/velocity-meter. The method was an extension of the real fringe laser arrangements, a work started by Dunning (1967) and Andrews and Seifert (1971). He showed that when the fringe spacing is comparable to a particle diameter, the size can be estimated and when the fringe spacing is much greater than the average particle diameter, the number density can also be measured. Since the fringe spacing, depending on the optical system, is generally less than 4 μm, the technique is only suitable for very small particles.

Lee and Srinivasan (1978) were the first to extract size information from peak values from a filtered anemometer. At the same time Driscoll and Mann (1978) used the broadening of the optical spectrum of scattered light to estimate the size of their submicron particles. Further into the eighties the most frequently used methods involved the two concept of a doppler signal; pedestals and visibility. Hishida et al. (1984), Grehan et al. (1986) and Berkelman and Renz (1989) are some of the scientists, who have successfully used these techniques.

In the early nineties Yang and Arastoopour (1992) modified a LDA system. Both the hardware configuration and software for data acquisition and processing were changed. The system could estimate the diameter of fine particles, size less than the measuring volume. The research was based on Farmer (1972), Lee and Srinivasan (1978), and the principle that the amplitude of a Doppler burst is proportional to the particle diameter. They found that this proportionality can be obtained by a calibration curve. They named the method "Shape Discrimination Technique". Later Zhang and Arastoopour (1995) followed the work and did successfully measurements of FCC, cohesive and sand particles in the riser of a circulating fluidized bed.

For size measurements of larger particles, Shao and Arastoopour (1995) developed a technique called "Flight Time Technique". The method estimates the particle diameter from the velocity and the time the particle travels through the measuring volume. This is probably the best suitable technique using LDA. To get a good estimate of the diameter, the particle size should be larger than the width of the measuring volume, which is generally larger than 100 μm.

Already in 1975 Durst and Zare (1975) found that there exists a linear relation between the diameter of a spherical particle and the Doppler signals detected at two different points in space. Almost ten years later Saffmann et al. (1984) extended the technique and presented the experimental results on bubble size measurements. Later Bachalo and Houser (1984, 1985) measured simultaneously the droplet size and velocity in nozzle spray flow. The technique is named "Phase Doppler Technique" or often called "Phase Difference Technique", since the phase difference between two points is related linearly to the particle size. PDA has a number of desirable features including a very wide size range, from micron to millimeters, and a good immunity to noise. A big limitation of the method is that the particles have to be smooth and spherical. However many scientists have adopted the method in gas/solids flow as well as in liquid/solids and bubble flow. Lazaro (1991), Tadrist et al. (1993), Azario et al. (1995), and Van Den Moortel et al. (1996) have all successfully done gas/solids measurements. Hardalupas (1988) and Jackson and Samuelsen (1988) have identified limitations and proposed some improvements of the technique.

In this work, two different techniques are used to estimate the particle size. Measurements of glass particles are performed using PDA, since these solids are smooth and spherical. A slightly modified Shape Discrimination Technique is used to estimate the particle size of FCC catalysts. Although this technique have limitations and disadvantages, it is probably the best suitable technique to estimate the diameter of non-spherical particles in the size range between 5 and 100 μm. Compared with Yang (1991) and Zhang (1992) some important improvements are performed.

1.2.2 Modelling of Gas/Solids Flow Systems

Two different approaches are used in modelling of gas/solids systems, Lagrangian and Euler approaches. The Eulerian approach is most commonly used and are also used here. Eulerian modelling considers the solid phases as well as the gas as continuum. The presence of each phase is described by a volume fraction. In the other approach, the Lagrangian, the particle control volume is considered to move with the fluid. The dynamics of each particle and its interaction with the fluid is modelled, Tsuji (1993). The Lagrangian approach limits the number of particles and are unsuitable in gas/solids flow systems like fluidized bed.

Hydrodynamic models have been developed and applied to describe gas/solids systems since the early sixties. Davidson (1961) and Davidson and Harrison (1963) are usually credited the first model. The hydrodynamic model was used to explore the details of bubble motion, and was based on three postulates:

1) No solids in the gas bubble, the bubble is cylindrical/spherical in 2 and 3 dimensional bed respectively.
2) Rising of bubbles causes particles to move aside, like an inviscid incompressible fluid.
3) The relative velocity between gas and solid satisfies Darcy's law for flow in porous media.

This model has been refined and extended by several scientists. The best known works are Jackson (1963), Murray (1965), Pigford and Baron (1965), Soo (1967), Ruckenstein and Tzeculescu (1967) and Jackson (1970). They all used linearized equations of motions, no attempt was made to solve the set of partial differential equations constituting the model.

In the late seventies, the availability of "high speed" computers made it possible to numerically solve the basic Navier-Stokes equations. Gidaspow (1986) reviewed different computer codes that were based on modelling of the basic conservation equations for mass, momentum and energy for gas/solids flow, but all were still inviscid.

The first to report simulations of viscous gas/solids systems were Tsuo and Gidaspow (1990). They incorporated reasonable viscosities and simulated two-phase flow in a riser. They were able to describe two different flow regimes, core and annulus flow. The importance of the viscous terms were obvious and thus led the way into turbulence modelling of gas/solids systems.

However, already in early eighties Elghobashi and Abou-Arab (1983) and Chen (1984) used the well known k-ε model in the carrier phase to predict the effect of the dispersed phase. The two-equation model describes the conservation of turbulence kinetic energy and dissipation rate for the gas phase. In these models particle-particle interactions are neglected and make them unsuitable for modelling of gas/solids systems like fluidized beds.

The second approach, and best acknowledged of turbulence modelling used in gas/solids flow is known as "kinetic theory for granular flow". The theory of the model is based on kinetic theory of non-uniform gases, as presented in the classical work of Chapman and Cowling (1970).

Actually Bagnold (1954) started this work as early as in the fifties. He derived a particle pressure in uniform shear flow from a simple expression for the collisional frequency of the solids. He also proposed a radial distribution function which is still frequently used.

The first to introduce "granular temperature", defined as proportional to the square of the fluctuating velocity were Jenkins and Savage (1983). Based on the kinetic theory for non-uniform gases, they solved a conservation equation for the granular temperature. To allow for inelastic collision between two particles they introduced a restitution coefficient. Lun et al. (1984) continued this work. Lun and Savage (1987) derived equations for granular flow, assuming mono-sized, rough, inelastic and spherical particles.

Ahmadi and Shahinpour (1983a, 1983b) and Ma and Ahmadi (1990a, 1990b) used a different approach. Those scientists applied the Bhatnager, Gross and Krook (BGK) relaxation model and Chapman Enskog iteration to solve the granular temperature. A simple model was used to account for particle fluid interactions. The dissipation rate for the gas as well as the solid phase was given by algebraic equations. They found reasonable agreement with experimental data.

Based on Jenkins and Savage (1983), Ding and Gidaspow (1990) extended the granular flow model for gas/solids starting with the Boltzmann equation for the velocity distribution of the particles. The Maxwellian velocity distribution function was used as a single particle distribution. The collisional transport consists of binary collision of equal mass and size, smooth and inelastic. Thus model was valid for only dense gas/solids flow.

Gidaspow (1994) extended the work, and included the effect of non-Maxwellian velocity distribution. This made the model valid for both dilute and dense gas/solids flow systems. This model is considered as the "state of the art" in turbulence modelling of gas/solids flow.

With slight modifications, researchers at different institutions around the world have adopted the work of Gidaspow and his co-workers at Illinois Institute of Technology (IIT), and are developing numerical models for gas/solids flow. Some of these institutions are Telemark Institute of Technology (HiT), Samuelsberg (1994), Samuelsberg and Hjertager (1996a, 1996b) and Manger (1996), Morgantown Energy Technology Center (METC), Syamlal et al. (1993), Twente University of Technology, Kuipers et al. (1993), Argonne National Laboratory, Lyczkowski and Bouillard (1989) and Babcock and Wilcox Inc., Alliance Research Center, Burge (1991).

Farrell (1986) and Jenkins and Mancini (1987) extended the kinetic theory for granular flow to binary mixtures. They used the approach of Chapman and Cowling (1970) to derive a model for binary mixtures of smooth, nearly elastic, spherical disks in dense flow. The basic assumption was equal turbulent kinetic energy with a small correction for the individual phase temperatures. A simple shear flow was used to test the theory.

Gidaspow et al. (1996) and Manger (1996) extended the kinetic theory to binary mixtures of solids with unequal granular temperatures between the phases. Both transport equations and constitutive relations for the solids phases were established. The model is valid for dilute as well as dense flow, but have the limitation that the relative velocities between the solids phases should not be too large. Manger (1996) did a simple test simulation in a two-dimensional channel, but no verification of the model is performed.

This thesis continue the work started by Hjertager and Samuelsberg (1992) and Samuelsberg (1994). The turbulence model is based on the kinetic theory for granular flow proposed by Gidaspow (1994) and the binary model by Manger (1996). However, slight modifications are proposed here.

1.3 Outline of Thesis

In this chapter a short introduction to the subject circulating fluidized bed reactors as well as the motivation of this work have been given. A short overview of previous work, with emphasis on LDA/PDA measurement techniques and turbulence modelling of gas/solids systems, are presented.

Chapter 2 gives a presentation of LDA and PDA. The measurement techniques, which are made use of in this study to estimate the mean and fluctuating velocity, diameter and volume fraction are presented.

Chapter 3 shows an overview and description of the governing partial differential equations with constitutive relations. A discussion of the consistency of the multiphase gas/solids flow model is done.

Numerical schemes, algorithms and solution procedure are briefly presented in chapter 4. A short description of the software is given as well.

In chapter 5 a circulating fluidized bed is experimentally investigated using LDA and PDA. Glass particles with a relative large size and density are used. The circulating fluidized bed loop is modelled in a two-dimensional Cartesian coordinate system and three phases (one gas and two particle sizes). Comparisons and discussions of the experimental and computational results are given.

A comparison between simulations of a circulating fluidized bed and data from literature is presented in chapter 6. The simulations are performed using two-dimensional Cartesian grid and three solids phases. The suspended particles are also in these simulations glass particles, group B solids.

Another experimental study of a circulating fluidized bed using LDA is conducted in chapter 7. The solids are FCC catalysts, typical group A particles. A two-dimensional simulation of the riser is performed. Experimental and numerical results are discussed, analyzed and compared.

A three-dimensional simulation of the riser section of a circulating fluidized bed is done in chapter 8. Thus to capture three-dimensional effects in order to obtain more detailed information about the processes involved. The results are analyzed qualitatively.

In chapter 9 conclusions are drawn and recommendations for further work are given.

CHAPTER 2

LASER AND PHASE DOPPLER ANEMOMETRY

Laser Doppler Anemometry (LDA) has become one of the most commonly used experimental tools in single and multiphase flows. The advantages of LDA measurements listed below, shows the capabilities of the technique:

- Non-invasive measurements, no probes introduced into the flow and hence retains all the flow field characteristics.
- No calibration required, measures the flow velocity directly, and is not strongly dependent on the temperature, density and composition of the fluid.
- Measures the desired component of velocity directly, without having to measure the other components.
- High frequency response.
- High dynamic range, can measure flow velocity ranging from μm/s to hypersonic speeds, both positive and negative.
- Small measuring volume.

These features make the LDA technique an ideal instrument for velocity measurements. This technique can also be used to measure size and concentration. There exist at least three different LDA techniques which may estimate the particle size of the dispersed phase. The Phase Discrimination Technique, which is used here, is probably the best suitable LDA/PDA-technique to estimate the diameter of non-spherical particles within the diameter range from 5 to 100 μm. This technique is developed by Arastoopour and Yang (1992), but some important improvement are proposed here.

Phase Doppler Anemometry (PDA) is another technique to measure size of the dispersed phase in multiphase flow. PDA has also desirable features; very wide size range, from micron to millimeters, and good immunity to noise. However, a limitation of the technique is that the particles have to be smooth and spherical.

There are two commonly used techniques to measure the concentration of the dispersed phase, Time Ratio Technique and Data Rate Technique. A description of the Time Ratio Technique which is best suitable for particle sizes smaller than the measuring volume will be given later.

Figure 2.1 shows a schematic sketch of a typical LDA measurement system. The most important parts in such a system are:

- The laser, which provides collimated coherent light source. Normally a low power Helium-Neon or a high power Argon-Ion laser.
- The beam splitter, which splits the beam into two equal intensity beams with the same frequency.
- The bragg cell, which may give one of the beams a frequency shift, so reversal flow can be measured.
- The transmitting optics consist of a focusing lens. Depending on the lens, the two beams will intersect each other at a certain distance from the lens and make a measuring volume. The size of the measuring volume is a function of the wavelength

of the laser beams, focal distance, the angle between the two intersecting beams and the diameter of the laser beams.

- The receiving optics consist of a lens and photo detector(s). The receiving optics may be placed in forward or back scatter modus. The photo detector converts the light energy into electrical energy.
- The data analyzing part consists normally of a signal processor, oscilloscope and a PC for data acquisition and data processing.

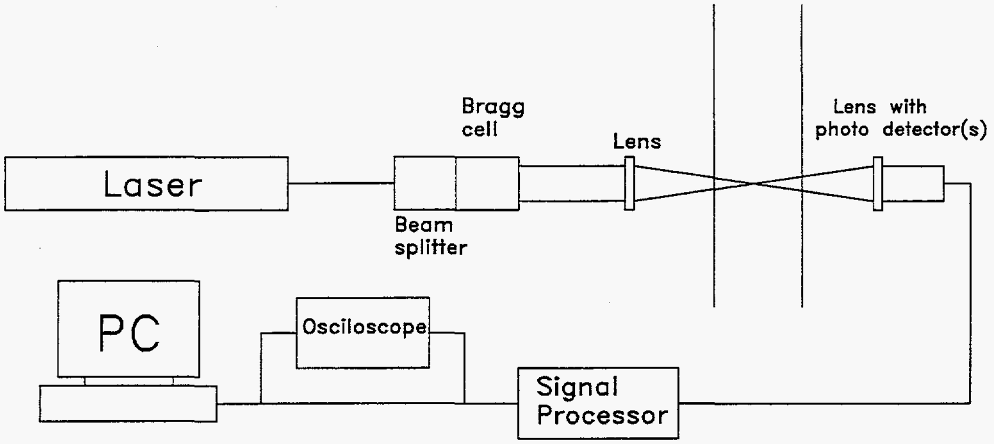

Figure 2.1: A typical LDA measurements system.

2.1 Particle Velocity Measurement

When two coherent Gaussian laser beams are intersecting, the intersection will cause a pattern of plane interference fringes. The intersection area is the measuring volume.

Figure 2.2 gives an overview of a measuring volume with fringes. The fringe spacing δ_f can be shown to be proportional to the wavelength λ and inversely proportional to half of the angle ϑ between the two incident beams:

$$\delta_f = \frac{\lambda}{2\sin(\vartheta/2)} \tag{2.1}$$

When a particle is passing through the measuring volume, it will scatter light and the intensity will change according to the interference fringes, Arastoopour and Shao (1996). The intensity variation of the scattered light or the frequency can be obtained by a photo detector. The velocity of the passing particle will be proportional to the Doppler frequency f_D and the fringe spacing:

$$v_i = f_D \delta_f = \frac{f_D \lambda}{2\sin(\vartheta/2)} \tag{2.2}$$

where v_i is the absolute velocity of the particle in the direction which is perpendicular to the bisector of the two incident laser beams. To detect the direction of the flow, a frequency shift for one of the beams is introduced as indicated in *figure 2.2*. The Doppler frequency is the frequency obtained by the photo detector minus the frequency shift.

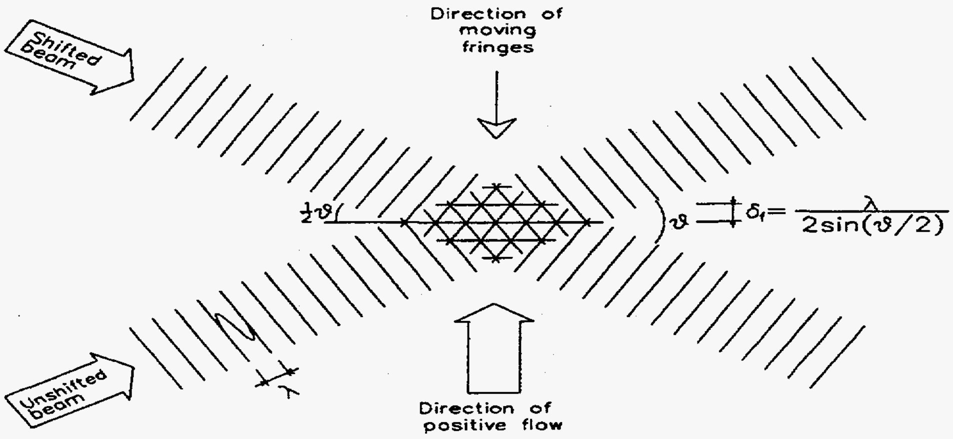

Figure 2.2: An overview of a measuring volume, Dantec (1990).

The mean velocity, V may be obtained by:

$$V = \frac{1}{N_i}\sum_{i=1}^{N_i} v_i \tag{2.3}$$

where N_i is the number of sampled particles. The fluctuating velocity or the Root Mean Square (RMS) velocity, V_{RMS} may be expressed as:

$$V_{RMS} = \sqrt{\frac{1}{(N_i - 1)}\sum_{i=1}^{N_i} (v_i - V)^2} \tag{2.4}$$

2.2 Particle Size Measurement

2.2.1 Shape Discrimination Technique

The Shape Discrimination Technique is based on knowledge about Doppler burst signals. The shape of a Doppler burst signal is determined by the size, shape and surface properties of the particles, concentration of solids, the fluid, the path the particle takes as it passes through the focusing volume and the optical system alignment. This study has documented that the amplitude is a function of the particle velocity as well. Hence, in a system with fixed optical parameters, one type of solids in one type of fluid and one flow condition, the maximum amplitude of a Doppler burst A_D, or the envelop, will depend on the size of the particle D_i the particle velocity v_i, and the path l the particle is traveling through the measuring volume:

$$A_D = A_D(D_i, v_i, l) \tag{2.5}$$

Figure 2.3 shows the Doppler signals generated at different paths. For the same particle with the same velocity, the strongest signal will be generated when the particle is passing through the center of the measuring volume.

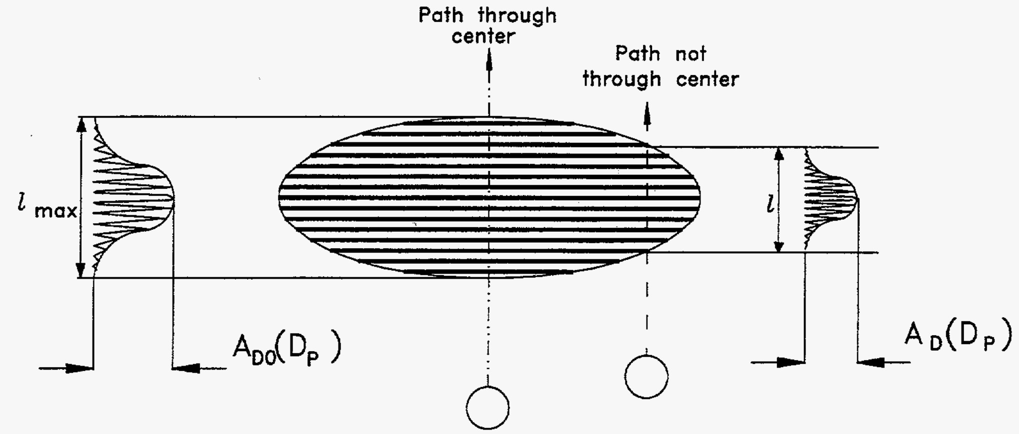

Figure 2.3: Doppler signal generated at different paths, Yang (1991).

The intensity I of a Doppler burst may be written as Farmer (1972):

$$I = I_0\left[\cosh(2yz\vartheta/b_0^2) + \cos(y/\delta_f)\right]\cdot\exp\left[(-2/b_0^2)(x^2+y^2+(z\frac{\vartheta}{2})^2)\right] \tag{2.6}$$

where b_0 is the dimension of the measuring volume in the direction perpendicular to the optical axis.

If the velocity component perpendicular to the laser beam plane and the component parallel to the fringes are neglected, the amplitude of the Doppler burst may be written as:

$$A_D(D_i,v_i,l) = A_{D0}(D_i,v_i)\exp\left[-2(1-\frac{l^2}{l_{\max}^2})\right] \tag{2.7}$$

where A_{D0} is the amplitude of a Doppler burst generated by a particle which is passing through the center of the measuring volume and l_{max} is the maximum possible path length. Since effective path length and maximum possible path length are proportional to the actual peak numbers within one Doppler burst N_{peak} and the maximum peak numbers within one Doppler burst $N_{peak,max}$ the above expression may be written as, Yang (1991):

$$A_{D0}(D_i,v_i) = A_D(D_i,v_i,l)\exp\left[2(1-\frac{N_{peak}^2}{N_{peak,\max}^2})\right] \tag{2.8}$$

To decide if the velocity of a particle is influencing the size of the amplitude or not, a verification experiment is conducted using only one particle (with constant diameter, shape and surface properties), air as the fluid, one optical alignment and the same particle path. The experimental apparatus consist of a motor and a rotating disk, as shown in *figure 2.4.* A tiny wire with known diameter is fixed on the rotating disk, mounted on a shaft of a small variable speed motor. The wire rotates with the disk and is passing through the measuring volume at a specified speed v_i. The trajectory of the particle is perpendicular to the plane forming the bisection of the two laser beams. This trajectory is manually adjusted to ensure that the rotating wire is passing through the center of the measuring volume.

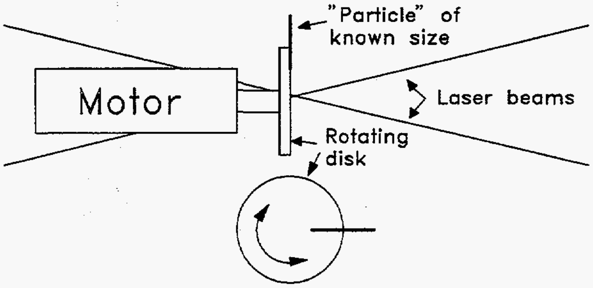

Figure 2.4: Sketch of experimental verification setup.

The verification experiments are conducted at seven different particle velocities between -0.2 and 1.0 m/s. At each velocity the amplitude of the Doppler burst is measured 100 times. *Figure 2.5* shows the mean amplitude size of the Doppler burst for two different diameters of the wire, 500 and 700 *µm* respectively.

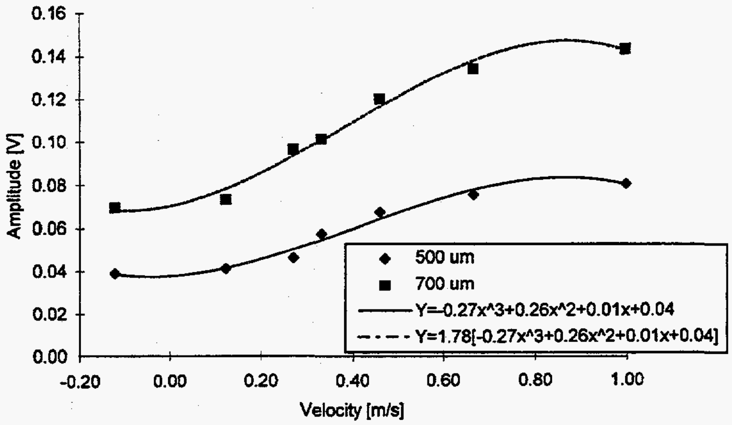

Figure 2.5: Amplitude as a function of particle velocity.

As explained above, the experimental apparatus is aligned in such a way that the amplitude is only a function of the diameter of the wire (particle) and the velocity:

$$A_{D0} = A_{D0}(D_i, v_i) \tag{2.9}$$

As indicated in *figure 2.5* the amplitude of the Doppler burst for a diameter of 500 *µm* may be expressed as:

$$A_{D0}(v_i) = -0.27v_i^3 + 0.26v_i^2 + 0.01v_i + 0.04 \tag{2.10}$$

and with a diameter of 700 *µm* as:

$$A_{D0}(v_i) = 1.78\left[-0.27v_i^3 + 0.26v_i^2 + 0.01v_i + 0.04\right] \tag{2.11}$$

A generalized empirical relation between the amplitude of the Doppler burst and the velocity of the particles may then be expressed as:

$$A_{D0}(D_i,v_i) \propto A_{D0}(D_i)\left[-\ 0.27v_i^3\ +\ 0.26v_i^2\ +\ 0.01v_i\ +\ 0.04\right] \qquad \textit{(2.12)}$$

$$when \quad -\ 0.2\ m/s\ <\ v_i\ <\ 1.0\ m/s$$

By combining *eq. 2.8* and *eq. 2.12* an expression for the amplitude as a function of the diameter may be obtained:

$$A_{D0}(D_i) \propto A_D(D_i,v_i,l)\frac{\exp\left[2\left(1-\frac{N_{peak}^2}{N_{peak,max}^2}\right)\right]}{\left[-0.27v_i^3+0.26v_i^2+0.01v_i+0.04\right]} \qquad \textit{(2.13)}$$

The maximum amplitude of the Doppler burst calculated by *eq. 2.13* will be proportional to the size of the particle which causes the burst. It is rather impossible to obtain a calibration curve theoretically for the amplitude of the Doppler burst versus particle diameter. Hence to transform the amplitude to the diameter of the particles, an experimentally verified calibration procedure has to be done.

The experimental calibration curve can be obtained using the following procedure:

1.) Measure the particle size distribution by using a well recognized particle size instrument and generate a particle diameter versus accumulative percentage plot as in *figure 2.6*.
2.) Mount the experimental equipments and align the LDA optical system.
3.) Specify the flow condition, calibration must be done for each flow condition.
4.) Record a large number of amplitudes at different radial locations.
5.) Calculate the maximum amplitudes (envelop) of the individual Doppler bursts by *eq. 2.13*.
6.) Correct the number of amplitudes for area and time, using the following equation:

$$N_{Doppler}(A_D) = \frac{\int_0^R \left[\frac{N_{Doppler}(A_D,r)}{T_{sample}(r)}\right] r\,dr}{\int_{A_{D,\min}}^{A_{D,\max}} \int_0^R \left[\frac{N_{Doppler}(A_D,r)}{T_{sample}(r)}\right] r\,dr\,dA_D} \qquad \textit{(2.14)}$$

where $N_{Doppler}(A_D)$ is the corrected overall number of amplitudes with the size A_D and $N_{Doppler}(A_D,r)$ is the local signal amplitude distribution at radial location r, which is obtained within the sampling time period $T_{sample}(r)$. *Figure 2.7* shows an accumulative amplitude size distribution.

7.) Finally, make the calibration curve by comparing the particle size and amplitude size distribution. *Figure 2.8* shows an example of such a calibration curve. The calibration curve is used to estimate the particle diameter.

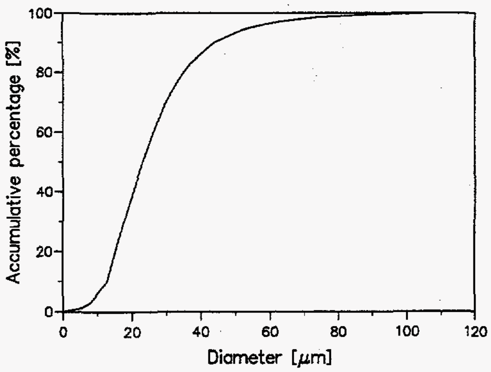

Figure 2.6: Accumulative percentage of particle diameter.

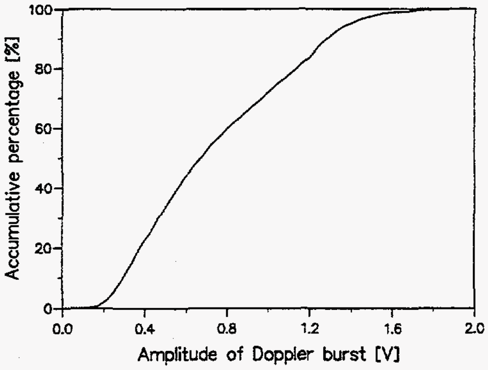

Figure 2.7: Accumulative percentage of amplitude size.

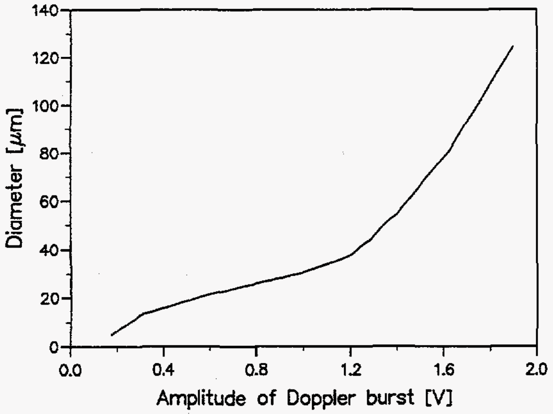

Figure 2.8: A typical calibration curve.

When a given number of particles have been estimated, the mean particle diameter may be calculated. The number mean diameter is given by:

$$D_{Number} = \frac{1}{N_i}\sum_{i=1}^{N_i} D_i \tag{2.15}$$

and the Sauter mean diameter is given by:

$$D_{Sauter} = \frac{\sum_{i=1}^{N_i} D_i^3}{\sum_{i=1}^{N_i} D_i^2} \tag{2.16}$$

Using this technique it is important to discriminate the noise, since the amplitude is very sensitive. To make use of a signal processor the high and low frequency noise may be discriminated. The possible noise in the receiving Doppler signal due to electronic devices is discriminated using time and periodic criteria.

A reasonable Doppler burst should be longer than a minimum time duration $\tau_{\min}$:

$$\tau_{\min} \leq \tau_i \tag{2.17}$$

where τ_i is the time duration for the Doppler burst signal.

A perfect Doppler signal should be oscillating with the same period, a constant frequency. The standard deviation of the oscillating period in the Doppler burst should be less than a critical level:

$$\frac{\sqrt{\frac{1}{(N_{peak}-1)}\sum_{k=1}^{N_{peak}}(\Delta\tau_k-\overline{\Delta\tau})^2}}{\overline{\Delta\tau}} \leq critical\ level \tag{2.18}$$

where $\Delta\tau_k$ is the k-th period and $\overline{\Delta\tau}$ is the average period in the Doppler burst. In this experimental work, the critical level is set equal to 0.5

2.2.2 Phase Doppler Anemometry

Durst and Zare (1975) found that there exists a linear relation between the diameter of a spherical particle and the Doppler signals detected at two different points in space. Almost ten years later Saffmann et al. (1984) extended the technique and presented experimental results on bubble size measurements. Many scientists have later adopted the technique which is often called Phase Difference Technique, since the phase difference between two points is related linearly to the particle diameter. PDA has desirable features including very wide size range, from micron to millimeters, and good immunity to noise. A limitation of the technique is that the particles have to be smooth and spherical.

If two adjacent photo detectors are used to collect scattered laser light, they will show a phase difference which is linearly proportional to the diameter of a smooth and spherical particle as it passing through the measuring volume, Bachalo and Houser (1984). The diameter is a function of the phase shift ϕ, the focal length of the transmitting lens f_l, the fringe spacing δ_f, an optical constant K and spacing of the detectors ΔL:

$$D_i = \frac{f_l\,\delta_f\,\phi}{360°\,\Delta L}K \tag{2.19}$$

Eq. 2.19 shows that for one optical alignment, the diameter of a spherical particle will be proportional to the phase shift between two detectors.

The phase difference between two symmetrically placed detectors will be periodic with the particle diameter. Large particles will therefore produce a phase difference which is not unique. This ambiguity is removed by adding a third photo detector as indicated in *figure 2.9*. The main detector pair is *U1* and *U2*. The detectors *U1* and *U3* have a shorter distance between each other and are used to expand the size range. *Figure 2.9* shows the relative phase difference for each pair of detectors, where:

$$\begin{aligned}\phi_{U1,U2} &= \phi_{U1} - \phi_{U2}\\ \phi_{U1,U3} &= \phi_{U1} - \phi_{U3}\end{aligned} \tag{2.20}$$

The phase difference between the detector pairs give a unique diameter of the particles.

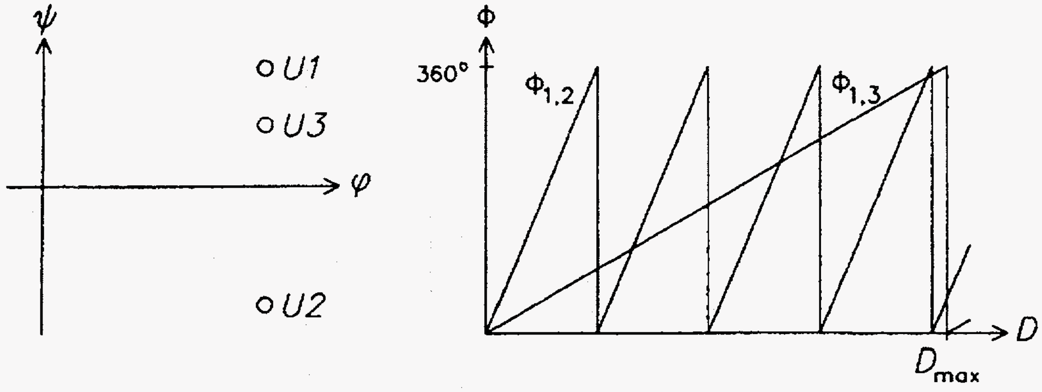

Figure 2.9: Position of detectors and phase difference, Dantec (1990).

The closed loop is used to discriminate the signals. The phase difference between the three detectors may be expressed as:

$$\phi_{Closed\ Loop} = \phi_{U1,U3} + \phi_{U2,U3} + \phi_{U1,U2} \tag{2.21}$$

$\phi_{Closed\ Loop}$ is theoretically zero. If the error is greater than a specified value, the measurement will not be accepted.

2.3 Particle Concentration Measurement

The best suitable technique for small particles, sizes less than the measuring volume, is the Time Ratio Technique, Sekoguchi et al. (1982). The technique uses the time ratio of the dispersed phase to the total sampling time to find the average volume fraction of solids. When a particle is in the measuring volume, the local volume fraction of the dispersed phase may be expressed as:

$$\alpha_i = \frac{\pi D_i^3}{V_{focus}} \tag{2.22}$$

where D_i is the diameter of the i-th particle and V_{focus} is the volume of the measuring volume. Within the sampling time period T_{sample}, the average volume fraction of the solids is:

$$\alpha_s = \frac{\sum_{i=1}^{N_i} \tau_i \alpha_i}{T_{sample}} \tag{2.23}$$

The basic assumption of this technique is that there is only one particle in the measuring volume at the same time, and hence the technique is only suitable for very dilute systems.

CHAPTER 3

GOVERNING EQUATIONS IN MULTIPHASE GAS/SOLIDS MODEL

During the recent years computational fluid dynamics in multiphase flow has become a well accepted and useful tool in modelling of gas/solids flow systems and much progress has been made toward developing computer codes for describing fluidized beds. Most of the developed models are based on a two-phase description, one gas and one solids phase. All the particles are assumed to be identical, characterized by a diameter, form factor, density and a coefficient of restitution. In gas/solids systems, particle segregation due to different size and/or density will play a significant role on the flow behavior. To describe such phenomena an extension to multiple particle phases is essential. A multiphase gas/solids model is given in this chapter and the consistency of the model is discussed briefly.

An Eulerian description of the phases is used, which consider the gas as well as each solids phase as continuum. The presence of each phase is described by a volume fraction, varying from zero to one. The sum of the volume fractions have to be exactly one in each control volume.

The laws of conservation of mass and momentum are satisfied for each phase individually. The dependent variables as the volume fraction and the three velocity components are solved for each phase. All the phases share a fluid pressure. In addition a turbulent kinetic energy equation for each solids phase is solved. No turbulence equation for the gas phase is solved, but an effective gas viscosity is estimated.

To obtain the transport equations for single and multiphase flow, Patankar (1985) and others have used a control volume approach. This gives the equations for the continuous gas phase. For the solids phases, Jenkins and Savage (1983) showed an approach, which started from a statistical point of view with a given distribution of particles and then used the Reynolds transport theorem to develop the well known Boltzmann equation:

$$\frac{\partial f}{\partial t} + c \cdot \frac{\partial f}{\partial r} + F \cdot \frac{\partial f}{\partial c} = (\frac{\partial f}{\partial t})_{coll} \tag{3.1}$$

where c is the instantaneous velocity, r is the position vector, F are the forces per unit mass acting on the particle and $(\partial f/\partial t)_{coll}$ is the rate of change for the distribution function due to the particle collisions. By multiplying the Boltzmann equation with a quantity ψ, and integrating over the velocity space, a transport equation can be obtained, Chapman and Cowling (1970). A complete derivation of the equation for gas/solids flow is done by Gidaspow (1994). Manger (1996) gives an extension to binary mixtures of particulate materials and derives transport equations for each solids phase. So, the constitutive equations come from the interactions of the fluctuating and the mean motion of the particles. The interactions give rise to effective shear viscosities, which relates the random motion to the mean motion of the particles. A turbulent kinetic energy equation or granular temperature is derived for each solids phase in order to predict the random fluctuations for each solids phase. The granular temperature is defined as one-third times the fluctuating velocity squared.

This work, which adopts the multiphase turbulence model proposed by Manger (1996), will not go into detail of the derivation of the transport and constitutive equation. The multiphase model is modified slightly and made consistent.

The CFD model is generalized and written for M phases, one gas phase and N solids phases. Each solids phase is characterized by a diameter, form factor, density and coefficient of restitution.

To enable modelling of porous plates and obstructions, area and volume porosities are included in the governing equations. The porosities may have values between zero and one, where zero is a totally blocked area/volume and unity is open. This makes it more easy to describe complex geometries such as circulating fluidized beds.

3.1 Transport Equations

The CFD model is three-dimensional in Cartesian coordinates and the governing conservation equations are here presented in tensor notation.

3.1.1 Continuity Equations

The gas continuity equation is given by:

$$\frac{\partial}{\partial t}(\beta_v \alpha_g \rho_g) + \frac{\partial}{\partial x_i}(\beta_i \alpha_g \rho_g U_{i,g}) = 0 \tag{3.2}$$

where α, ρ and U_i are volume fraction, density and the i-th direction velocity component, respectively. β_v is volume porosity and β_i is the area porosity in i-direction. No mass transfer is allowed between the phases.

The continuity equation for each solids phase is written as:

$$\frac{\partial}{\partial t}(\beta_v \alpha_s \rho_s) + \frac{\partial}{\partial x_i}(\beta_i \alpha_s \rho_s U_{i,s}) = 0 \tag{3.3}$$

3.1.2 Momentum Equations

The gas phase momentum equation in j-direction may be expressed as:

$$\begin{aligned} &\frac{\partial}{\partial t}(\beta_v \alpha_g \rho_g U_{j,g}) + \frac{\partial}{\partial x_i}(\beta_i \alpha_g \rho_g U_{i,g} U_{j,g}) \\ &= -(\beta_v \alpha_g)\frac{\partial P}{\partial x_j} + \frac{\partial}{\partial x_i}(\beta_i \tau_{ij,g}) + \beta_v \alpha_g \rho_g g_j + \beta_v \sum_{m=1, m\neq g}^{M} \Phi_{gm}(U_{j,m} - U_{j,g}) \end{aligned} \tag{3.4}$$

P and g_j are fluid pressure and j-direction component of gravity respectively. Φ_{gm} is drag coefficient between the phases g and m.

The stress tensor $\tau_{ij,g}$ is given by:

$$\tau_{ij,g} = \mu_{eff,g}\left[\left(\frac{\partial U_j}{\partial x_i} + \frac{\partial U_i}{\partial x_j}\right) - \frac{2}{3}\delta_{ij}\frac{\partial U_k}{\partial x_k}\right]_g \tag{3.5}$$

where δ_{ij} is the Kroenecker delta.

The gas phase turbulence is modelled by the Sub Grid Scale (SGS) model proposed by Deardorff (1971) and thus the effective viscosity $\mu_{eff,g}$ may be estimated as:

$$\mu_{eff,g} = \alpha_g\left(\mu_{lam,g} + \mu_{turb,g}\right) = \alpha_g\mu_{lam,g} + \alpha_g\rho_g(c_t\,\Delta)^2\sqrt{S_{ij,g}:S_{ij,g}}$$

$$\Delta = \sqrt[3]{\Delta x\Delta y\Delta z} \qquad \wedge \qquad S_{ij,g} = \frac{1}{2}\left[\frac{\partial U_j}{\partial x_i} + \frac{\partial U_i}{\partial x_j}\right]_g \tag{3.6}$$

The constant turbulence parameter c_t is estimated to *0.079* by using ReNormalization Group (RNG) theory, Yakhot and Orszag (1986).

The momentum equations for the solids phases in *j*-direction may be written as:

$$\begin{aligned}&\frac{\partial}{\partial t}(\beta_v\alpha_s\rho_s U_{j,s}) + \frac{\partial}{\partial x_i}(\beta_i\alpha_s\rho_s U_{i,s}U_{j,s}) \\ &= -(\beta_v\alpha_s)\frac{\partial P}{\partial x_j} + \frac{\partial}{\partial x_i}(\beta_i\Pi_{ij,s}) + \beta_v\alpha_s\rho_s g_j + \beta_v\sum_{m=1,m\neq s}^{M}\Phi_{sm}(U_{j,m} - U_{j,s})\end{aligned} \tag{3.7}$$

where the total stress tensor $\Pi_{ij,s}$ for each solids phase is:

$$\Pi_{ij,s} = -P_s\delta_{ij} + \xi_s\delta_{ij}\frac{\partial U_{k,s}}{\partial x_k} + \mu_s\left[\left(\frac{\partial U_j}{\partial x_i} + \frac{\partial U_i}{\partial x_j}\right) - \frac{2}{3}\delta_{ij}\frac{\partial U_k}{\partial x_k}\right]_s \tag{3.8}$$

The solids phase pressure P_s consists of a collisional and a kinetic part:

$$P_s = \sum_{n=1}^{N}P_{C,sn} + \alpha_s\rho_s\theta_s \tag{3.9}$$

where $P_{C,sn}$ is the pressure caused by collisions between the solids phases *s* and *n*, and has the expression:

$$P_{C,sn} = \frac{\pi}{3}\left(1 + e_{sn}\right)d_{sn}^3 g_{sn}n_s n_n\left\{\frac{m_0\theta_s\theta_n}{\left(\left(m_s/m_n\right)\theta_s + \left(m_n/m_s\right)\theta_n\right)}\right\}\left\{\frac{\left(m_0/m_s\right)^2\theta_s\theta_n}{\left(\theta_s + \left(m_n/m_s\right)^2\theta_n\right)\left(\theta_s + \theta_n\right)}\right\}^{3/2} \tag{3.10}$$

$$e_{sn} = \frac{1}{2}(e_s + e_n) \qquad \wedge \qquad d_{sn} = \frac{1}{2}(d_s + d_n) \qquad \wedge \qquad m_0 = m_s + m_n$$

e, *d*, *n* and *m* are coefficient of restitution, diameter of the particle, number of particles and mass of a particle respectively. The coefficient of restitution is unity for fully elastic and zero for inelastic collisions. By using the assumption of spherical particles, number of particles and mass of a particle are respectively:

$$n_s = \frac{6\alpha_s}{\pi\,d_s^3} \qquad \wedge \qquad m_s = \frac{\pi\,d_s^3\rho_s}{6} \tag{3.11}$$

g_{sn} is the radial distribution function which is near one when the flow is dilute and becomes infinite when the flow is so dense that motion is impossible. Based on the single solids phase model given implicitly by Bagnold (1954) a new binary radial distribution function is proposed here:

$$g_0 = \left\{ 1 - \left(\frac{1-\alpha_g}{\alpha_{s,\max}} \right)^{\frac{1}{3}} \right\}^{-1} \tag{3.12}$$

$$g_{sn} = \frac{N}{2} \frac{g_0}{(1-\alpha_g)} (\alpha_s + \alpha_n)$$

where $\alpha_{s,\max}$ is maximum total volume fraction of solids.

The solids phases bulk viscosity may be written as:

$$\xi_s = \sum_{n=1}^{N} P_{C,sn} \frac{d_{sn}}{3} \left(\theta_s + (m_n/m_s)\theta_n\right) \sqrt{\frac{2}{\pi \theta_s \theta_n \left(\theta_s + (m_n/m_s)^2 \theta_n\right)}} \tag{3.13}$$

The solids phases shear viscosity consists of a collisional term:

$$\mu_{col,s} = \sum_{n=1}^{N} P_{C,sn} \frac{d_{sn}}{5} \left(\theta_s + (m_n/m_s)\theta_n\right) \sqrt{\frac{2}{\pi \theta_s \theta_n \left(\theta_s + (m_n/m_s)^2 \theta_n\right)}} \tag{3.14}$$

and a kinetic term:

$$\mu_{kin,s} = \frac{2\mu_{dil,s}}{\frac{1}{N}\sum_{n=1}^{N} (1+e_{sn}) g_{sn}} \left\{ 1 + \frac{4}{5} \sum_{n=1}^{N} g_{sn} \alpha_n (1+e_{sn}) \right\}^2 \tag{3.15}$$

where

$$\mu_{dil,s} = \frac{15}{8 d_s^3} \alpha_s l_s \sqrt{\frac{2 m_s \theta_{s,av}}{\pi}} \tag{3.16}$$

$$l_s = \frac{1}{6\sqrt{2}} \frac{d_s}{\alpha_s}$$

To ensure that the dilute viscosity is finite as the volume fraction of solids approaches zero, the mean free path l_s is limited by a characteristic dimension.

The average granular temperature $\theta_{s,av}$ is obtained from:

$$\theta_{s,av} = \frac{2 m_s \theta_s}{\left\{ \sum_{n=1}^{N} \left(\frac{n_n}{n_s}\right) \left(\frac{d_{sn}}{d_s}\right)^2 \sqrt{\frac{(m_0/m_s)^2 \theta_n}{(\theta_s + (m_n/m_s)^2 \theta_n)}} \; S^{3/2} \right\}^2} \tag{3.17}$$

$$S = \frac{(m_0/m_s)^2 \theta_s \theta_n}{\left(\theta_s + (m_n/m_s)^2 \theta_n\right)\left(\theta_s + \theta_n\right)}$$

For $\alpha_g \leq 0.8$, the gas/solids drag coefficients are based on Ergun equation, Ergun (1952):

$$\Phi_{sg} = 150 \frac{\alpha_s (1-\alpha_g) \mu_{lam,g}}{(\psi_s d_s)^2} + 1.75 \frac{\alpha_s \rho_g \, |\vec{u}_g - \vec{u}_s|}{\psi_s d_s} \tag{3.18}$$

where ψ_s is the form factor which is unity for spheres and between zero and one for all other particles.

For $\alpha_g > 0.8$ the drag coefficients are based on the work by Wen and Yu (1966) and Rowe (1961):

$$\Phi_{sg} = \frac{3}{4} C_d \frac{\alpha_s \alpha_g \rho_g \, |\vec{u}_g - \vec{u}_s|}{\psi_s d_s} \alpha_g^{-2.65}$$

$$\begin{aligned} C_d &= \frac{24}{Re_s}(1 + 0.15 Re^{0.687}) && \textit{for} \quad Re_s \leq 1000 \\ C_d &= 0.44 && \textit{for} \quad Re_s > 1000 \end{aligned} \tag{3.19}$$

$$Re_s = \frac{d_s \rho_g \, |\vec{u}_g - \vec{u}_s|}{\mu_{lam,g}}$$

The particle/particle drag coefficients are based on Manger (1996):

$$\begin{aligned} \Phi_{sn} = \beta_v P_{C,sn} \Bigg\{ & \frac{3}{d_{sn}} \sqrt{\frac{2\left(m_s^2 \theta_s + m_n^2 \theta_n\right)}{\pi \, m_0^2 \theta_s \theta_n}} + \frac{1}{|\vec{u}_n - \vec{u}_s|} \\ & \left[\nabla \left| \ln \frac{\alpha_s}{\alpha_n} \right| + \frac{\theta_s \theta_n}{\theta_s + \theta_n} \left| \frac{\nabla \theta_n}{\theta_n^2} - \frac{\nabla \theta_s}{\theta_s^2} \right| + 3 \nabla \left| \frac{\ln(m_n \theta_n)}{\ln(m_s \theta_s)} \right| \right] \Bigg\} \end{aligned} \tag{3.20}$$

3.1.3 Turbulent Kinetic Energy Equations

A turbulent kinetic energy equation or a granular temperature equation is solved for each solids phase:

$$\begin{aligned} & \frac{3}{2} \left[\frac{\partial}{\partial t} (\beta_v \alpha_s \rho_s \theta_s) + \frac{\partial}{\partial x_i} (\beta_i \alpha_s \rho_s U_{i,s} \theta_s) \right] \\ & = \beta_v \left(\Pi_{ij,s} : \frac{\partial U_{j,s}}{\partial x_i} \right) + \frac{\partial}{\partial x_i} \left(\beta_i \kappa_s \frac{\partial \theta_s}{\partial x_i} + \beta_i q_{cor,s} \right) - \beta_v \gamma_s - 3 \beta_v \Phi_{sg} \theta_s \end{aligned} \tag{3.21}$$

The transport coefficient of the turbulent kinetic energy consists of a dilute and a dense part:

$$\kappa_s = \frac{2\kappa_{dil,s}}{\frac{1}{N}\sum_{n=1}^{N}(1+e_{sn})g_{sn}}\left\{1+\frac{6}{5}\sum_{n=1}^{N} g_{sn}\alpha_n(1+e_{sn})\right\}^2 + 2\alpha_s\rho_s d_s\sqrt{\frac{\theta_s}{\pi}}\sum_{n=1}^{N}\alpha_n g_{sn}(1+e_{sn}) \tag{3.22}$$

$$\kappa_{dil,s} = \frac{225}{32}\alpha_s l_s\sqrt{\frac{2m_s\theta_{s,av}}{\pi}}$$

Due to the extension of the kinetic theory for granular flow to multiple particle phases, a correction of the collisional heat flux, $q_{cor,s}$ is obtained:

$$\begin{aligned} q_{cor,s} = \sum_{n=1}^{N} P_{C,sn}(1-e_{sn}) \Bigg\{ & \frac{9}{5}\frac{m_n}{m_0}(\vec{u}_n-\vec{u}_s) \\ & + d_{sn}\Bigg[\sqrt{\frac{2\theta_n}{\pi\left((m_s/m_n)^2\theta_s+\theta_n\right)}}\left(\nabla\ln\frac{\alpha_s}{\alpha_n}+3\nabla\frac{\ln(m_n\theta_n)}{\ln(m_s\theta_s)}\right) \\ & + 3\sqrt{\frac{2m_s^3\theta_s m_n^3\theta_n}{\pi(m_s^2\theta_s+m_n^2\theta_n)}}\left(\frac{m_n\theta_s\theta_n}{\theta_s+\theta_n}\right)\left(\frac{\nabla\theta_s}{\theta_s^2}-\frac{\nabla\theta_n}{\theta_n^2}\right) \\ & + 6m_n\left(\frac{2m_s^3 m_n^3\theta_s\theta_n}{m_s^2\theta_s+m_n^2\theta_n}\right)^{3/2}\left(\frac{\nabla\theta_s}{m_s\theta_s^2}-\frac{\nabla\theta_n}{m_n\theta_n^2}\right)\Bigg]\Bigg\} \end{aligned} \tag{3.23}$$

The dissipation of the turbulent kinetic energy due to particle collisions is given by:

$$\begin{aligned} \gamma_s = & \sum_{n=1}^{N}\frac{3}{4}P_{C,sn}\frac{(1-e_{sn})}{d_{sn}} \\ & \left[4\sqrt{\frac{2\theta_s\theta_n}{\pi\left((m_s/m_o)^2\theta_s+(m_n/m_0)^2\theta_n\right)}} - d_{sn}\left(\frac{(m_s/m_0)\theta_s+(m_n/m_0)\theta_n}{(m_s/m_0)^2\theta_s+(m_n/m_0)^2\theta_n}\right)\frac{\partial U_{k,s}}{\partial x_k}\right] \end{aligned} \tag{3.24}$$

3.2 Consistency of the Multiphase Model

To be consistent a gas/solids flow model with multiple solids phases should fulfil the following condition:

- A solids phase consisting of particles with identical diameter, density and coefficient of restitution can be represented either as a single solids phase of volume fraction α_s or as N distinct solid phases, whose respective volume fractions will sum to α_s.

To show that the presented model is consistent, the simplified model for a single solids phase is given first, following by the multiphase model for two identical solids phases.

3.2.1 Single Solids Phase

For a single solid phase the momentum equation and the constitutive equations presented by *eq. (3.7)* to *(3.20)* will be reduced to the following equations:

$$\begin{aligned}&\frac{\partial}{\partial t}(\beta_v \alpha_s \rho_s U_{j,s}) + \frac{\partial}{\partial x_i}(\beta_i \alpha_s \rho_s U_{i,s} U_{j,s}) \\ &= -(\beta_v \alpha_s)\frac{\partial P}{\partial x_j} + \frac{\partial}{\partial x_i}(\beta_i \Pi_{ij,s}) + \beta_v \alpha_s \rho_s g_j + \Phi_{sg}(U_{j,g} - U_{j,s})\end{aligned} \qquad (3.25)$$

The total stress tensor for the single solid phase model is identically to *eq. (3.8)*, but the solids phase pressure will be simplified to:

$$P_s = \alpha_s \rho_s \left(1 + 2(1+e_s)\alpha_s g_0\right)\theta_s \qquad (3.26)$$

The single solids phase bulk viscosity can be written as:

$$\xi_s = \frac{4}{3}\alpha_s^2 \rho_s d_s g_0 (1+e_s)\sqrt{\frac{\theta_s}{\pi}} \qquad (3.27)$$

The solids phase shear viscosity may be rewritten as:

$$\mu_s = \frac{2\mu_{dil,s}}{(1+e_s)g_0}\left(1 + \frac{4}{5}(1+e_s)g_0\alpha_s\right)^2 + \frac{4}{5}\alpha_s^2 \rho_s d_s g_0 (1+e_s)\sqrt{\frac{\theta_s}{\pi}} \qquad (3.28)$$

where

$$\mu_{dil,s} = \frac{5}{16}\rho_s \alpha_s l_s \sqrt{2\pi\theta_s} \qquad \wedge \qquad l_s = \frac{1}{6\sqrt{2}}\frac{d_s}{\alpha_s} \qquad (3.29)$$

The transport equation for the turbulent kinetic energy of a single solids phase is equivalent to *eq. (3.21)*, but the correction of the collision flux due to multiple particle phases $q_{cor,s}$ is exactly zero. The transport coefficient is reduced to:

$$\kappa_n = \frac{2\kappa_{dil,s}}{(1+e_s)g_0}\left(1 + \frac{6}{5}(1+e_s)g_0\alpha_s\right)^2 + 2\alpha_s^2 \rho_s d_s g_0 (1+e_s)\sqrt{\frac{\theta_s}{\pi}} \qquad (3.30)$$

where

$$\kappa_{dil,s} = \frac{75}{64}\rho_s \alpha_s l_s \sqrt{2\pi\theta_s} \qquad \wedge \qquad l_s = \frac{1}{6\sqrt{2}}\frac{d_s}{\alpha_s} \qquad (3.31)$$

The collisional energy dissipation is simplified to:

$$\gamma_s = 3(1-e_s^2)\alpha_s^2 \rho_s g_0 \theta_s \left(\frac{4}{d_s}\sqrt{\frac{\theta_s}{\pi}} - \frac{\partial U_{k,s}}{\partial x_k}\right) \qquad (3.32)$$

The model presented by *eq. (3.25)* to *(3.32)* is the same as the single solids phase model proposed by Gidaspow (1994) and is normally considered as the "state of the art" for turbulence modelling of gas/solids flow.

3.2.2 Two Identical Solids Phases

Modelling by N solids phases with identical diameters, form factors, densities and coefficients of restitution should give the same mathematical model as described for a single solids phase by *eq. (3.25)* to *(3.32)*. Here, for simplicity the number of identical solids phases N is set to *2*, and:

$$\alpha_s = \alpha_1 + \alpha_2 \tag{3.33}$$

By adding the momentum equations for the solids phases *1* and *2* a common momentum balance may be obtained:

$$\begin{aligned} \frac{\partial}{\partial t}(\beta_v \alpha_s \rho_s U_{j,s}) + \frac{\partial}{\partial x_i}(\beta_i \alpha_s \rho_s U_{i,s} U_{j,s}) &= -(\beta_v \alpha_s)\frac{\partial P}{\partial x_j} \\ + \frac{\partial}{\partial x_i}\left[\beta_i\left((P_1+P_2)\delta_{ij} + (\xi_1+\xi_2)\delta_{ij}\frac{\partial U_{k,s}}{\partial x_k} + (\mu_1+\mu_2)\left(\frac{\partial U_j}{\partial x_i} + \frac{\partial U_i}{\partial x_j} - \frac{2}{3}\delta_{ij}\frac{\partial U_k}{\partial x_k}\right)_s\right)\right] \\ + \beta_v \alpha_s \rho_s g_j + (\Phi_{1g}+\Phi_{2g})(U_{j,g}-U_{j,s}) \end{aligned} \tag{3.34}$$

To satisfy the consistency criterium, the momentum equations *(3.25)* and *(3.34)* have to be identical and hence the following conditions have to be satisfied:

$$\begin{aligned} P_s &= P_1 + P_2 \\ \xi_s &= \xi_1 + \xi_2 \\ \mu_s &= \mu_1 + \mu_2 \\ \Phi_{sg} &= \Phi_{1g} + \Phi_{2g} \end{aligned} \tag{3.35}$$

By comparing a common turbulent kinetic energy equation with the granular temperature of the single solids phase, the following conditions are obtained:

$$\begin{aligned} \kappa_s &= \kappa_1 + \kappa_2 \\ q_{cor,s} &= q_{cor,1} + q_{cor,2} = 0 \\ \gamma_s &= \gamma_1 + \gamma_2 \end{aligned} \tag{3.36}$$

A very detailed derivation of the consistency criterium will not be presented here, but it is briefly shown that the consistency conditions by *eq. (3.35)* and *(3.36)* are fulfilled if the collisional pressures are identical:

$$P_{C,s} = P_{C,1} + P_{C,2} \tag{3.37}$$

The collisional pressure for a single solids phase is given by:

$$P_{C,s} = 2(1+e_s)\alpha_s^2 \rho_s g_0 \theta_s \tag{3.38}$$

For two identical solids phases the sum of the collisional pressures are:

$$P_{C,1} + P_{C,2} = 2(1+e_s)\alpha_1^2 \rho_s g_{11} \theta_s + 2(1+e_s)2\alpha_1 \alpha_2 \rho_s g_{12} \theta_s + 2(1+e_s)2\alpha_2^2 \rho_s g_{22} \theta_s \tag{3.39}$$

Comparing *eq. (3.38)* and *(3.39)* leads to:

$$\alpha_s^2 g_0 = \alpha_1^2 g_{11} + 2\alpha_1 \alpha_2 g_{12} + \alpha_2^2 g_{22} \tag{3.40}$$

This shows that the radial distribution function is the critical part and that the consistency conditions can and can only be fulfilled if:

$$g_0 = g_{11} = g_{12} = g_{22} \tag{3.41}$$

The distribution function proposed here by *eq. (3.12)* is satisfying this criterium, if:

$$\alpha_1 = \alpha_2 = \frac{1}{2}\alpha_s \tag{3.42}$$

Lebowitz (1964), Jenkins and Mancini (1987), Zamankhan (1995) and Boemer (1996) have proposed different models for the binary radial distribution function. However none of these models are satisfying both the consistency criterium, becomes infinity for maximum solids packing and is an expression for a probability of collisional between the two solids phases.

By this it is shown that the presented multiphase gas/solids model is consistent.

CHAPTER 4

NUMERICAL ALGORITHMS AND SOLUTION PROCEDURE

The partial differential equations given in chapter 3 are solved by the finite volume method, Patankar (1980). The calculation domain is divided into a finite number of control volumes in a three-dimensional Cartesian coordinate system. The grid spacing may be uniform or non-uniform. *Figure 4.1* shows a scalar control volume for a two-dimensional Cartesian situation.

In the center of each control volume a main grid point is placed. At these points the scalar variables such as volume fraction, density, pressure, turbulent kinetic energy, transport coefficients and volume porosity are stored. The value of the variables are assumed to be uniform in each control volume.

A staggered grid arrangement is used for the velocity components which are stored at surfaces of the main control volume. Velocity control volumes for a two-dimensional Cartesian situation are shown in *figure 4.2*. The staggered grid arrangement is used to avoid that an alternating unphysical pressure field will be felt like a uniform pressure field by the momentum equations. A numerical method that allows such an unphysical solution is certainly undesirable and not used here. Also the area porosities are stored at the main control volume surfaces.

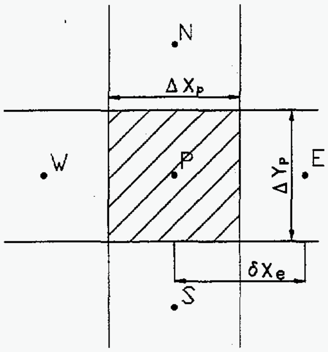

Figure 4.1: Control volume for scalar variables.

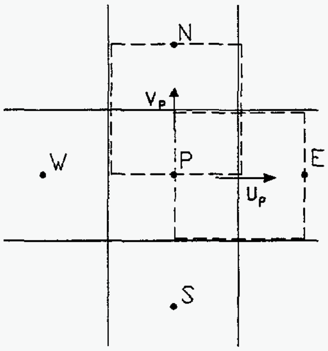

Figure 4.2: Control volumes for velocities.

4.1 Numerical Scheme

From the partial differential equations a general discretization equation for the general dependent variable ϕ is obtained:

$$a_p \phi_p = a_E \phi_E + a_W \phi_W + a_N \phi_N + a_S \phi_S + a_T \phi_T + a_B \phi_B + b \qquad (4.1)$$

The algebraic equation shows that the value of ϕ in point P is a linear function of ϕ in the neighbor points E, W, N, S, T and B. The neighbor coefficients depend on how the ϕ varies between the nodes and include the effects of convection and diffusion. The constant part of a source term is included in b. The coefficient for the point P consists of the sum of the neighbor coefficients, the contribution from last time step and the variable part of the source term.

4.1.1 Convective Term

The conservation equations are integrated in space and time, as indicated in *eq. (4.1)*. The well known upwind difference scheme is used in space, first put forward by Courant et al. (1952). The scheme is most commonly used in multiphase gas/solids flow because of its simplicity and numerical stability, Patankar (1980). The upwind scheme puts the convected property, ϕ_e at the interface equal to the value of ϕ at the grid point on the upwind side of the face. The condition may be written compactly as:

$$F_e \phi_e = \phi_P \max(F_e, 0) - \phi_E \max(-F_e, 0) \qquad (4.2)$$

where

$$F_e \equiv (\rho u)_e \qquad (4.3)$$

4.1.2 Diffusive Term

Since the transport coefficients Γ are stored at the main grid points and the coefficient is required at the control volume surfaces, an average value has to be obtained. It may be shown that an arithmetic mean value may give an unphysical behavior. Hence a harmonic mean which can handle non-uniform transport coefficients is made use of here. For a non-uniform grid spacing the transport coefficient at the east control volume surface will be expressed as:

$$\Gamma_{\phi,e} = \frac{2\Gamma_P \Gamma_E \delta x_e}{\Gamma_P \Delta x_E + \Gamma_E \Delta x_P} \qquad (4.4)$$

4.1.3 Source Term

All source terms are linearized in the standard way:

$$S = S_c + S_p \phi_p \qquad (4.5)$$

The constant source term S_C becomes a contributor to the constant term b in *eq. 4.1*. When dealing with positive definite variables like the turbulent kinetic energy, S_C is required to be positive or zero in order to prevent negative and unphysical values of the variable. Otherwise, as for the momentum equations, the constant source term can becomes both positive and negative. The coefficient of the variable part of the source term S_P has to be negative or zero to ensure convergence and a physically realistic solution.

4.1.4 Transient Scheme

The integration is performed using a fully implicit scheme in time. The implicit scheme postulates that at time t, the variable ϕ_p suddenly drops from the old value ϕ_p^0 to a new value ϕ_p and then stays at the new value over the whole time step. This means that ϕ_p will be linked to the unknown neighbor values ϕ_{nb}, and a solution of the set of simultaneous algebraic equations will be necessary.

The time step is automatically calculated from the Courant number, which is related to stability and accuracy considerations:

$$C = U_{\max}\frac{\Delta t}{\Delta x_{\min}} \leq 1. \tag{4.6}$$

4.2 Initial Conditions

Initial conditions have to be specified for the dependent variables in order to get a unique solution of the governing equations. The velocity field is normally set to zero in the whole calculation domain.

The specification of initial volume fractions depends on the experimental setup. Normally an initial bed of solids with a total volume fraction of the solids set close to the maximum packing of solids is specified. In the rest of the calculation domain a volume fraction of the gas is set to unity.

The pressure field is initialized from the gravity force and such that the pressure at the top plane of the calculation domain is equal to a given value.

To ensure a small initial viscosity for the solids phases, the turbulent kinetic energy is set to:

$$\theta_s = 5\cdot 10^{-6}\,\alpha_s \tag{4.7}$$

4.3 Boundary Conditions

To have physical realistic boundary conditions are essential and their influence on the solution are often underestimated. In this work symmetry boundaries, wall boundaries, inlet and outlet boundaries are used.

4.3.1 Symmetry Boundaries

For a symmetry boundary, plane as well as axi-symmetric, all the perpendicular fluxes are equal zero:

$$\frac{\partial \phi}{\partial x} = 0 \tag{4.8}$$

Here ϕ is the volume fraction, pressure, turbulent kinetic equation and the velocity components parallel to the symmetry plane. The velocity component perpendicular to the plane is set equal zero.

4.3.2 Wall Boundaries

Area and volume porosities are included in the governing equations to make modelling of porous plates and obstructions easy. Due to the included porosities, interior points as well as boundary points may be treated as a wall. The porosities have values between zero and one, where zero is a totally blocked area/volume and unity is open.

For the gas phase, the well accepted no-slip condition is used at the wall.

For the solids phases wall functions are included. The relation for the solids velocity gradients at the wall are based on a microscopic model for particle-wall collisions, Sinclair and Jackson (1989). The rate of transfer of momentum to the wall by particle collisions is given by the product of the average collision frequency of each adjacent particle with the wall, the averaged momentum transferred per collision and the averaged number of particles adjacent to unit area of the surface:

$$\tau_w = \mu_s \frac{\partial U_{j,s}}{\partial x_i} = \frac{\alpha_s}{\alpha_{s,\max}} \frac{\pi}{6} \rho_s \omega_s \sqrt{3\theta_s}\, U_{j,s}\, g_{ss,w} \tag{4.9}$$

where ω is a specularity factor, whose value varies between zero for a completely specular collisions and unity when particles are scattered diffusely.

Sinclair and Jackson (1989) also gave an expression for the turbulent kinetic energy flux at the wall as the turbulence production minus the rate of dissipation per unit area, given by:

$$q_w = \frac{\alpha_s(1-\alpha_g)}{\alpha_{s,\max}} g_{ss,w} \pi \sqrt{3}\, \rho_s \left[\frac{\omega_s}{6} \sqrt{\theta_s}\, U_{j,s}^2 - \frac{1}{4}(1-e_{sw}^2)\theta_s \sqrt{\theta_s} \right] \tag{4.10}$$

For the volume fractions and pressure a zero flux condition is used. The velocity component perpendicular to the wall is obviously set to zero.

4.3.3 Inlet and Outlet Boundaries

The inlet boundaries are given by a specific inflow flux. For the solids phases, the turbulent kinetic energy at the inlet is estimated in the same way as in the initialization, by *eq. (4.6)*.

At the outlet, the volume fraction, pressure, turbulent kinetic energy and velocity of the dispersed phases are extrapolated from upstream. Since the overall continuity has to be satisfied to ensure convergence and a correct solution, the velocity for the continuous phase is calculated from the total mass balance at the outlet.

4.4 Multiphase Solution Algorithm

The continuity equation for each phase is used to solve the volume fraction for that phase. In order to avoid numerical errors and to get a more stable expression for the volume fractions, the continuity equations are combined, multiplied and added together before they are solved, Hjertager (1993).

The discretized equations are solved sequentially. Due to nonlinear equations and the strong coupling between the equations, an iterative solution procedure is desirable. The numerical solution procedure is based on the well known single phase algorithm SIMPLE (Semi-Implicit Method for Pressure-Linked Equations), Patankar and Spalding (1972). As the name indicates, the algorithm takes care of the strong coupling between the continuity and the momentum equations. Spalding (1983) did an extension to multiphase flow and named the algorithm IPSA (InterPhase-Slip Algorithm). The pressure correction equation, which is common for all the phases, is derived from the total continuity equation. To avoid dominant influence of the particle phases with high density, the individual continuity equations are divided by their respective reference density before their are added together.

Due to the strong coupling between the phases through the drag forces, a Partial Elimination Algorithm (PEA) given for two-phase flow by Hjertager, (1993) is used to de-couple the drag. The PEA, which substitute the variable that appear in another variables equation by its own equation, is generalized and extended to *M* phases by Solberg (1994).

4.5 Solving Algebraic Equations

Discretization of the governing differential equations results in a system of algebraic equations which have to be solved This may be done in several ways. The TriDiagonal Matrix Algorithm (TDMA) is adopted here, Patankar (1980). The name refers to the fact that when the matrix of the algebraic equations is written, all the non-zero coefficients are aligned along the three diagonal of the matrix. This means that for one dimension the solution is found directly by forward and backward substitution. The extension to two and three dimensions is simple and straightforward, but changes the solver from a direct to an iterative method.

4.6 Solution Procedure

The mathematical model presented in chapter 3 is implemented in a transient three dimensional computer code using the numerical algorithms described in the previous section. The code is written in FORTRAN. A flow chart of the iterative solution procedure is visualized in *figure 4.3*

4.7 Computer Code Outline

The computer code is named FLOTRACS-MP-3D. The software package consists of a preprocessing part, the actual computer code and a postprocessing part. *Figure 4.4* shows the relationship between these parts.

The preprocessing part is based on a text editor or on AutoCAD (FloCAD-3D). The preprocessing part generates a case file, which is the input to the model and flow simulation. In the case file central start conditions such as a geometrical description, coordinate system and number of control volumes, number of phases, initial and boundary conditions and other flow parameters have to be specified.

The main part of the software is the transient three dimensional computer code, which is using the described mathematical model and solution algorithms.

For the postprocessing part commercial software packages are used. A number of presentations and data analysis software is available.

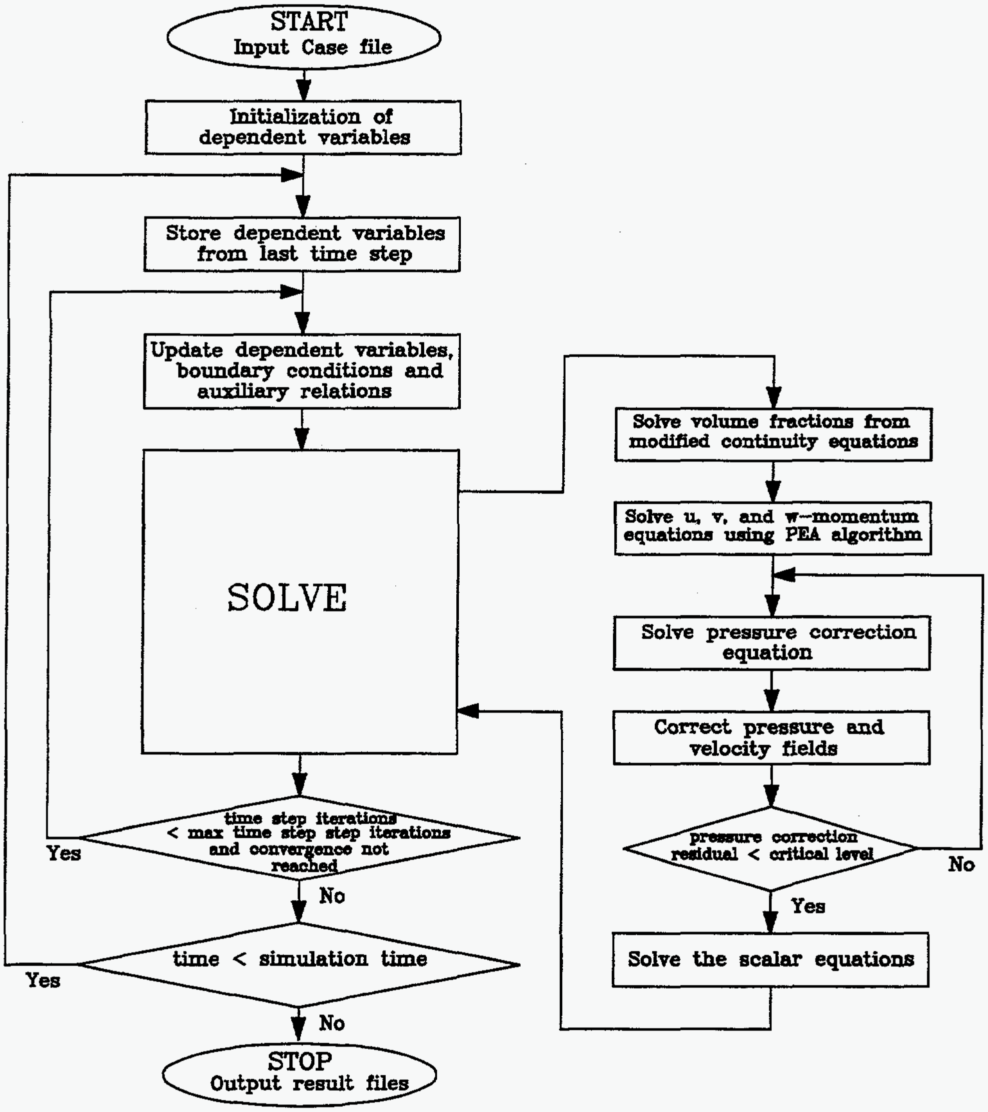

Figure 4.3: Flow chart of iterative solution procedure.

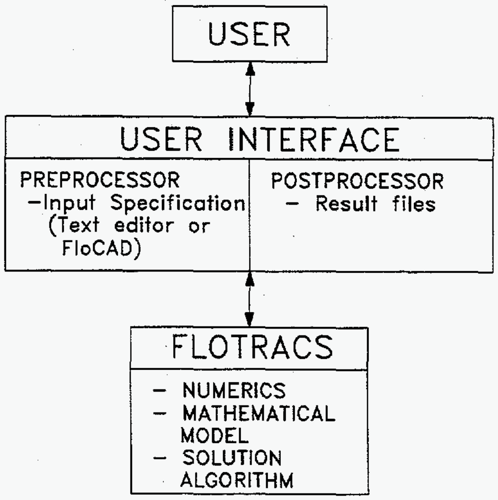

Figure 4.4: The FLOTRACS-MP-3D software.

CHAPTER 5

AN EXPERIMENTAL AND COMPUTATIONAL STUDY OF A 0.032 m I.D. CFB

At Telemark Institute of Technology (HiT-TF) experimental studies of a circulating fluidized bed have been conducted for several years. Samuelsberg and Hjertager (1996a) did successful velocity measurements of FCC catalyst in the cold flow laboratory scale circulating fluidized bed using LDA. Using a slightly modified reactor, and diameter, velocity and volume fraction measurements are performed in the present study. The dispersed phase is spherical glass particles which are classified as group B particles, Geldart (1973). A LDA/PDA system delivered by DANTEC is used in the experimental study. The experiments are conducted with one dilute particle concentration and with three different superficial gas velocities.

The circulating fluidized bed loop is modelled in a two-dimensional Cartesian coordinate system. Two solids phases are used to describe the particulate materials in the simulations.

The experimental and computational results are compared, analyzed and discussed.

5.1 Experimental Setup

5.1.1 Circulating Fluidized Bed

The riser has a internal diameter of 0.032 m, is 1.0 m high and made of clear plexiglass. The primary gas inlet is located at the bottom of the riser. To provide a uniform gas velocity at the inlet, an air distributor is installed. The distributor is a Duran filter-plate with a thickness and porosity of 0.004 m and 0.36 respectively.

At the top of the riser the suspended particles enter a glass cyclone where the solids are separated from the gas and recycled via a return loop. Supply of secondary air, positioned 0.05 m above the air distributor feeds the solids back to the riser. *Figure 5.1* shows a schematic sketch of the circulating fluidized bed system.

The air has ambient temperature and pressure. To minimize the influence of electrostatic effects, a humidifier is installed upstream the main air inlet.

The measurements are conducted with three different superficial gas velocities, 0.8 m/s, 1.0 m/s and 1.2 m/s respectively. To prevent the particles to build up in the recirculation loop, the secondary air inlet velocity is held constant at 0.3 m/s. The secondary air inlet has a diameter of 0.008 m.

From a Gaussian particle size distribution with a Sauter mean diameter of 157 μm two distinct particle groups are sieved out. The sieved particles have diameters between 100 and 130 μm and between 175 and 205 μm for the smallest and largest particles respectively. The mean particle diameter of the two groups are approximately 120 and 185 μm. The two distinct particle groups are mixed together and the initial volume concentration of each group is identical. The initial bed height is 0.04 m. Thus the overall volume concentration of solids in the riser is 2.5 %. The particle density is 2400 kg/m^3.

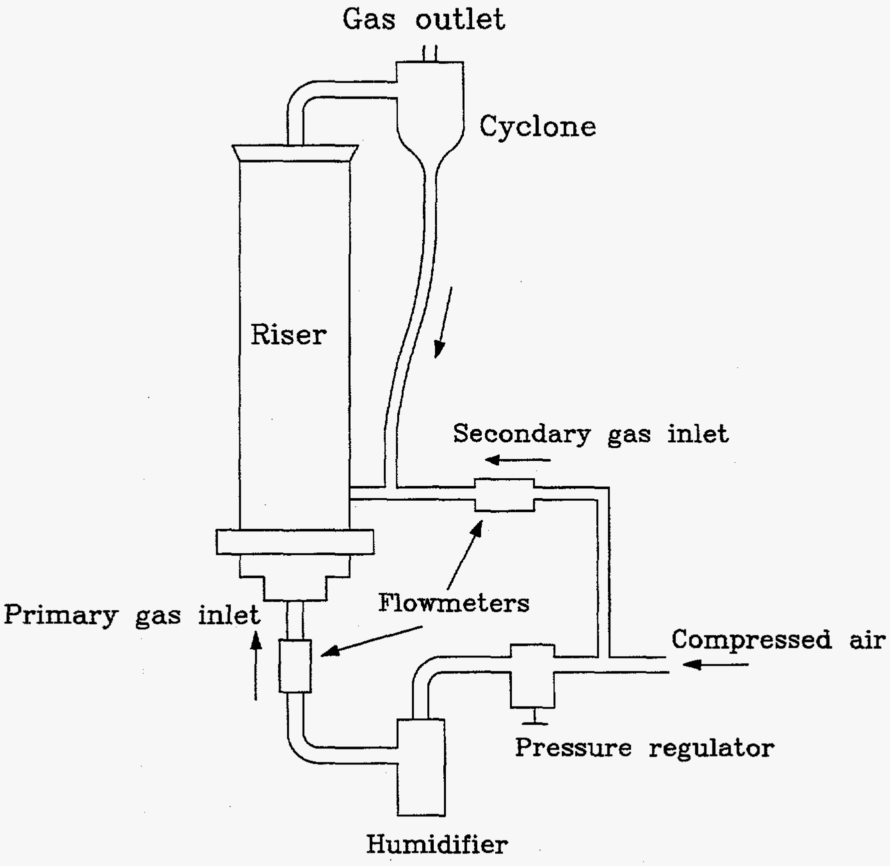

Figure 5.1: A schematic sketch of the laboratory scale CFB.

5.1.2 Laser and Phase Doppler Anemometry

The laser source is a 2 W Spectra-Physics Stabilite 2016 Argon-Ion laser operating at a wavelength of 514.5 nm. The LDA/PDA system is applied in an off-axis back scatter modus. The transmitting and receiving lenses have focal length of 310 and 600 mm respectively. *Table 5.1* gives a summary of the most essential LDA/PDA parameters. An IBM compatible computer is used on-line to data acquisition and processing.

The measurements are performed at three heights, 0.2, 0.4 and 0.7 m above the main gas inlet respectively. At each height the measurements are done at 25 different radial positions, from wall to wall. Mean particle velocity and fluctuating velocity profiles are obtained for each particle group. Volume fraction profiles of solids and mean diameter profiles are measured as well. Mean diameters along the center axis are also measured and presented. The local mean diameters and velocities are the mean values of 3000 accepted samples in each measuring point.

Wavelength	514.5 nm
Fringe spacing	4.2 μm
Beam separation	38 mm
Focal length, transmitting lens	310 mm
Focal length, receiving lens	600 mm
Width of measuring volume	0.15 mm
Length of measuring volume	2.45 mm
Effective scattering angle	124 °
Velocity range	- 1.26 to 3.28 m/s
Particle/gas refraction index	1.51/1.00

Table 5.1: LDA/PDA parameters.

5.2 Numerical Flow Parameters, Initial and Boundary Conditions

The whole circulating fluidized bed loop as shown in *figure 5.1*, is modelled and simulated in a two-dimensional Cartesian coordinate system. The calculation domain is divided into 29×102 control volumes in radial and axial direction respectively. The grid is uniform in the axial direction, but in the radial direction a non-uniform grid is used in order to have smaller control volumes close to the walls, where the volume fraction and velocity gradients increase. The circulating fluidized bed model with internal obstructions and grid nodes is shown in *figure 5.2*.

Two solids phases are used to describe the particles. The two solids phases have identical flow parameters, but different diameters. *Table 5.2* gives a summary of the flow parameters.

The reactor is initially filled with a 0.04 m high bed where the total volume fraction of solids is approximately 0.63. The two solids phases are perfectly mixed in the bed and are assumed to have an identical initial volume fraction.

One-dimensional plug flow is assumed at the primary as well as at the secondary gas inlet. At the outlet, which is located at the top of the cyclone, a continuity condition for the gas phase is used. No particles are allowed to leave the circulating fluidized bed system. At the walls, the no-slip wall condition is used for the gas. Even though a humidifier was installed to prevent electrostatic effects, significant static electricity was observed during the experiments, and particles were sticking to the wall. Due to this a no-slip condition is also used for the solids phases. A zero gradient condition is used for the turbulent kinetic energy.

All the simulations are run for twelve seconds real time. The time averaged results are obtained from the two last seconds of the simulations.

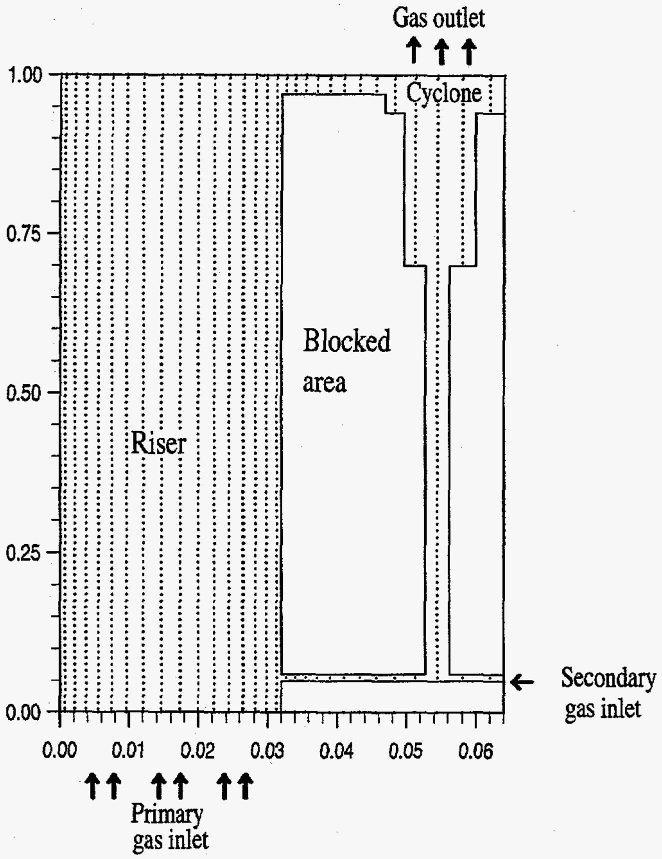

Figure 5.2: Calculation domain with internal obstructions and grid nodes.

	Gas Phase	Solids Phase I	Solids Phase II
Mean Diameter [μm]	-	120	185
Density [kg/m^3]	1.20	2400	2400
Form factor [-]	-	1.00	1.00
Laminar viscosity [kg/ms]	1.8E-5	-	-
Restitution coefficient, solids [-]	-	0.99	0.99
Courant number [-]	1.00		
Maximum total volume fraction of solids [-]	0.63		

Table 5.2: Numerical flow parameters.

5.3 Experimental and Numerical Results

In the experimental as well as in the computational study, most emphasis is given to the flow condition with a superficial gas velocity of 1.0 m/s. Flow conditions with lower and higher superficial gas velocity, 0.8 and 1.2 m/s respectively, are used to investigate the sensitivity and general trends of the flow behavior.

5.3.1 Particle Diameter Profiles

The particle size distribution are important in chemical reactors, and axial as well as radial segregation by size will have large influence on the reaction kinetics and catalyst activity. It is well accepted knowledge that risers can generally be divided into three distinct zones. Above the inlet there will be a section looked upon as a dense turbulent bubbling bed with nearly constant concentration of solids. In this region the averaged particle size will be large. Above the dense zone comes a freeboard zone with a smaller averaged particle size and a significant decreasing of solids concentration. At the top of the riser an exit zone will exist. Depending on the outlet geometry, the concentration of solids will decrease/increase and the particle diameter will normally be small. When the superficial gas velocity increases, the solids concentration distribution as well as the diameter distribution will be more uniform in the axial direction.

Figure 5.3 shows the measured and computed axial number averaged diameter profile along the center axis of the riser. The superficial gas velocity is 1.0 m/s. The averaged diameter is significantly decreasing with the height above the inlet. The measurements show that from 0.2 to 0.7 m above the primary gas inlet, the averaged diameter decreases from 135 to 120 μm. Due to a dense zone it was not possible to conduct measurements lower than 0.2 m above the inlet. However the experimentally obtained mean diameter seems to increase exponentially in the dense zone. The simulation shows exactly the same trend and the maximum deviation between measurements and simulation is just about 2 μm.

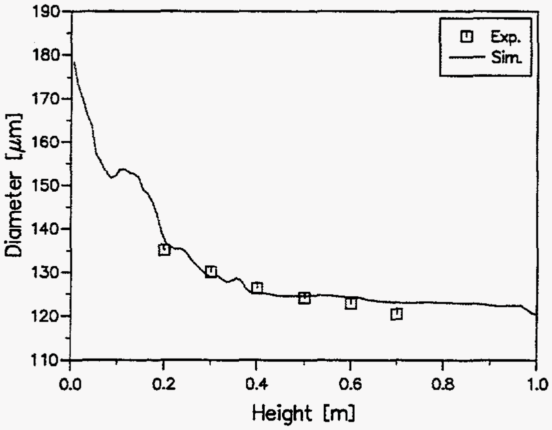

Figure 5.3: Axial particle diameter profile, V_{sup}=1.0 m/s.

The experimental and computational results show the importance of using more than one solids phase in modelling of a gas/solids flow system with a non-uniform particle size distribution. With one solids phase the deviation between the real and actual diameter would have been 30-40 μm in most of the riser. By using two solids phases the maximum deviation is reduced to about 2 μm.

With different superficial gas velocities the form and slope of the axial diameter profile will be changed. This is shown in *figure 5.4*. When the gas velocity decreases the particles are more difficult to fluidize and only the smallest particles will reach the freeboard and circulate in the loop. In the dense section a very large mean diameter is observed. By increasing the gas velocity a more uniform axial diameter distribution appears. The mathematic model predicts the axial segregation very well for all flow conditions and only insignificant deviations from the experimental data are observed.

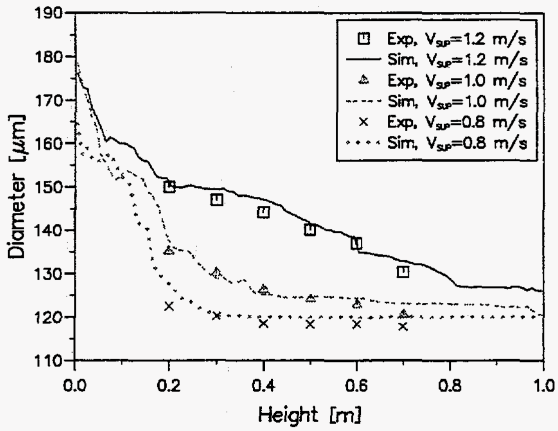

Figure 5.4: Axial particle diameter profiles for different superficial gas velocities.

Core-annulus flow will normally occur in the riser of a circulating fluidized bed and is frequently observed and reported in the literature. Core-annulus flow is characterized by a nearly constant particle upflow and a relative small concentration of solids in the central part of the riser, called the core region. Near the wall, in the annulus, the concentration of solids increases and there will be a downflow of solids. No significant radial variation of the particle mean diameter in the annulus and the core regions seems to be observed and reported in earlier studies of fluidized beds.

Figure 5.5 shows the measured and computed number averaged particle diameter profiles at three different heights above the inlet. The experimental data does not support the behavior reported in the literature of the subject and shows a significant difference in the mean diameter at the center of the riser and near the wall. The difference increases with the height above inlet, which means decreasing concentration of solids. The mathematical model predicts a correct mean diameter in the core region at all heights, but is not able to calculate the significant increases of mean diameter in the wall region.

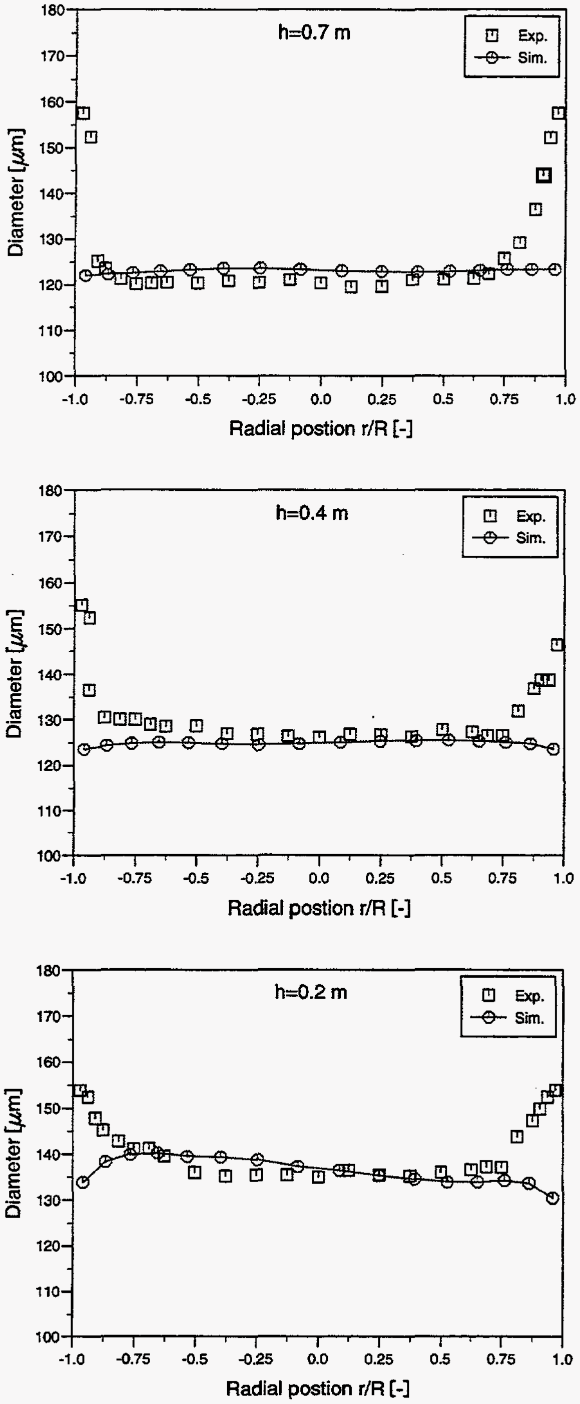

Figure 5.5: Mean particle diameter profiles at different heights, V_{sup}=1.0 m/s.

Figure 5.6 shows a comparison of the mean particle diameter profiles for different superficial gas velocities, 0.4 m above the main gas inlet. With a gas velocity of 0.8 m/s the concentration 0.4 m above the inlet is very dilute and the radial diameter segregation is large. By increasing the gas velocity, the concentration increases and the radial diameter variation decreases. This means less radial segregation or more radial mixing. For all simulations the mean diameter in the central part is in good agreement with the experimental results, although discrepancies are observed in the annulus region.

The axial segregation due to different particle diameters, is explained by the fact that smaller particles are more easy to fluidize and will follow the gas more effectively than larger ones. From the empirical drag coefficient given in *eq. (3.19)* it can be shown that the minimum fluidization velocity is proportional to the mean diameter. The segregation by size will be reduced when the superficial gas velocity and hence gas/solids drag increases. Also the particle-particle drag, which is proportional to the square root of the turbulent kinetic energy, plays a major role at the segregation by size.

The radial segregation of the mean diameter may be explained by the same phenomena. Larger particles will not follow the gas effectively and start accumulating, particularly in the wall region where the gas velocity is very low. Another important factor in a circulating fluidized bed will be that the smallest particle will probably circulate in the whole system, up in the core region and recirculate back through the standpipe. Larger particles will also start flowing up in the core and then loose the momentum and start falling down near the wall. Thus a larger mean diameter is observed in the annulus than in the core region.

In CFD modelling of bubbly two-phase flow, Lahey (1995) and others have shown that a lift force has significant influence on the radial phase distribution. The lift force is proportional to the axial velocity gradient in radial direction of the continuous phase and the relative velocity between the dispersed and continuous phase. It may be reasonable that this force should have an influence also in a gas/solids flow system. To test this, the lift force was included into the mathematical model. However the simulations show that the lift force in a gas/solids flow system has only small effects on the flow pattern.

A Magnus-type force which is produced by spin and rotation of particles may have effects on the radial segregation. This force is more complex to implement in the model and is not included, but the effects should be studied in the future.

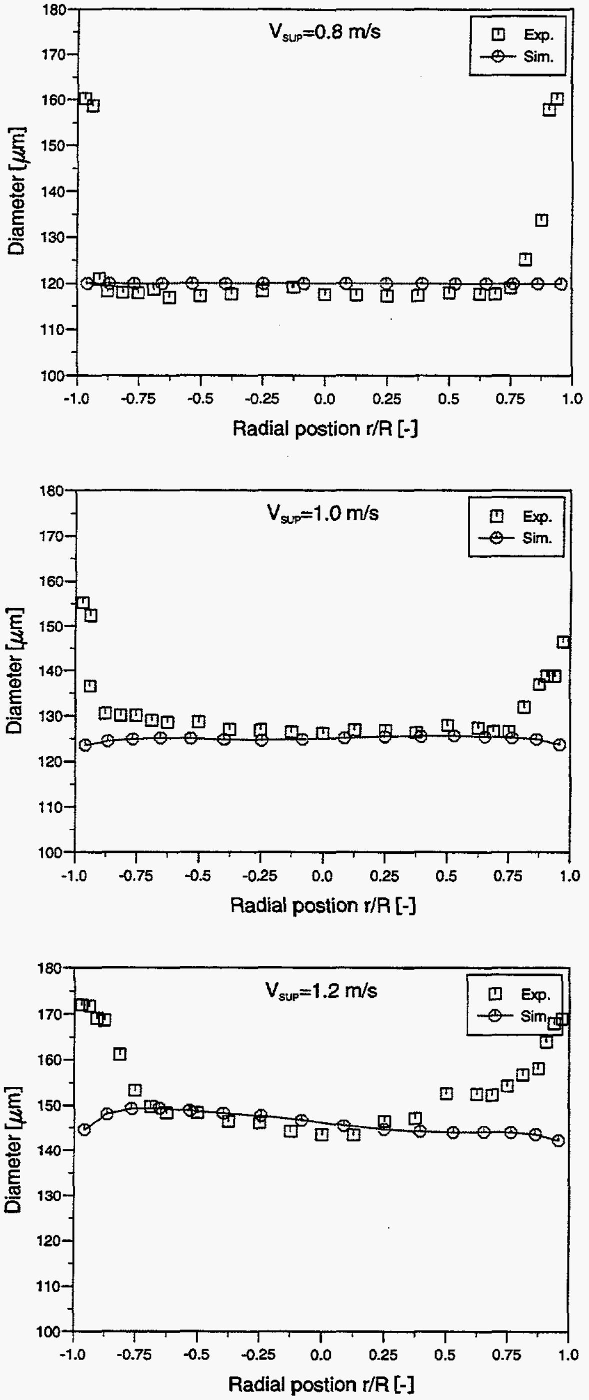

Figure 5.6: Mean particle diameter profiles for different superficial gas velocities, h=0.4 m.

5.3.2 Volume Fraction Profiles

The LDA/PDA system delivered by Dantec is only able to estimate the concentration of solids by the Time Ratio Technique. The technique has the limitations that there should be only one particle in the measuring volume at the same time and that this particle is less than the measuring volume. Since the width of the measuring volume is 150 μm and the system cannot be characterized as very dilute, there may be significant errors in the volume fractions measurements. However the volume fraction measurements should give a good indication of the order of magnitude and general trends.

Figure 5.7 shows the measured and computed radial volume fraction profiles of solids at three different heights for a superficial gas velocity of 1.0 m/s. The general agreement between the experimental and numerical results is fairly good. The simulated and measured profiles have the same form. At all heights the solids concentration distribution are as expected, dilute in the core region and more dense in the wall region in the simulation as well as in the measurements. The solids concentration is most dense at height 0.2 m. The height 0.4 m and 0.7 m seem to be in the freeboard zone, and the solids concentration is more dilute. At these two heights there are larger differences between the concentration of solids in the annulus and in the core regions.

The computed volume fraction profiles of each solids phase are shown in *figure 5.8*. For both phases the concentration of solids increases from the center of the riser and toward the wall. Similar to the mean diameter, the radial concentration gradient seems to increase with height above the inlet. The smallest particles (solids phase I) separate more distinct between the annulus and the core regions than the larger one (solids phase II). The largest particles have not the same increase of the volume fraction in the wall region as the smaller solids.

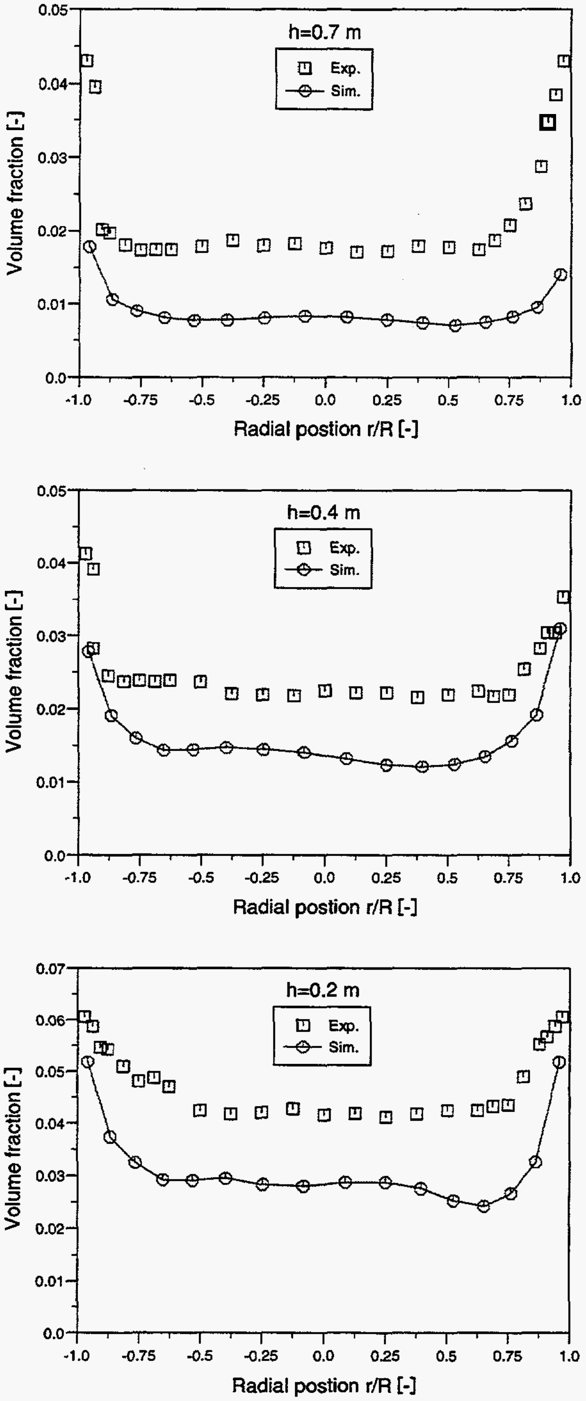

Figure 5.7: Volume fraction profiles of solids at different heights, V_{SUP}=1.0 m/s.

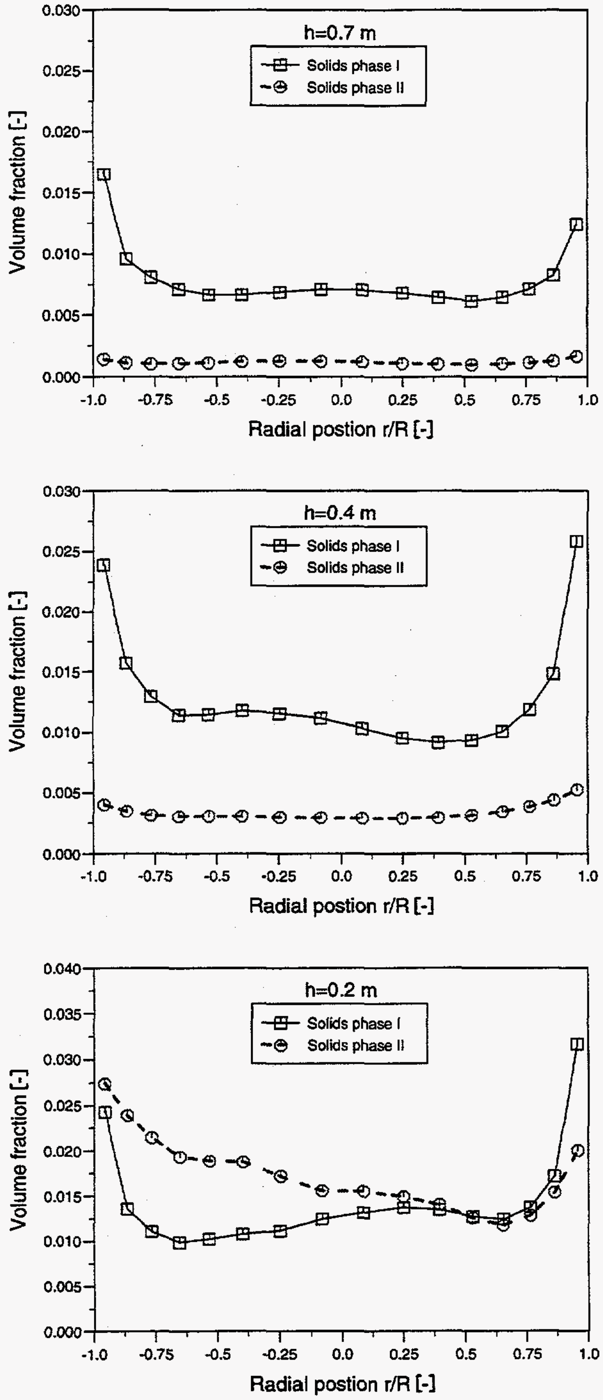

Figure 5.8: Computed volume fraction profiles, V_{SUP}=1.0 m/s.

5.3.3 Particle Velocity Profiles

Measured and computed particle velocity profiles for each particle group are presented in *figure 5.9*. The particle velocity profiles are obtained with a superficial gas velocity of 1.0 m/s, and 0.2, 0.4 and 0.7 m above the main gas inlet.

As illustrated in the figure, the particles move upward in the central part of the riser and downward near the walls, a behavior which is typical for core-annulus flow. The behavior is clearly observed in the experiments as well as in the simulations. At all heights the negative velocities in the wall regions are almost correctly predicted. The computed core velocities are in good agreement with the experimental results, although a too low velocity is obtained at height 0.2 m above the primary gas inlet.

The measured velocity profiles show a relative velocity between particles of different sizes in the core region. In the wall region, no significant velocity deviation is observed in the experiments. The relative velocities are expected and caused by different gas-particle drag for different particle sizes. The particle-particle drag, which is a strong function of the particle collisions will also play a major role at the magnitude of the relative velocity. The particle-particle drag decreases normally in a dilute gas/solids system where the particle-particle collisions are of less importance. The relative velocity decreases slightly with the height above the gas inlet due to a lower mean velocity in the upper part of the riser.

The simulation shows a behavior similar to the measurements even though the relative velocity is a little too high at all heights, probably due to a too small estimated particle-particle drag. The too large computed relative particle velocity may be one of the reasons for the incorrectly obtained mean diameters in the annulus region. A too low particle velocity of the largest particle will give a too low circulation of larger particles in the riser and hence an incorrect radial diameter distribution.

Figure 5.10 and *5.11* show the velocity profiles at height 0.4 m obtained with superficial gas velocity of 0.8 and 1.2 m/s respectively. The same trends are observed, typical core-annulus flow and a relative velocity between the particles of different sizes in the central part of the riser. The relative velocity increases slightly with the superficial gas velocity. The simulations are in a fairly good agreement with the measurements and a typical core-annulus flow behavior with a relative velocity between the solids phases are obtained for all flow conditions.

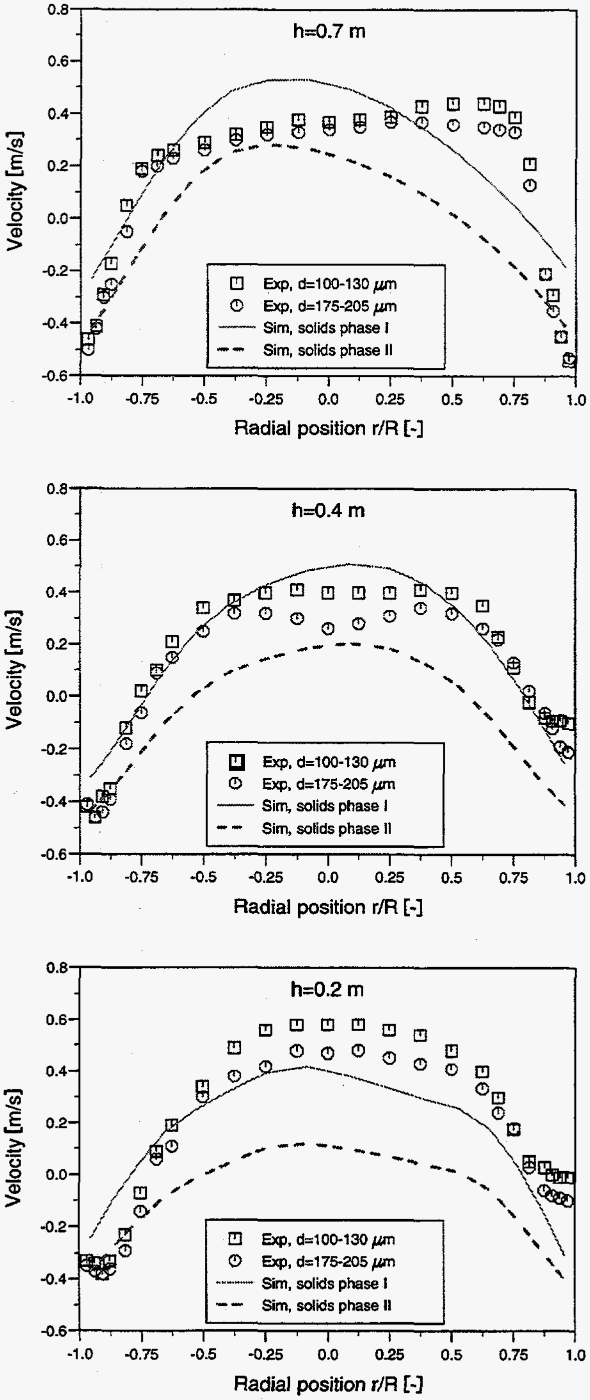

Figure 5.9: Particle velocity profiles at different heights, V_{SUP}=1.0 m/s.

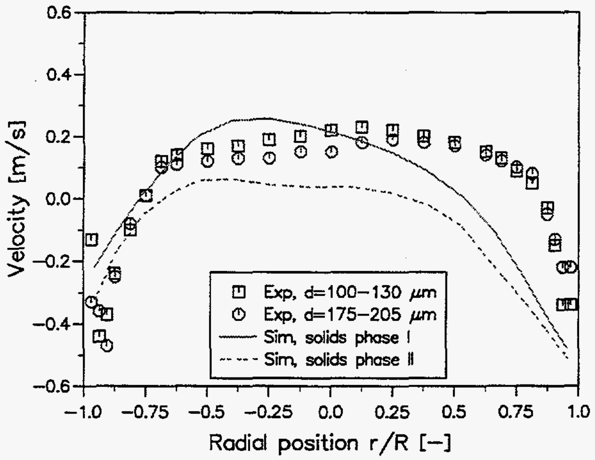

Figure 5.10: Particle velocity profiles, h=0.4 m and V_{SUP}=0.8 m/s.

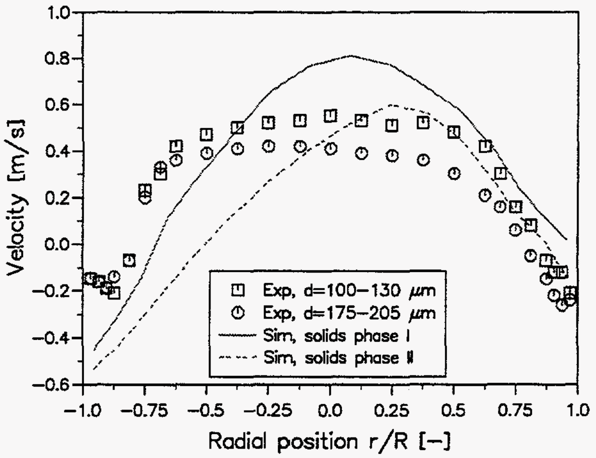

Figure 5.11: Particle velocity profiles, h=0.4 m and V_{SUP}=1.2 m/s.

5.3.4 Fluctuating Particle Velocity

The fluctuating velocity is measured and compared against computational results. The computed particle Root Mean Square (RMS) velocities are derived from the definition of granular temperature:

$$V_{RMS} = \sqrt{3\theta_s} \tag{5.1}$$

The RMS velocities from experiments are found by *eq. (2.4)*. The RMS velocity profiles are measured for each particle group, and calculated for each solids phase.

A comparison of the experimental and numerical results is done in *figure 5.12*. The particle RMS velocity profiles are obtained at heights 0.2, 0.4 and 0.7 m and with a superficial gas velocity of 1.0 m/s. For a very dilute gas/solids flow system that is considered in these experiments, the fluctuating velocity or the turbulence is mainly produced by shear. The RMS velocity in such a system increases from the center of the riser toward the wall. The turbulence decreases slightly with the height of the riser. At height 0.2 m where the concentration of solids is more dense, also particle-particle collisions have significantly influence of the magnitude of the turbulence. Hence the turbulence does not increase as much in the shear layer at this height, as at 0.4 and 0.7 m, where the concentration of solids is more dilute.

The general trends in the simulation are in relative good agreement with the experimental results. However the simulations are a little too low at the heights 0.2 m and 0.4 m. The relative particle RMS velocity decreases correctly with the height of the riser and a small increase of the turbulence in the shear layer is obtained in the simulation. The model calculate correctly the highest turbulence for the smallest particles (solids phase I).

A gas/solids flow system like a circulating fluidized bed will never reach a normal steady state condition. The system will exhibit a fluctuating behavior. In modelling such systems, the kinetic theory for granular flow takes care of the small scale fluctuations which are present. The large scale fluctuations are also simulated. *Figure 5.13* and *figure 5.14* show the calculated large scale velocity fluctuations for each solids phase at the center line, 0.2 and 0.7 m above the gas inlet, respectively. The fluctuations are plotted for the 10 first seconds of real time and with a superficial gas velocity of 1.0 m/s. The large scale velocity fluctuations have the same frequency and the relative velocity between the solids phases is nearly constant. A wide range of particle velocities is observed, including positive and negative velocities. In the experiments the large scale fluctuations were easy to observe visually.

The large scale fluctuating flow behavior of a circulating fluidized bed will obviously also lead to a fluctuating mean diameter. The computed fluctuating diameter at the centerline, 0.4 m above the gas inlet is shown in *figure 5.15*. The frequency of the diameter fluctuations have the same order of magnitude as the velocity fluctuations. The number averaged diameter fluctuates between 120 and 145 μm.

These large scale velocity fluctuations as well as the small scale fluctuations are included in the measurements of the particle RMS velocity profiles. Hence the computed RMS velocity from the granular temperature cannot be compared directly with the measured RMS velocity. The computed large scale fluctuations give rise to an extra RMS velocity which is added to the RMS velocity from the granular temperatures. The total RMS velocity is compared against the experimental data in *figure 5.16*. Although the large scale fluctuations seem to be significantly, they have only minor effects on the total particle RMS velocity of each phase. The large scale velocity fluctuations are highest and have most influence on the total RMS velocity in the shear layers.

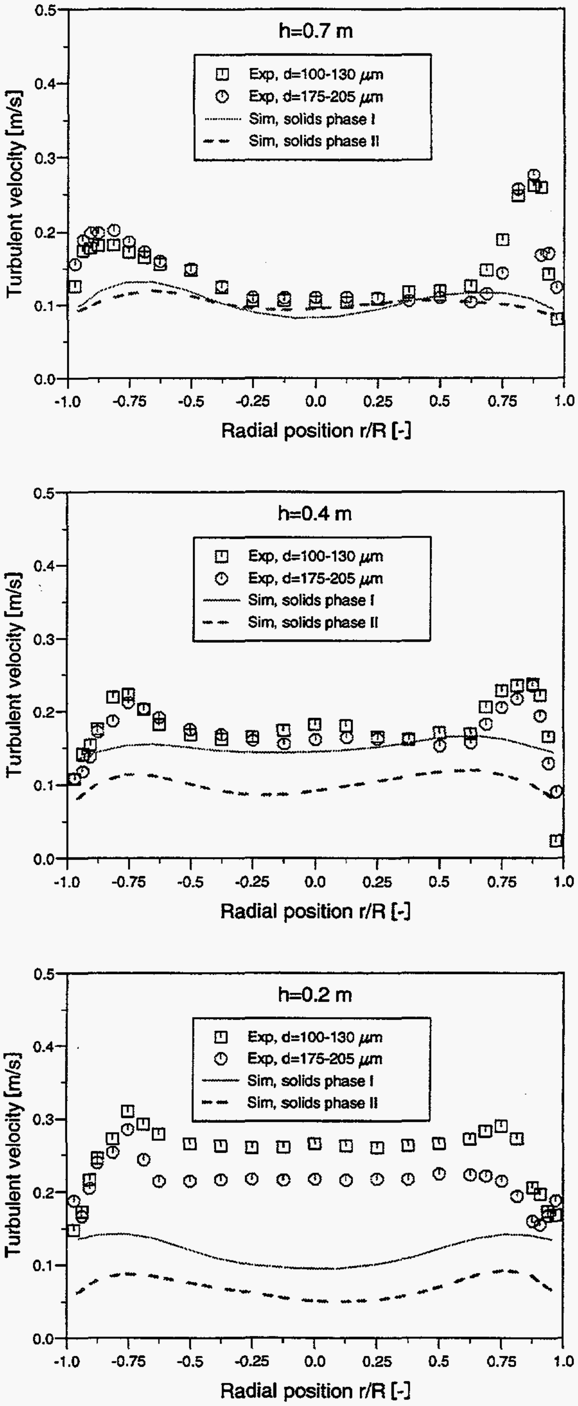

Figure 5.12: Particle RMS velocity profiles at different heights, V_{SUP}=1.0 m/s.

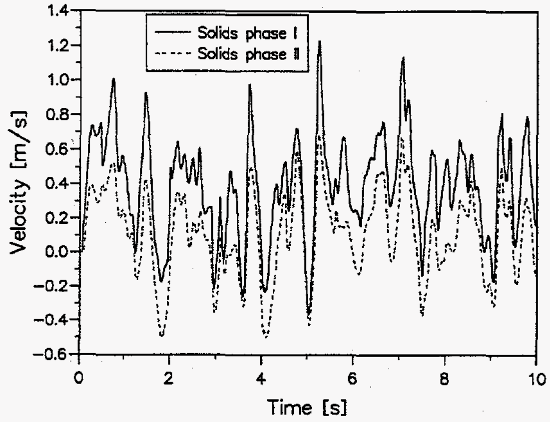

Figure 5.13: Large scale velocity fluctuations, h=0.2 m, V_{SUP}=1.0 m/s.

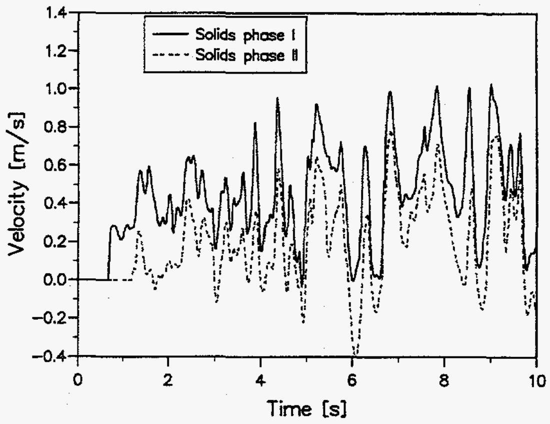

Figure 5.14: Large scale velocity fluctuations, h=0.7 m, V_{SUP}=1.0 m/s.

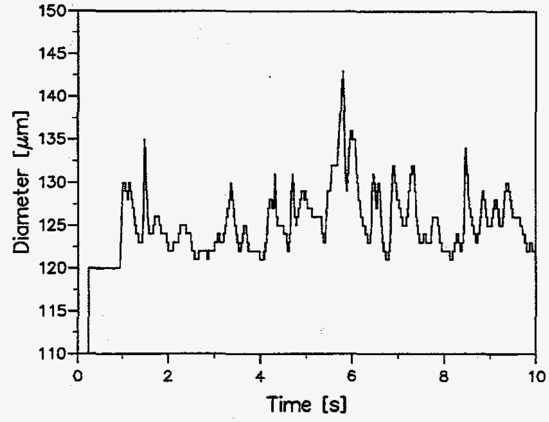

Figure 5.15: Diameter fluctuations, h=0.4 m, V_{SUP}=1.0 m/s.

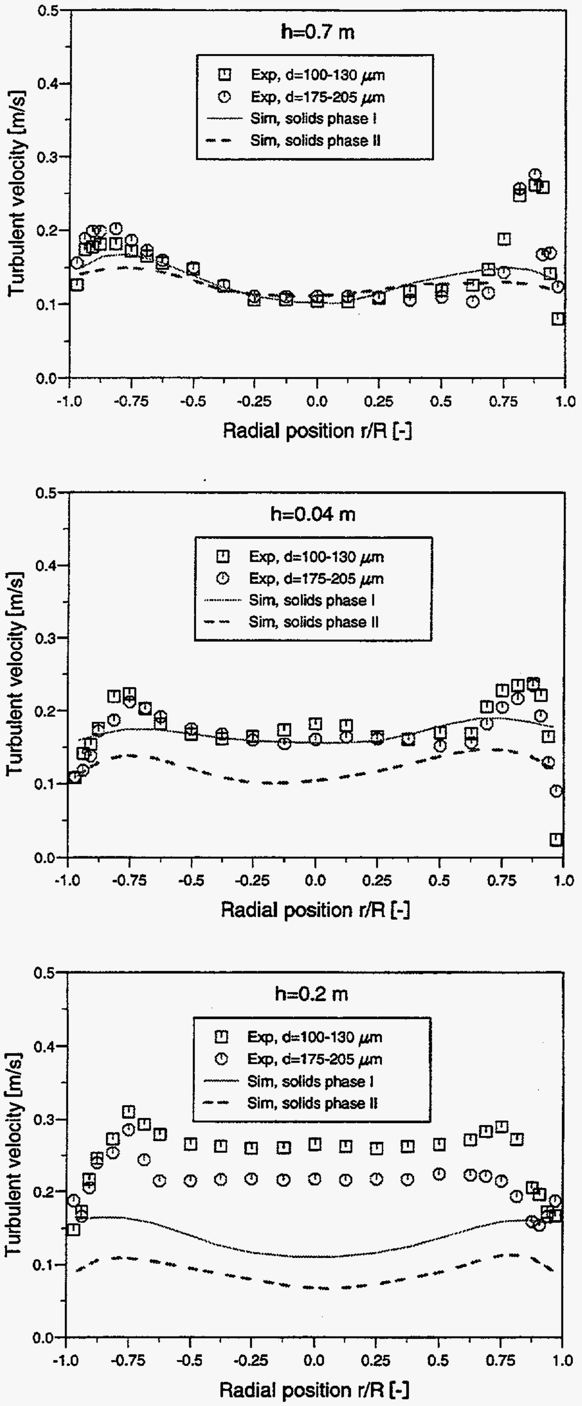

Figure 5.16: RMS velocity profiles added large scale fluctuations at different heights, V_{SUP}=1.0 m/s.

5.4 Dependence of Flow Parameters

In a CFD model there will always exist parameters and conditions which determines the quality of the prediction. In the model proposed in this work, the constants in the particle-wall boundary conditions and the coefficient of restitution coefficient are the model parameters which are most doubtful. A closer discussion of these factors follows next.

5.4.1 Particle-Wall Conditions

Although the existence of electrostatic forces in the measurements were evident, the particle-wall collisions may have significant effects on the flow behavior. In the preceding simulations the particle-wall interactions and collisions were neglected. A no-slip condition was used for the gas phase as well as the solids phases and a zero gradient condition for the turbulent kinetic energies.

A simulation, with particle-wall collisions included in the model, is also performed. The wall conditions described by *eq. (4.9)* and *(4.10)* with a specularity factor and particle-wall restitution coefficient of 0.40 and 0.85 respectively, are used. A zero flux condition is still used for the volume fraction and pressure equations. The simulation is performed with a superficial gas velocity of 1.0 m/s.

Figure 5.17 shows the particle RMS velocity profiles at the three heights. The simulation results are not added the large scale fluctuations, so the figure is directly comparable to *figure 5.12*. A comparison shows a decrease of the RMS velocity at height 0.2 and 0.4 m. The turbulent kinetic energy flux at the wall consists of a production and a dissipation term. From the figures the dissipation seems to be larger than the production of turbulence in the wall region. This also affects the turbulence in the core region. The relative particle RMS velocity decreases slightly when including wall effects.

The wall effects will naturally have influence on the particle velocity profile. The new obtained velocity profiles are plotted in *figure 5.18*. The effects of the wall functions are clearly shown. Although a typical core-annulus flow behavior is computed, the velocity closed to the wall is underpredicted. The particle-wall interactions and collisions give rise to an increase of the shear viscosity and shear stress. Thus a reduced negative velocity closed to the wall is obtained. In the central part of the riser, just minor changes are observed.

The change of the RMS and mean velocities influence further the mean diameter. In *figure 5.19* the predicted mean diameter profiles are given. A small change of the mean diameter is observed at height 0.2 m. At height 0.4 and 0.7 m just insignificant differences are observed. The wall effects have no influence on the computed mean diameter in the wall regions.

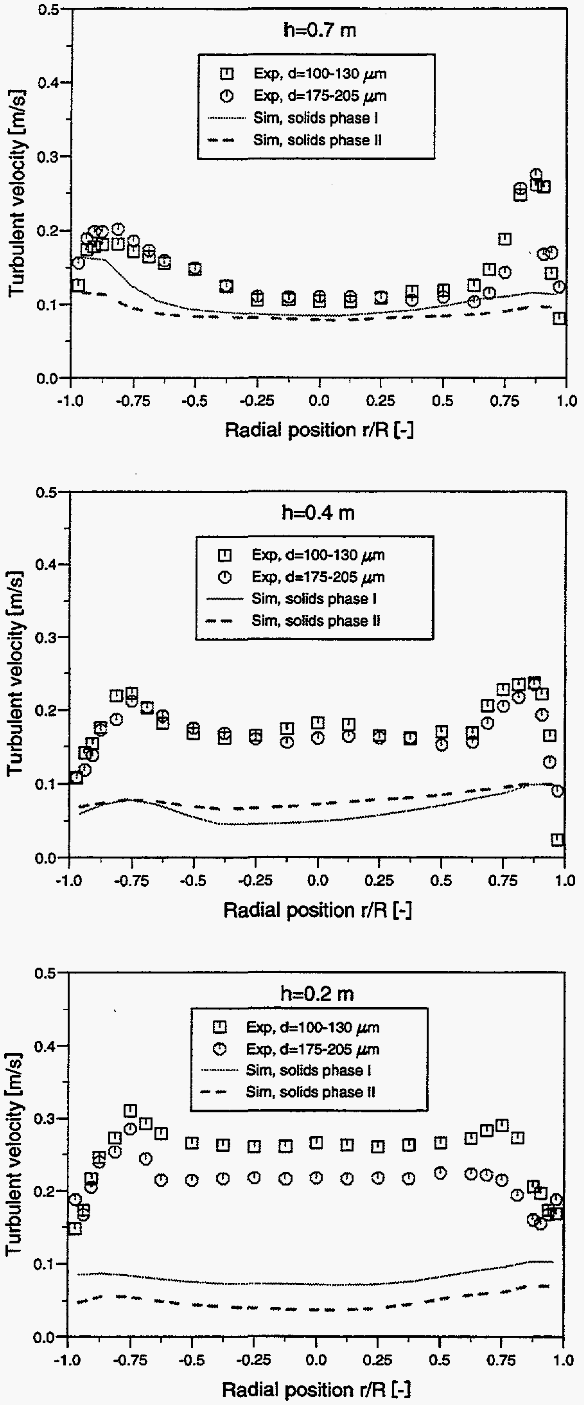

Figure 5.17: RMS velocity profiles included particle-wall collisions, V_{SUP}=1.0 m/s.

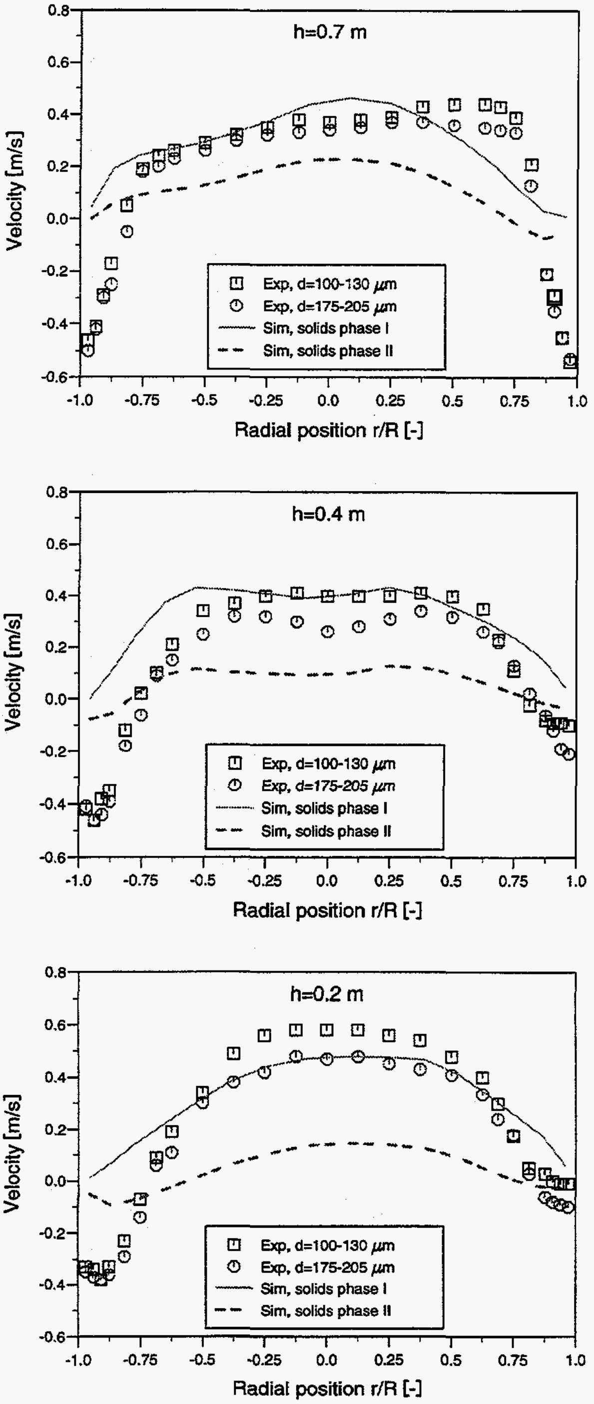

Figure 5.18: Particle velocity profiles included particle-wall collisions, V_{SUP}=1.0 m/s.

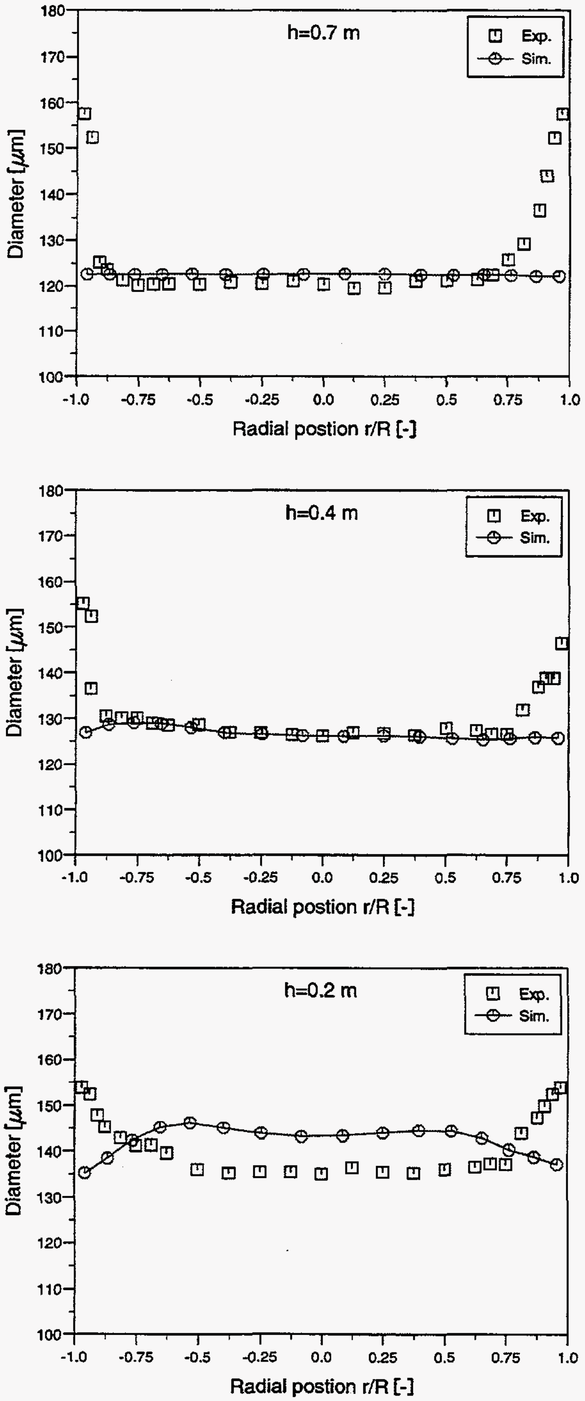

Figure 5.19: Mean particle diameter profiles included particle-wall collisions, V_{SUP}=1.0 m/s.

5.4.2 Restitution Coefficient

Beside the wall functions, the restitution coefficient is the only parameter in the model which may be varied. The restitution coefficient is unity for fully elastic collisions and zero for inelastic collisions. Johnson (1985) showed that the restitution coefficient is a function of the material properties as well as the impact of velocity. Indeed, the data he summarized show that for hard materials, the restitution coefficient is nearly one for impact velocities of 0.5 m/s and less. The turbulent velocities in *figure 5.12* give impact velocities in this order of magnitude. To be able to see how the value of the restitution coefficients will affect the turbulence, two simulations with different restitution coefficient of 0.9 and 0.999 are performed. The particle-particle restitution coefficients are the same for both solids phases. The superficial gas velocity used in the comparative simulations is 1.0 m/s.

A comparison of the computed turbulent velocities is given in *figure 5.20*. As the figure shows, the turbulent velocity varies just insignificantly in form and magnitude. When the restitution coefficient increases, dissipation due to particle-particle collisions decreases and turbulence production slightly increases, since the dissipation and production are proportional to $(1-e^2)$ and $(1+e)$ respectively. This should give an increase of the turbulence when the restitution coefficient increases. However in a very dilute gas/solids flow system that is considered in these simulations, the particle-particle collisions are of less importance. The dissipation is mainly caused by the interactions with the gas phase. Hence the value of the restitution coefficient is of minor interest in a very dilute gas/solids system.

Samuelsberg and Hjertager (1996a) did a similar analysis of varying the restitution coefficient and its affect on the turbulent kinetic energy in a dilute gas/solids system. They neglected the dissipation due to interaction with the gas phase and found that the RMS velocity undergoes a relative great change in form and magnitude when the restitution coefficient increases from 0.99 to 0.999. Actually, the difference was roughly 1 m/s.

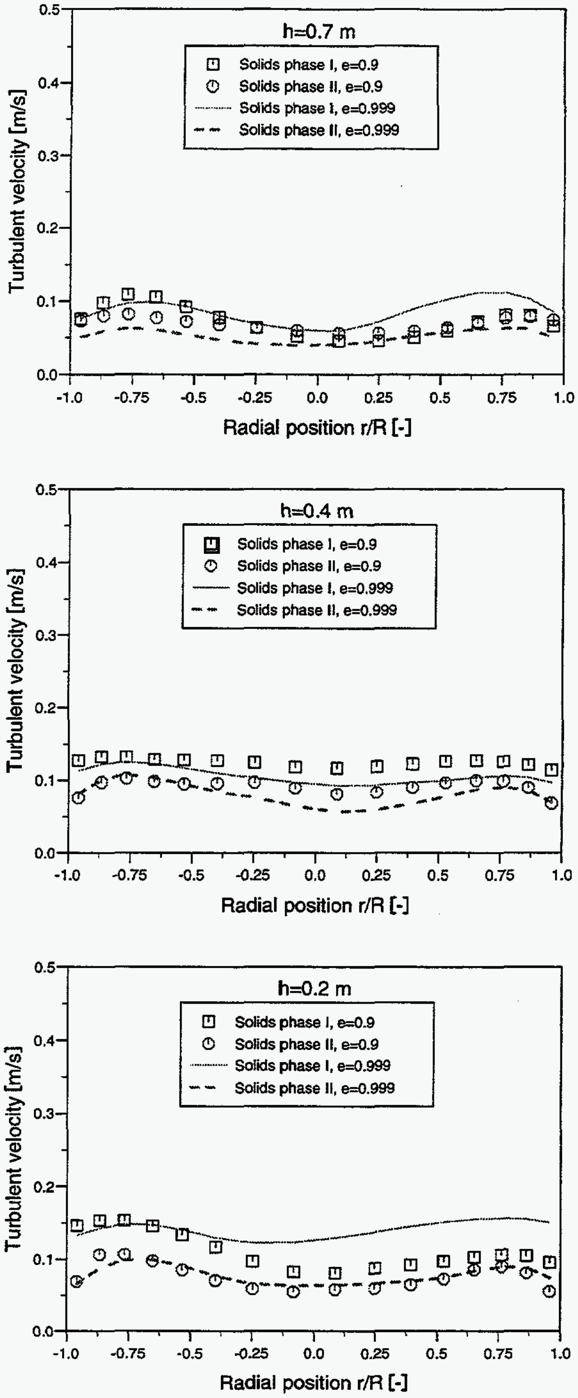

Figure 5.20: RMS velocity profiles for different restitution coefficients, V_{SUP}=1.0 m/s.

5.5 Summary

An extensive experimental study of the flow behavior of group B particles in a cold flow laboratory scale circulating fluidized bed using LDA and PDA is performed. Mean and RMS particle velocities are obtained for two different particle sizes. In addition, solids volume fraction and mean diameter are measured. The experimental results are analyzed and may be summarized as follow:

- A typical core-annulus flow behavior is observed in the riser.
- A relative particle velocity between small and larger particles is measured. The relative velocity is largest in the center of the riser and decreases toward the walls.
- The turbulent velocity is almost constant in the center of the riser and increases in the shear layer.
- A relative particle RMS velocity is observed in the lower part of the riser. Smaller particles fluctuate more than larger ones. In the upper part of the riser, the turbulent velocity seems to be nearly independent of the particle size.
- The solids concentration is dilute in the core region and denser in the annulus zone.
- An axial segregation by size is shown. The axial segregation decreases when the superficial gas velocity increases.
- A significant radial segregation of the mean diameter is shown, a behavior which seems not to be observed or reported in earlier studies of fluidized beds. The mean diameter is almost constant in the center of the riser and increases drastically toward the walls. The radial diameter distribution is most uniform in the most dense region.

The circulating fluidized bed loop is simulated using a two-dimensional Cartesian coordinate system. Two solids phases are used to describe two distinct particle groups. The simulations are in a fairly good agreement with the measurements. The core-annulus flow is correctly computed and the solids concentration seems to be relative well predicted. However the relative velocity between the solids phases is somewhat overpredicted. This may be due to the underestimated turbulent kinetic energy in the lower part of the riser, since the particle-particle drag is proportional to the square root of the granular temperature. In the upper part of the riser the computed turbulence has a correct form and magnitude, although the turbulence in the shear layer is somewhat too low.

For different superficial gas velocities the mathematical model is capable of estimating the axial segregation by size very well. But the model is not able to predict the significant radial variation of the mean diameter. The underestimation of the turbulence in the lower part may be a reason for the discrepancy between measured and simulated mean diameter in the wall region. The radial segregation may also be a result of external forces which are not included in the mathematical model.

The large scale fluctuations which occur in a gas/solids flow system are calculated and added to the small scale fluctuations obtained by the granular temperature. Although the large scale fluctuations seemed significantly, they increased the total particle RMS velocity very little. The model calculate correctly higher level of turbulence for the largest particles.

A closer investigation of wall effects is conducted. The wall effects change the particle velocities in the annulus region significantly, but did not change the flow behavior, segregation by size or had other considerable effects on the flow pattern.

It is shown that the magnitude of the restitution coefficient is not important in a dilute gas/solids system. In a very dilute gas/solids flow system the dissipation is mainly caused by interactions with the gas and not by particle-particle collisions.

CHAPTER 6

2D MODELLING OF A PILOT SCALE CFB

Scientists at "Institut Universitaire des Systemes Thermiques Industriels, Universite Provence U.R.A", France have done extensive experimental investigations of a cold flow pilot scale circulating fluidized bed. Some of the results have been reported by Tadrist et al. (1993), Azario et al. (1995) and Tadrist and Van den Moortel (1996).

A two-dimensional Cartesian coordinate system and three solids phases are used in the modelling of the flow pattern in the circulating fluidized bed system. The simulation results are compared against experimental results from the literature. Mathiesen et al. (1996) did a similar computational study of the same circulating fluidized bed and compared the numerical results with experimental data obtained by Tadrist et al. (1993). The authors showed that their multiphase CFD model was able to handle segregation by size and that the predicted flow behavior was in a fairly good agreement with the experimental data. In this chapter a comparison against experimental results obtained by Azario et al. (1995) is performed, since these experimental data are more extensive.

6.1 Experimental Setup

A detailed description of the circulating fluidized bed system and measurement techniques is given by Azario et al. (1993). *Figure 6.1* gives a sketch of the experimental setup.

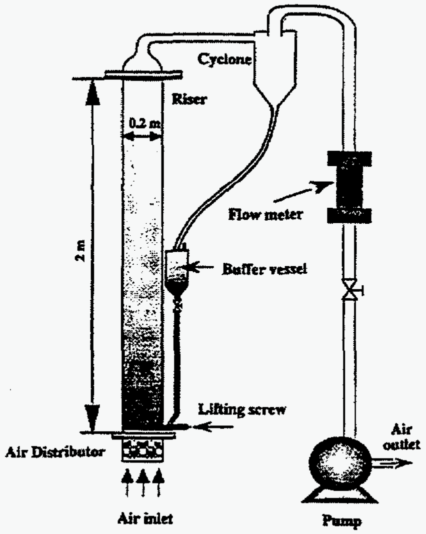

Figure 6.1: The experimental setup, Tadrist and Van den Moortel (1996).

The riser has a cross section area of 0.2×0.2 m^2 and is 2.0 m high. The primary air inlet is located at the bottom of the riser where the gas is passing through an air distributor to provide a uniform flow of air. The air has ambient temperature and pressure. At the top of the riser the suspended particles enter a cyclone and are recycled via a return loop.

Azario et al. (1995) used LDA and PDA measurement techniques to measure flow parameters, such as mean diameter, flux, mean and fluctuating velocity. The experiments were performed with two different particle size distributions, whereas the mean particle diameter was held constant. The measurements were conducted with two different superficial gas velocities, 0.7 and 1.0 m/s respectively. The initial solids concentration in the gas/solids system was dilute with a solids concentration of 1 and 3 % of the riser volume.

It should be noted that all experimental data presented in this chapter are obtained and reported by Azario et al. (1995).

6.2 Numerical Flow Parameters, Initial and Boundary Conditions

The simulation geometry with internal obstructions and grid nodes are shown in *figure 6.2*. The two-dimensional calculation domain is divided into 38×102 grid nodes, in radial and axial direction respectively. The grid is chosen to be uniform in axial direction, whereas a non-uniform grid is used in radial direction in order to have smaller control volumes where the gradients are large.

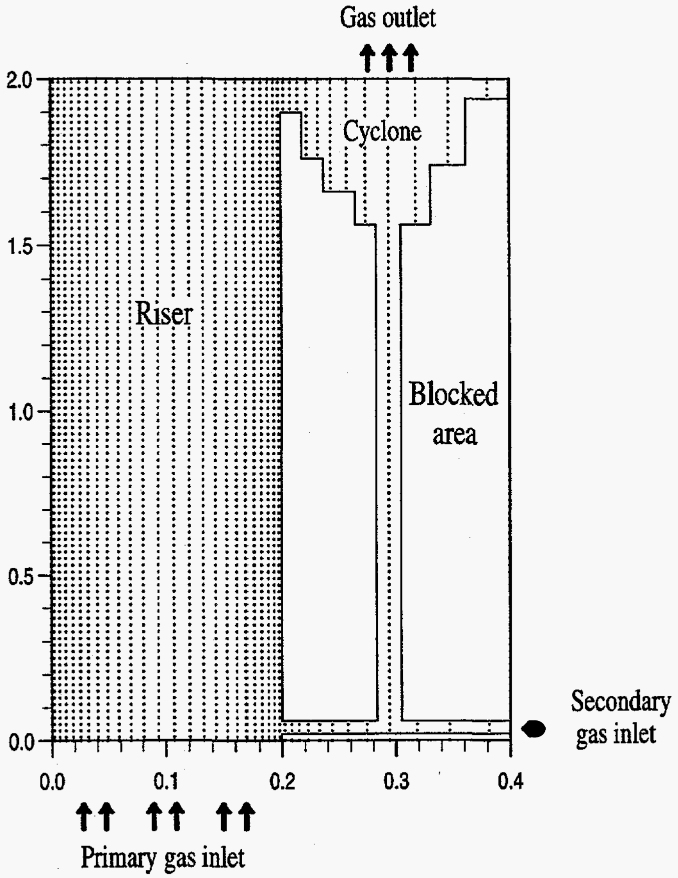

Figure 6.2: Simulation geometry with internal obstructions and grid points.

To enable a realistic particle size distribution, three solids phases are used in the simulations. *Table 6.1* and *6.2* give an overview of the numerical particle size distributions as well as the flow parameters for the two experimental particle size distributions which are considered in this chapter. The Sauter mean particle diameter is held constant at 120 μm and the standard deviations are 18 and 40 μm respectively.

Figure 6.3 shows the numerical and real particle size distribution with a standard deviation of 18 μm. A comparison shows that with three solids phases, the CFD-model are able to describe the real particle size distribution fairly well.

	Solids phase I	Solids Phase II	Solids Phase III
Mean diameter [μm]	84	120	156
Fraction of particles [%]	12.5	75.0	12.5
Density [kg/m^3]	2400	2400	2400
Form factor [-]	1.00	1.00	1.00
Restitution coefficient, solids [-]	0.99	0.99	0.99
Courant number [-]	1.00		
Maximum total volume fraction of solids [-]	0.63		

Table 6.1: Flow parameters for particles with d_{mean}=120 μm and σ=18 μm.

	Solids phase I	Solids Phase II	Solids Phase III
Mean diameter [μm]	63	120	177
Fraction of particles [%]	25.0	50.0	25.0
Density [kg/m^3]	2400	2400	2400
Form factor [-]	1.00	1.00	1.00
Restitution coefficient, solids [-]	0.99	0.99	0.99
Courant number [-]	1.00		
Maximum total volume fraction of solids [-]	0.63		

Table 6.2: Flow parameters for particles with d_{mean}=120 μm and σ=40 μm.

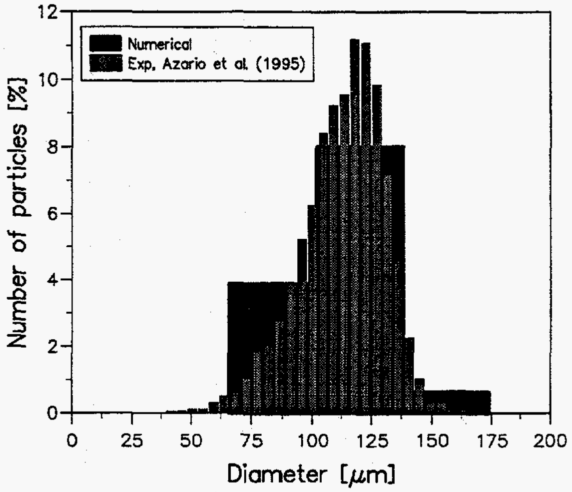

Figure 6.3: Initial particle size distribution.

In order to get reasonable computational results to compare against the experimental data, time averaged results are obtained between 16 and 20 seconds of real time.

The solids phases are initially perfectly mixed in the bed and the initial bed height depends on the concentration of solids. The glass particles are assumed spherical and thus a maximum total volume fractions of solids equal 0.63.

The air inlets are modelled as one-dimensional plug flow. The outlet are located at the top of the cyclone where a continuity condition is used for the gas phase. No particles are allowed to leave the circulating fluidized bed system. Based on earlier experience (chapter 5) about particle-wall conditions for glass particles, a no-slip condition is used for the solids phases as well as the gas phase.

6.3 Numerical Results

6.3.1 Temporal Evolutions

In order to study temporal variations of the gas/solids flow in the circulating fluidized bed, a 60 seconds real time simulation with a superficial gas velocity of 0.7 m/s, initial solids concentration of 1.0 % and a particle size distribution with a standard deviation of 18 *μm* is performed. The fluctuations are studied at the center axis, 1.0 m above the main gas inlet which are assumed to be located in the freeboard zone.

In *figure 6.4* the computed velocity fluctuations of the three solids phases are presented, whereas the measured velocity fluctuations are reproduced in *figure 6.5*. As both figures show, the circulating fluidized bed never reach a normal steady state condition, but exhibits a strong fluctuating behavior. However, the simulation shows that the system needs almost 10 seconds to reach this condition. After the first 10 seconds the fluctuations have a constant mean value and frequency. Each of the solids phases has the same frequency and the relative velocity between the solids phases seems to be almost constant. As expected the particle velocity increases with decreasing particle diameter. A somewhat wider range of velocity fluctuations are observed in the simulation compared with the measurements. The oscillating velocity includes negative and positive values, but at this position in the center of the riser, a much higher fraction of the particles are flowing upward than downward. The frequency of the fluctuations is in the same order as the experimental, but a little bit higher in the measurements than in the simulation. This may be related to that the measured velocity fluctuations include small scale as well as large scale fluctuations, whereas the computed fluctuations are only produced by the large scale effects. A closer discussion of these large scale fluctuations as well as the small scale will be treated later in this chapter.

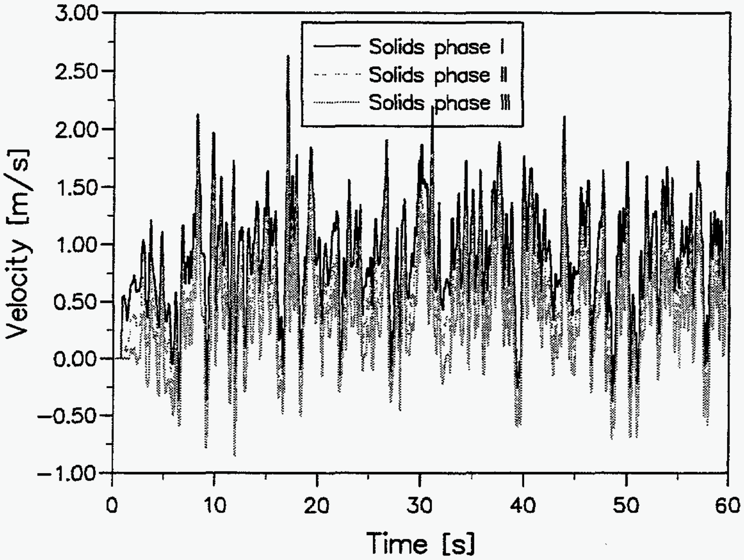

Figure 6.4: Computed large scale velocity fluctuations, h=1.0 m, V_{SUP}=0.7 m/s.

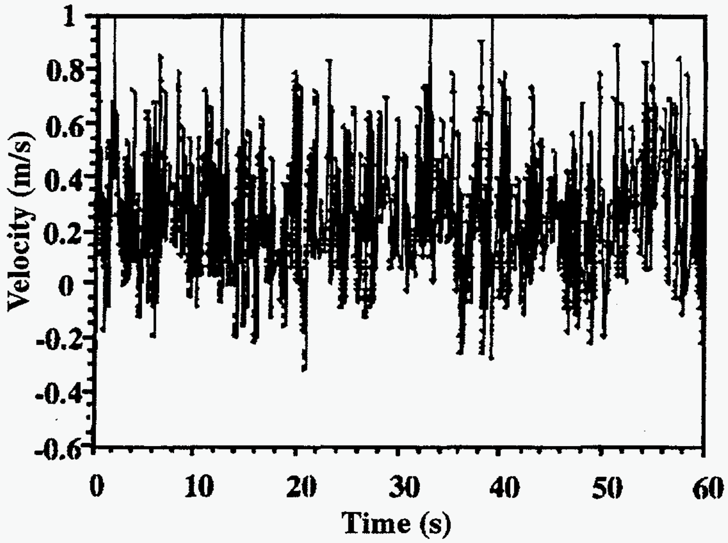

Figure 6.5: Measured velocity fluctuations, Azario et al. (1995).

Computed and measured particle diameters versus time are plotted in *figure 6.6* and *figure 6.7* respectively. The mean diameters are in a fairly good agreement and the frequency of the fluctuations seem to be in the same order of magnitude. The measured oscillations are considerably larger than the computed. This is probably because the real particle size distribution is more wide-ranging than the numerical one. With an increasing of number of solids phases, the oscillating diameter should be more correctly predicted.

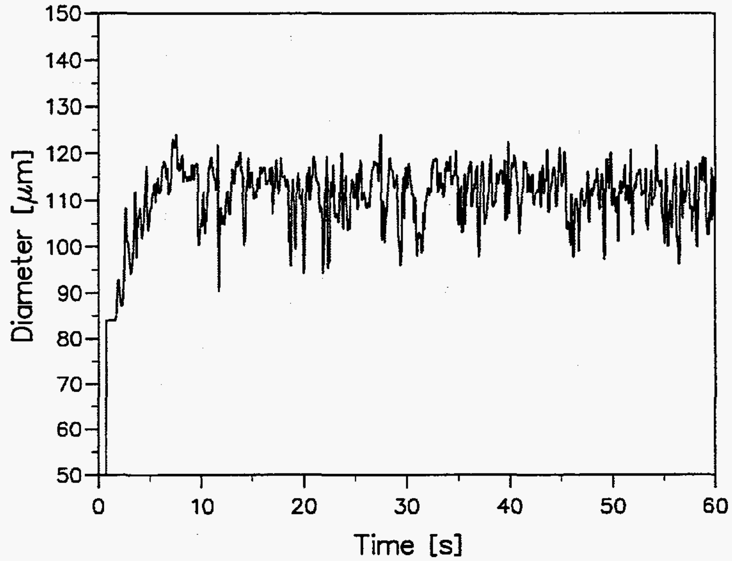

Figure 6.6: Computed diameter fluctuations, h=1.0 m, V_{SUP}=0.7 m/s.

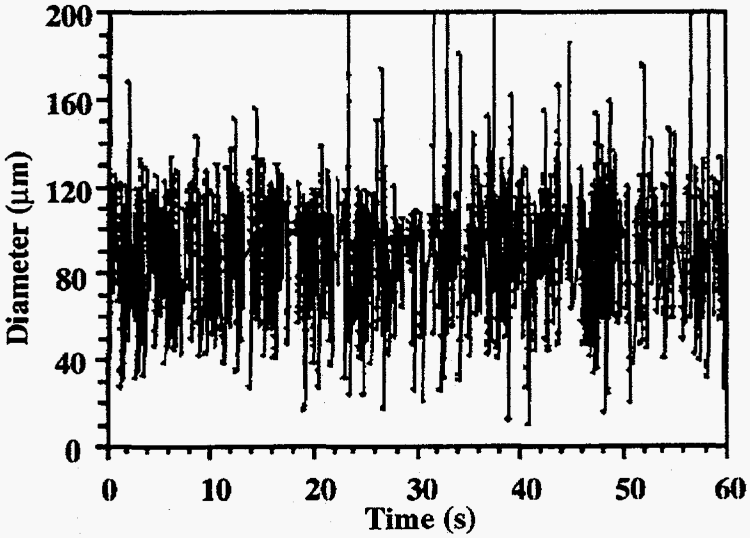

Figure 6.7: Measured diameter fluctuations, Azario et al. (1995).

The computed diameter fluctuations are related directly to the fluctuations of the volume fractions of each solids phase. The temporal evolution of the three solids volume fractions are shown in *figure 6.8*. The solids phase with a diameter of 120 *μm* and the highest initial volume fraction has also the largest magnitude of the oscillations. The frequency of the oscillations seems to be in the same order for all three phases. However the oscillations of the different solids phases are not seen to be in phase and hence the diameter fluctuations are induced.

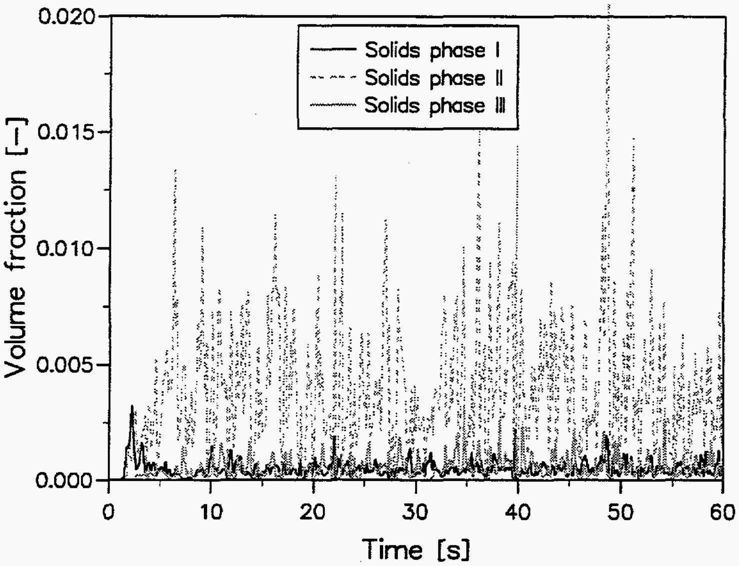

Figure 6.8: Computed solids volume fraction fluctuations, h=1.0 m, V_{SUP}=0.7 m/s.

6.3.2 Mean Diameter Profiles

In chapter 5, the axial segregation by size was shown to decrease when the superficial gas velocity increases. Another important factor that determines the magnitude of the segregation is the standard deviation of the particle size distribution. A narrow particle size distribution has obviously a more uniform mean diameter in a gas/solids flow system than a wider size distribution. Azario et al. (1995) did a comparison of the mean diameters for two different particle size distributions with a constant mean diameter and showed a significant increase in axial segregation by size when the standard deviation increased.

Simulations are performed with the two different particle size distributions and compared against the experimental data in *figure 6.9*. The figure shows the number averaged mean diameter along the median axis of the riser. The superficial gas velocity and concentration of solids are held constant at 1.0 m/s and 3 % respectively. The simulation results are in a good agreement with the experimental data and have the same form. For the narrow size distribution (σ=18), the particle size is almost constant along the median axis and only insignificant deviations from the experimental data are observed in the upper part of the riser. These deviations are probably caused by the difference in simulated and actual outlet geometry. For the larger size distribution (σ=40) the segregation by size is considerable. The multiphase model calculate a correct segregation, although the predicted mean diameters are somewhat smaller than measured.

The computed mean diameters as well as the experimental data confirm that using a large particle size distribution for the solids in the riser, an increase of the mass flow rate of fine particles will occur. Hence a lower mean particle diameter along the median axis is obtained.

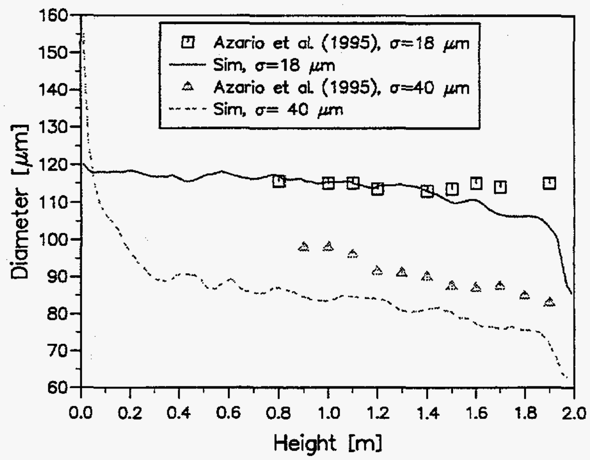

Figure 6.9: Axial particle diameter profiles for different particle size distributions.

6.3.3 Velocity Profiles

Azario et al. (1995) measured axial velocity profiles in the freeboard zone of the riser. The measurements were performed with a superficial gas velocity of 1.0 m/s, 3 % initial concentration of solids and a standard deviation of the particle size distribution of 18 μm.

Figure 6.10 shows the particle velocity profiles for different solids phases at height 1.50 m above the primary gas inlet. The computed velocity profiles are compared against a number averaged experimental velocity profile which does not separate between different particle sizes. As the figure shows, the agreement between the computed and experimental results are very good. A core-annulus flow with an almost constant velocity in the core and a downflow in the wall region is obtained.

The different solids phases have correspondingly flow behavior. The simulation shows that the smallest particle have a larger velocity than the experimental, whereas the intermediate and largest particles have a lower velocity. The relative velocity between the largest and the middle particles is somewhat larger than between the intermediate and the smallest diameters. The relative velocity is approximately 0.2 m/s in the central part of the riser and decreases toward the wall.

An overall mean particle velocity from the individual solids phase velocities is obtained in order to compare this to the experimental one. The number averaged velocity is calculated from the following relation:

$$\bar{V}_S = \frac{\frac{\alpha_1}{d_1^3} V_1 + \frac{\alpha_2}{d_2^3} V_2 + \frac{\alpha_3}{d_3^3} V_3}{\frac{\alpha_1}{d_1^3} + \frac{\alpha_2}{d_2^3} + \frac{\alpha_3}{d_3^3}} \tag{6.1}$$

where the subscripts indicate the solids phase number.

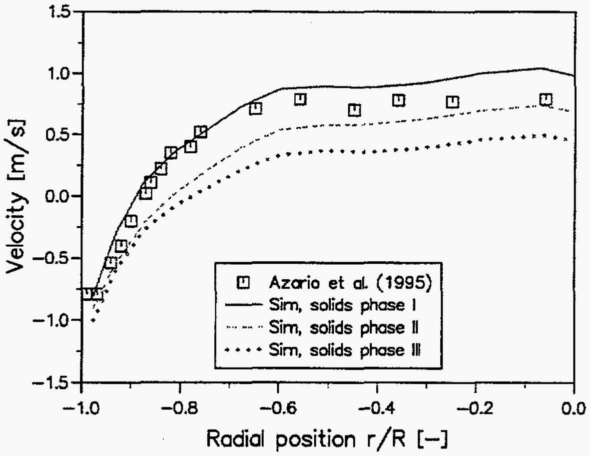

Figure 6.10: Velocity profiles for different solids phases, h=1.50 m.

In *figure 6.11*, the computed velocity profiles are compared against experimental data. The mean particle velocity profiles are obtained 1.20, 1.50 and 1.90 m above the primary gas inlet. The simulation is in good agreement with the measurements. At all three heights the core-annulus flow is correctly predicted and only insignificant deviations from the experimental data are observed. As in the experiments, the velocity profiles become flatter when the height above the inlet increases.

The radial mean velocity is plotted and compared against experimental data in *figure 6.12*. The radial velocity is obtained at height 1.20 m above the primary gas inlet and are plotted from the wall to the centerline. In this figure, the radial velocity is defined positive toward the wall from the centerline. The numerical results are in good agreement with the experiments, both in form and magnitude. The radial velocity is very low in the center of the riser, but increases toward the shear layer. If the riser is symmetrical about the median axis and a correct time averaging is performed, the radial velocity in the center should be zero. A small deviation from zero is found in the simulation.

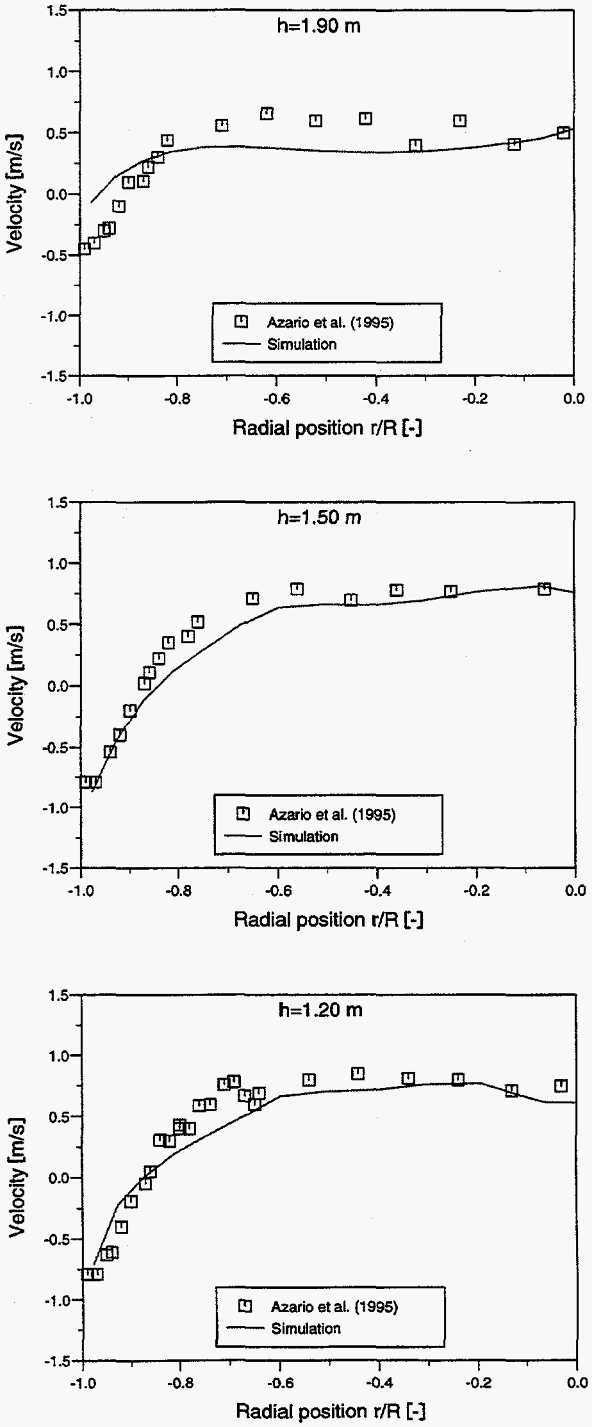

Figure 6.11: Axial particle velocity profiles at different heights.

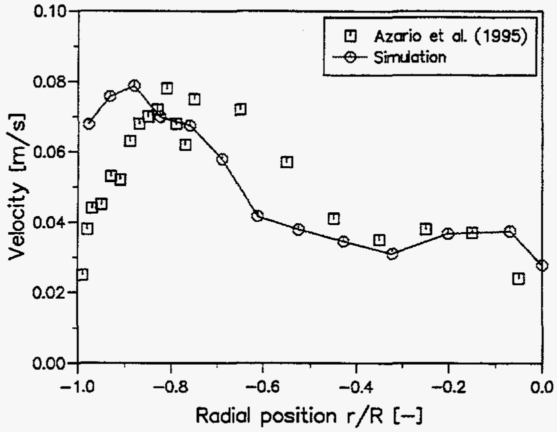

Figure 6.12: Radial particle velocity, h=1.20 m.

Different particle size distributions will cause different mean velocities. In *figure 6.13* the computed axial mean velocity along the median axis is compared against experimental data for the two particle size distributions with a standard deviation of 18 and 40 µm respectively. The simulations show the same tendency as the experiments both in form and magnitude although some discrepancies are observed. The widest particle size distribution has the largest mean velocity at the centerline.

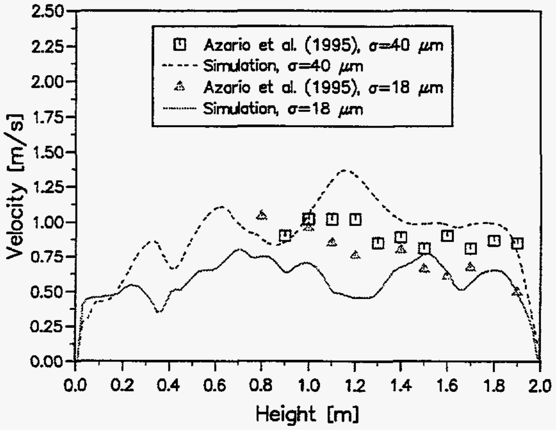

Figure 6.13: Mean particle diameter along the median axis for different particle size distributions.

6.3.4 Particle RMS Velocity Profiles

The gas/solids model is based on the kinetic theory for granular flow. The constitutive equations come from interactions of the fluctuating and mean motion of the particles. These interactions generate stresses and give rise to effective viscosities for the solids phases which relate the random fluctuating motions to the mean motions of the solids phases. In the derivation of the kinetic theory and in the definition of the granular temperature, an isotropic behavior of the particle fluctuations are assumed. Thus the axial and radial fluctuations should be the same. Azario et al. (1995) showed experimentally that the magnitude of the axial and radial velocity fluctuations are quite different.

In the multiphase gas/solids flow model a turbulent velocity is obtained for each solids phase and hence not directly comparable to the experimental data. A number averaged granular temperature is estimated from the individual granular temperatures. The turbulent velocity obtained from this granular temperature is considered as the small scale turbulence.

Large scale fluctuations are the fluctuations of the mean velocity as showed in *figure 6.4*. The small and large scale fluctuations are assumed statistical independent and hence a total particle RMS velocity may be obtained:

$$V_{RMS} = \sqrt{3\bar{\theta}_S + \frac{\frac{\alpha_1}{d_1^3}\sigma_1^2 + \frac{\alpha_2}{d_2^3}\sigma_2^2 + \frac{\alpha_3}{d_3^3}\sigma_3^2}{\frac{\alpha_1}{d_1^3} + \frac{\alpha_2}{d_2^3} + \frac{\alpha_3}{d_3^3}}} \qquad (6.2)$$

where the standard deviation σ_s of each solids phase is given by:

$$\sigma_s = \frac{1}{(N_i - 1)}\sum_{i=1}^{N_i} (v_i - \bar{V}_S)^2 \qquad (6.3)$$

Experimental studies show a non-isotropic behavior of the fluctuations in a gas/solids system, and that an assumption of isotropic granular temperature is not desirable if these fluctuations are the only oscillation of the system. However it is reasons to believe that the granular temperature only capture the small scale fluctuations which will occur in a gas/solids system. The existence of large scale fluctuations was clearly and evidently showed by *figure 6.4* to *6.8* and is also easy to observe visually in a gas/solids flow system. That the simulation never reach a normal steady state condition indicates also that there exist fluctuating effects as the granular temperature is not able to capture.

There are no doubt that large scale as well as small scale fluctuations are included in the measurements. Computed turbulent velocity from small and large scale fluctuations are compared against the experimental data in *figure 6.14* and *6.15*, for radial and axial direction respectively.

Figure 6.14 shows a significant difference in the computed radial RMS velocity whether the large scale fluctuations and are added or not. The small scale fluctuations have an almost constant value in the central part of the riser and increase significantly in the wall region. A comparison between the experimental data and the numerical small scale turbulence shows that it is correctly predicted in the wall region, whereas quite significant discrepancies are obtained in the core region. In such a dilute gas/solids system which are considered in this simulation, the granular temperature is mainly produced by the shear forces and hence largest in the annulus zone. When adding the large scale turbulence, the curve changes both in form and magnitude. A more constant and correct turbulence behavior is obtained and the agreements with the measured RMS velocities are fairly well.

In *figure 6.15* the experimental data show that the axial velocity fluctuations are approximately three times the radial RMS velocity. The computed small scale turbulence is significantly too small according to the experimental data. By adding the large scale turbulence, a correct order of magnitude is obtained although some deviations still are observed. The figures show further that the large scale fluctuations are significant higher in the axial than in the radial direction.

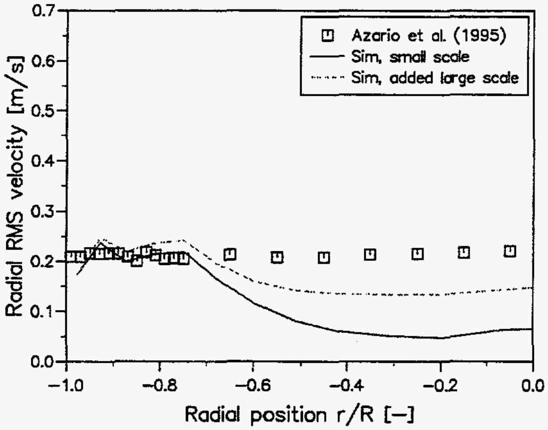

Figure 6.14: Radial RMS velocities, h=1.20 m.

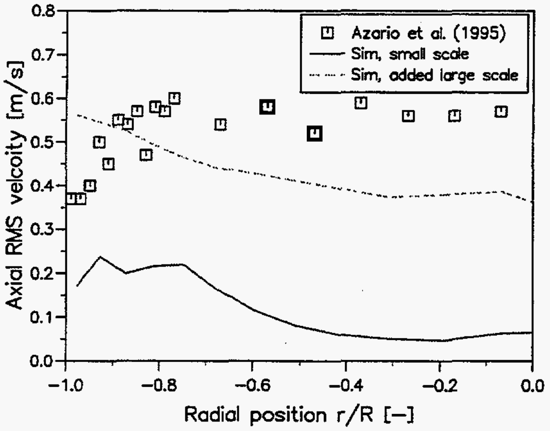

Figure 6.15: Axial RMS velocities, h=1.20 m.

6.3.5 Mass Flux Profiles

Azario et al. (1995) also measured and reported net mass flux profiles at three different heights. Flux profiles are computed and compared against these experimental data in *figure 6.16*. The computed fluxes are the sum of the individual solids phase fluxes. The flux profiles are obtained with a superficial gas velocity of 1.0 m/s, a standard deviation of the particle size distribution of 18 μm, 3 % initial solids concentration, and 1.2, 1.5 and 1.9 m above the main gas inlet.

The simulation shows a fairly good agreement with the experimental data. Best agreement are obtained at height 1.90 m above the primary gas inlet and this indicates that the total solids flux circulating in the loop is reasonably predicted.

At height 1.20 and 1.50 m above the inlet, larger discrepancies are obtained. The CFD model compute a too high flux upward in the core region, whereas a too high negative net flux is computed in the annulus region. This results indicate that a too large axial mixing is computed, although the total net flux seems to be reasonable.

The particle velocity profiles presented in *figure 6.11* showed a very good agreement with the experimental data. These profiles together with the net flux profiles indicate that the presence of solids at heights 1.2 and 1.5 m is somewhat too high. The volume fractions of solids is a little too high in the core as well as in the annulus region and probably the bed height is somewhat overpredicted.

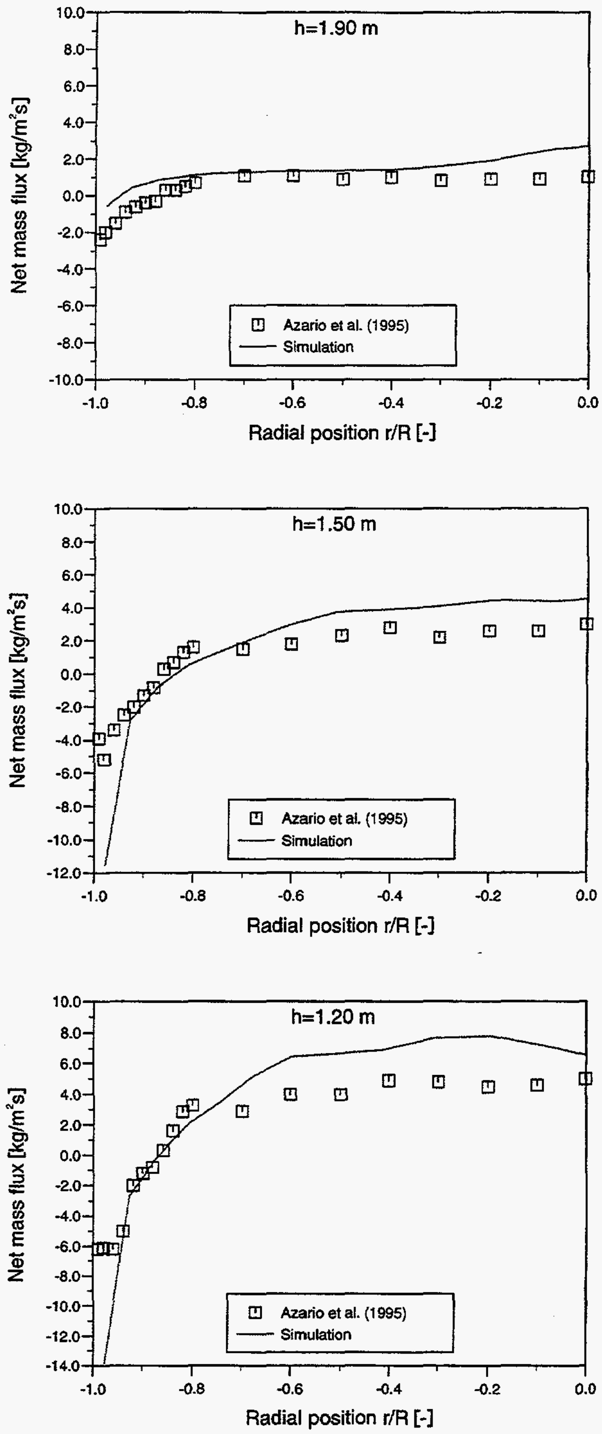

Figure 6.16: Net solids flux profiles at different heights.

6.4 Summary

Two-dimensional simulations of a pilot scale circulating fluidized bed are performed. The computational results are compared against experimental results reported in the literature. The simulations are performed with different superficial gas velocities, initial solids concentrations and standard deviations of the particle size distribution. Most emphasis is given to study the effects of different particle size distributions and to study the fluctuating behavior of the dilute gas/solids flow system. Altogether the simulation results are in a very good agreement with experimental data.

It is shown that the CFD model is able to capture the large scale fluctuations which will evidently be present in a circulating fluidized bed system. The large scale fluctuations of mean velocities, volume fractions and mean diameter are monitored and compared against experimental results. Both the frequency of the fluctuations and the size of the oscillations are of the correct order of magnitude.

Axial and radial large scale fluctuations are calculated and added to the small scale turbulence from the isotropic granular temperature. The computed small scale turbulence are significantly too small according to the experimental data. By adding the large scale fluctuations a correct order of magnitude is obtained, although some discrepancies still are observed. The calculations confirm that the axial fluctuations are much larger than the radial fluctuations and hence the fluctuating behavior of the circulating fluidized bed is evidently not isotropic.

Simulations are performed with two different particle size distributions and compared against experimental data along the median axis of the riser. The computed mean diameters are in good agreement with the experimental data both in form and magnitude. For the narrow size distribution, the particle diameter is almost constant along the median axis, whereas for the wide-ranging particle size distribution, a significant segregation by size is correctly predicted.

The axial velocity along the median axes are calculated for the two different particle size distributions as well. The simulations show the same tendency as the experiments, although some discrepancies are observed. A higher velocity is correctly obtained for the large particle size distribution.

Mean particle velocity profiles are obtained at three different heights with only insignificant deviations from the measurements. A typical core-annulus flow is calculated with a nearly constant velocity in the central part of the riser and a down flow of particles in the wall region. As in the experimental data, the velocity profiles became flatter when the height above the inlet increases.

A mean radial velocity is calculated. The agreement with experimental velocity is very well and the results show that the radial velocity is approximately zero at the centerline, then increases toward the shear layer and further decreases to the wall.

Net mass flux profiles are computed and presented. The calculated flux profiles show a fairly good agreement with the experimental data. Best agreement is obtained in the upper part of the riser and the total flux circulating in the loop seems to be reasonably predicted. At lower heights, larger deviations are obtained. The CFD model compute a little too high flux upward in the core region, whereas a too high negative net flux is computed in the annulus region. The results indicate that the model calculates a too large axial mixing of particles.

CHAPTER 7

AN EXPERIMENTAL AND COMPUTATIONAL STUDY OF A 2" I.D. RISER

In this chapter, an experimental study of a circulating fluidized bed with FCC catalysts as the dispersed phase is conducted. The work was carried out at Illinois Institute of Technology (IIT), Department for Chemical and Environmental Engineering. The circulating fluidized bed system was first used by Yang (1991). He also modified a LDA system delivered by TSI, both the hardware configuration and the software for data acquisition and processing. In this work slight modifications of the circulating fluidized bed system as well as the LDA system are conducted. Four different flow conditions are studied, two different dilute solids loading, each with two different superficial gas velocities. Particle diameter, mean and RMS velocity measurements of FCC catalysts using LDA are conducted.

A computational study of the riser section of the circulating fluidized bed is done. The simulations are performed with a two-dimensional Cartesian coordinate system and three phases, one gas and two solids phases.

7.1 Experimental Setup

7.1.1 Circulating Fluidized Bed

A sketch of the circulating fluidized bed system is shown in *figure 7.1*. The internal diameter of the clear PVC riser is 0.0508 m (2 inches) and 2.75 m (9 feet) high. The test section is located 1.12 m over the elbow inlet, where a pair of optical glass window is mounted to ensure a good optical signal.

At the top of the riser, the suspended particles enter a two-stage cyclone where they are recycled back to the riser via a return loop.

The gas inlet consists of air filters, pressure regulator and flowmeter. The air has pressure of 1 bar and ambient temperature at the inlet.

The FCC catalysts have a density of 1700 kg/m^3. The particle size distribution is very wide-ranging with particles from 11 to 180 μm. The effective number mean and Sauter mean diameter are approximately 27 and 55 μm. According to Geldart's classification, the FCC catalysts are typically group A, aeratable particles, Geldart (1973).

Four different flow conditions are studied. Two superficial gas velocities are used, 0.7 and 1.4 m/s respectively, each with 100 and 400 gram loading of solids. This give an approximately concentration of solids in the circulating fluidized bed of 0.5 and 2 % respectively.

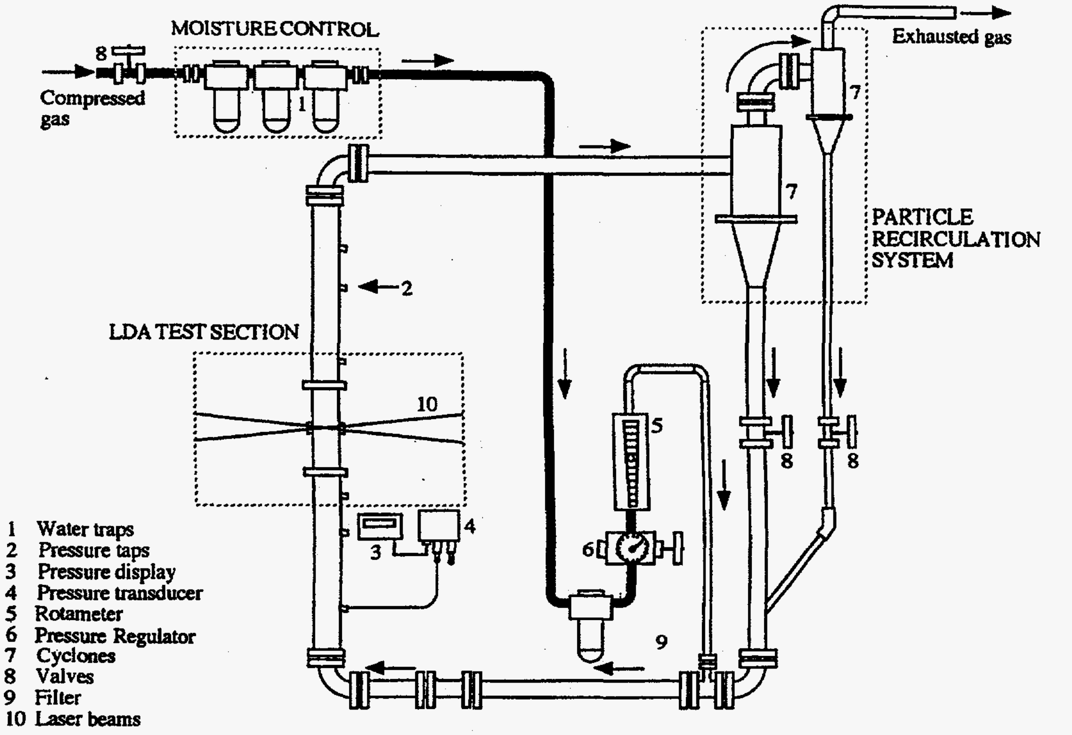

Figure 7.1: A sketch of the circulating fluidized bed system.

7.1.2 Laser Doppler Anemometry

The measurements are performed with a Helium-Neon laser with a power of 15 mW at a wavelength of 638.2 nm, delivered by TSI. The optical system is aligned in on-axis forward scatter modus. Transmitting and receiving lenses have both a focal length of 250 mm. *Table 7.1* gives an overview of the most essential LDA parameters.

Wavelength	638.2 nm
Fringe spacing	3.2 μm
Beam separation	50 mm
Focal length, transmitting lens	250 mm
Focal length, receiving lens	250 mm
Width of measuring volume	0.18 mm
Length of measuring volume	1.2 mm
Velocity range	- 1.26 to 3.28 m/s

Table 7.1: LDA parameters.

A HP5404 digitizing oscilloscope is used to record the Doppler signals, which are then transferred to an IBM compatible computer. The data acquisition and processing software developed by Yang (1991) are slightly modified.

The measurements are conducted at 13 different locations from centerline of the riser toward the wall, in the direction perpendicular to the plane shown in *figure 7.1*.

Both mean velocity, RMS velocity and particle diameter are measured. The Shape Discrimination Technique is used to estimate the diameter of the particles. The particle mixture is divided into two groups, size less and larger than the number mean size. Mean and RMS velocities are presented for each group. A slow data acquisition due to a slow computer, made it problematic to obtain reasonable results for the volume fraction of the dispersed phase.

7.2 Numerical Flow parameters, Initial and Boundary Conditions

The riser section of the circulating fluidized bed is modelled and simulated in a two-dimensional Cartesian coordinate system. A sketch of the calculation domain with grid nodes is given in *figure 7.2*. A uniform grid is used in axial direction, whereas a non-uniform grid spacing is used in the radial direction. To cover the calculation domain, 18×82 grid points are applied in radial and axial direction, respectively.

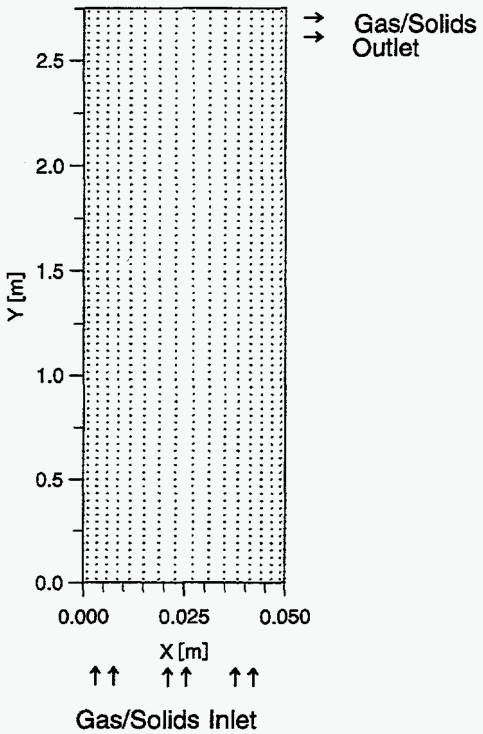

Figure 7.2: Sketch of the calculation domain with grid nodes.

The diameter of a spherical particle is uniquely defined. By dealing with non-spherical particles such as FCC catalysts, the definition of the particle diameter is more doubtful. Kunii and Levenspiel (1991) defined an effective diameter d_{eff} which is proportional to the form of the particle ψ and the diameter of a sphere having the same volume as the particle:

$$d_{eff} = \psi d_{sphere} \tag{7.1}$$

where the form factor (sphericity) is defined as:

$$\psi = \frac{surface\ of\ sphere}{surface\ of\ particle} \tag{7.2}$$

The diameter of a sphere d_{sphere} is the most correct diameter to use in the kinetic theory for granular flow as well as in the calculation of drag terms and Reynolds number.

The initial particle size distribution is obtained with the well recognized Microtrac Particle Size Analyzer. This measurement technique is based on absorption or diffraction of the scattered light intensity from a laser light source. The technique measures the projected area diameter, Ose (1996). This projected diameter will be approximately the same as the effective diameter in *eq (7.1)*.

The Shape Discrimination Technique uses the particle diameter obtained by Microtrac Particle Size Analyzer to make a calibration curve and hence this diameter is an effective diameter as well.

Kunii and Levenspiel (1991) list calculated sphericity of particles and suggested a form factor of 0.625 as typical for catalyst solids. This value are used as the form factor of the FCC catalysts in the simulations.

The real particle size distribution is modelled by using two solids phases. The experimental effective particle size distribution has an effective number mean and Sauter mean diameter of 27 and 55 μm respectively. 10 volume percent of the solids are assumed to have an effective diameter of 25 μm, whereas the other 90 percent have a diameter of 60 μm. This give an approximately correct Sauter mean diameter. Thus the equivalent diameter of the spheres are 40 and 96 μm for the two solids phases respectively. *Table 7.2* gives a summary of the flow parameters.

	Gas Phase	Solids Phase I	Solids Phase II
Mean Diameter [μm]	-	40	96
Fraction of particles [%]	-	10.0	90.0
Density [kg/m^3]	1.20	1700	1700
Form factor [-]	-	0.625	0.625
Laminar viscosity [kg/ms]	1.8E-5	-	-
Restitution coefficient, solids [-]	-	0.99	0.99
Courant number [-]	1.00		
Maximum total volume fraction of solids [-]	0.70		

Table 7.2: Flow parameters.

The riser is initially filled with a bed with a total solids volume fraction of 0.50. The initial bed height is 0.03 and 0.12 m for 100 and 400 g of solids respectively. The two solids phases are perfectly mixed.

One dimensional plug flow for the gas phase is assumed at the inlet. At the outlet, which is located at the top of the riser all the dependant variables of the solids phases are extrapolated downstream. To ensure that the overall continuity condition is satisfied, the gas phase velocities are calculated from total mass balance at the outlet. The inlet solids flux is the same as the outlet solids flux, hence a constant overall concentration in the riser is ensured.

At the walls, the no-slip condition is used for the gas phase. For the solids phases particle-wall collisions are included and described by *eq. (4.9)* and *(4.10)*. The specularity factor and particle-wall restitution coefficient are 0.5 and 0.9 respectively. A zero gradient conditions is used for the volume fraction and pressure equations.

The simulations are run for fifteen seconds real time. The time averaged results are obtained from the five last seconds of the simulations.

7.3 Experimental and Numerical Results

7.3.1 Particle Diameter Calibration Curves

When the Shape Discrimination Technique is used to estimate the particle diameter, a calibration curve must be obtained for each flow condition. The calibration curves are presented in *figure 7.3* and *figure 7.4*. All the calibration curves show a similar shape, which indicate that the particle size distribution in the test section is similar for all flow conditions. Hence there are no significant axial segregation in the riser.

The calibration curves also show that it is very important to make a new calibration curve for each flow condition. For example an amplitude of 1.6 V results in a particle diameter of 42 μm and 98 μm for constant 100 g of solids and a superficial gas velocity of 0.7 m/s and 1.4 m/s respectively.

The main reason for the differences in the calibration curves, is the variation of local particle concentrations in the test section at different flow conditions. The test section is located 1.12 m above the inlet and for a low gas velocity, as 0.7 m/s, a non-uniform axial concentration distribution of the solids will occur. When the superficial gas velocity increases to 1.4 m/s, the axial concentration distribution will be more uniformly and hence a higher solids concentration in the test section. The calibration curves confirm that the amplitude of a Doppler burst is a function of the solids concentration.

When the concentration of solids increases, the slope of the calibration curve will increase as well. The amplitude of the Doppler burst becomes more independent of the particle diameter when the solids concentration increases. Since a wide amplitude size distribution is desirable, the Shape Discrimination Technique is best suited for very dilute gas/solids flow systems.

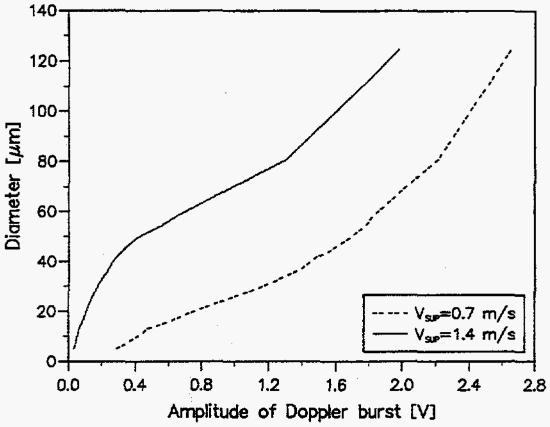

Figure 7.3: Calibration curves for 0.1 kg of solids.

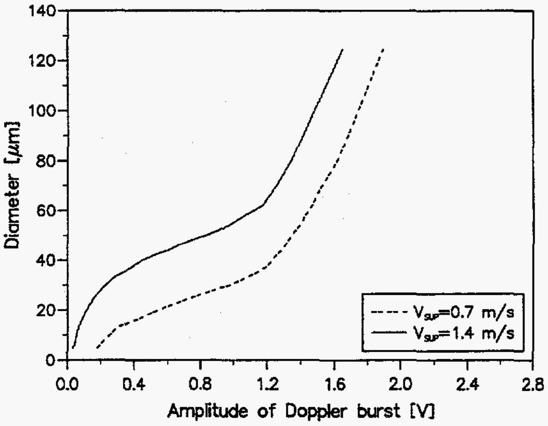

Figure 7.4: Calibration curves for 0.4 kg of solids.

The calibration curves for the particle size measurements are based upon the fundamental assumption that there are no agglomeration or axial segregation in the system. It is almost impossible to prove that there are no axial segregation, but a superficial gas velocity of 0.7 and 1.4 m/s is assumed to be sufficient to minimize axial segregation. In a dilute gas/solids flow system, agglomeration increases with the concentration of particles and/or the superficial velocity of the continuous phase. Among the above flow conditions, most agglomeration probably appears with 400 g of solids and a superficial gas velocity of 1.4 m/s. The agglomeration is mainly caused by electrostatic effects, Zhang et al. (1996). Larostat particles eliminate electrostatic forces and in turn agglomeration. Thus two experiments using 400 gram of solids with a superficial gas velocity of 1.4 m/s, one without Larostat and another one with 1 % Larostat particles mixed with the FCC are conducted. *Figure 7.5* shows a comparison of the accumulative percentage of the amplitude versus amplitude of the Doppler burst for the two situations. As the figure shows there is no significant difference between the amplitude size distribution without and with 1 % Larostat particles.

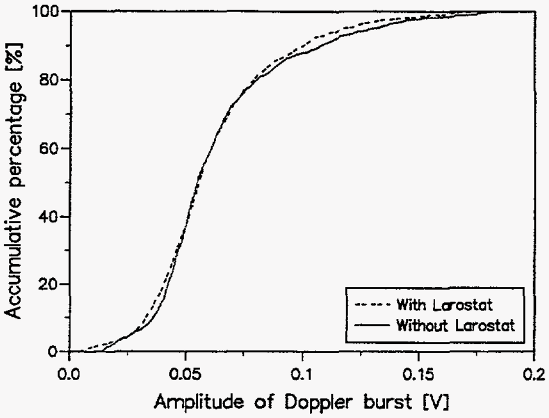

Figure 7.5: Amplitude distribution with and without Larostat particles.

Figure 7.6 gives a comparison of the measured number averaged particle diameter along the radial direction for the same flow condition. The data is plotted from the centerline toward the wall. The experimental results obtained with Larostat particles show a slightly higher particle diameter at the center of the riser and a lower estimated particle diameter near the wall in comparison with the run using no Larostat particles. The maximum difference between the local mean particle diameters in the two cases, is just about 2.5 μm. Hence there exists no significant agglomeration in the gas/solids flow system.

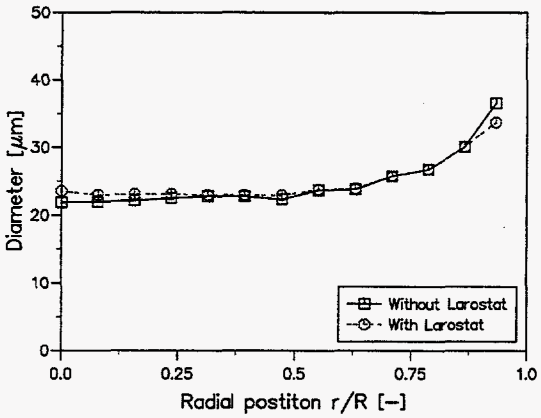

Figure 7.6: Particle diameter profiles with and without Larostat particles.

7.3.2 Particle Diameter Profiles

Figure 7.7, 7.8, 7.9 and *7.10* show the obtained number averaged diameter profiles for different flow conditions. The computed mean diameters are plotted in the same figures. Both the measured and computed diameters are an effective number diameter. The measured particle diameter profiles have the same form and magnitude for all flow conditions.

The most interesting observation in the measured particle diameter profiles is the significant difference in mean diameter between particles at the center of the riser and those near the wall. This is the same tendency as reported in chapter 5. The difference seems to increase with decreasing concentration of solids and seems to be almost independent of the gas velocity.

As indicated in chapter 5, the phenomena may be explained by the fact that smaller particles will follow the gas more effectively than larger one. Larger particles will not follow the gas effectively and start accumulating. Particularly in the wall region where the gas velocity is very low.

Also in the simulations, the mean diameter profiles have the same form and magnitude for all flow condition, but relatively large discrepancies are observed in comparison with the experimental data. The diameter is almost constant and independent of the radial position. The multiphase gas/solids flow model does not capture the radial segregation by size. The overall mean diameter has approximately the same value as the initial particle size distribution.

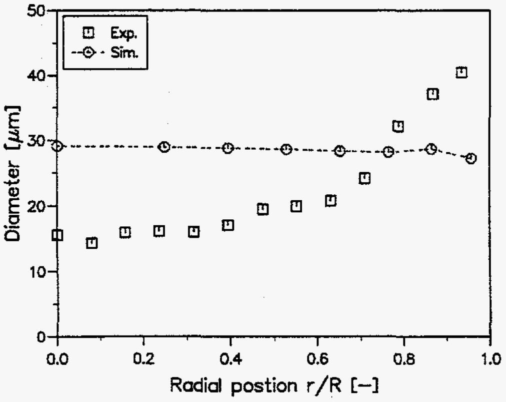

Figure 7.7: Mean particle diameter profiles, V_{SUP}=0.7 m/s, 0.1 kg solids.

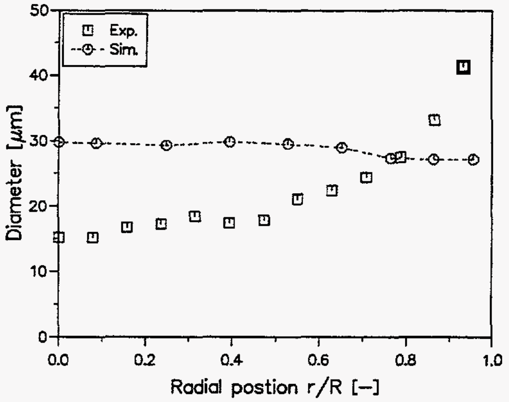

Figure 7.8: Mean particle diameter profiles, V_{SUP}=1.4 m/s, 0.1 kg solids.

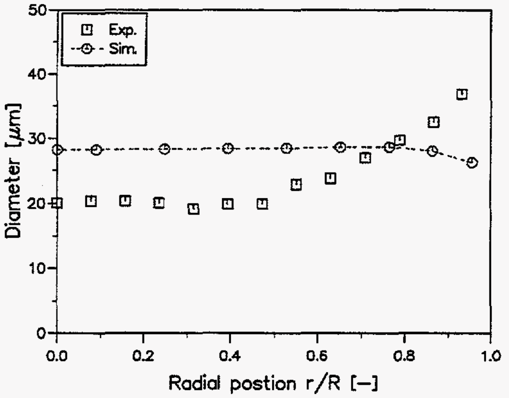

Figure 7.9: Mean particle diameter profiles, V_{SUP}=0.7 m/s, 0.4 kg solids.

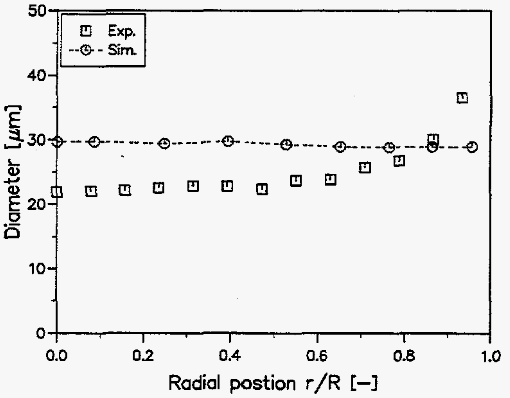

Figure 7.10: Mean particle diameter profiles, V_{SUP}=1.4 m/s, 0.4 kg solids.

The computed mean diameters are found directly from the volume fraction of the solids phases. *Figure 7.11* shows the volume fraction of the solids phases obtained with a superficial gas velocity of 0.7 m/s and 0.1 kg of solids. No volume fraction measurements are performed, but the volume fraction distribution has an expected form, dilute in the center of the riser and denser in the wall region. A behavior which is typically for dilute gas/solids flow. For both phases the concentration of solids increases from the center of the riser toward the wall, but more clearly for the largest particles.

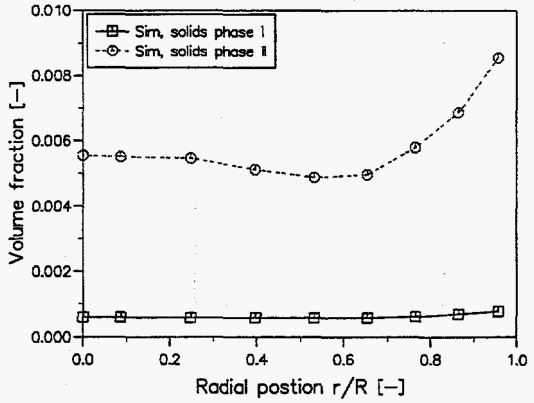

Figure 7.11: Volume fraction profiles, V_{SUP}=0.7 m/s, 0.1 kg solids.

7.3.3 Particle Velocity Profiles

The measured and computed particle velocity profiles are presented in *figure 7.12, 7.13, 7.14* and *7.15*. The particles are divided into two groups. Particles with diameter less than 27 μm, and particles with diameter larger than 27 μm, corresponding to the two solids phases.

A typical core-annulus flow behavior for the particulate phases is observed for all flow conditions. The experimental results show that in the central part of the riser, the particles flow upward with an almost constant velocity. In the wall region, the particle velocity decreases continuously from the core toward the wall. Close to the wall, a low particle velocity and in some cases reversal flow of particles are observed.

As expected the results show a relative velocity between particles of different sizes. The relative velocity between the two groups of particles that are considered in these experiments, remained almost constant across the radius. When the superficial gas velocity increases, the relative velocity between the particle groups decreases slightly.

At higher solid loadings and higher velocities, the particles show a more flat profile and in some cases (e.g. high solids loading and high gas velocity) the maximum velocity deviates from the center of the riser.

Although large discrepancies are observed between measured and computed velocity profiles, the simulations show a similar flow behavior. A typical core-annulus flow is computed with an upflow of particles in the central part of the riser and a downflow near the wall. The predicted relative velocities are in the right order of magnitude although the velocity is significantly too high in the annulus region.

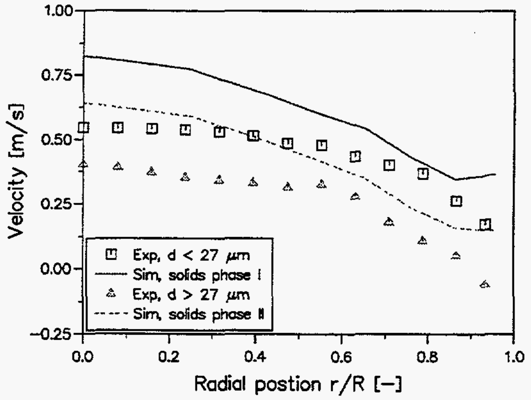

Figure 7.12: Particle velocity profiles, V_{SUP}=0.7 m/s, 0.1 kg solids.

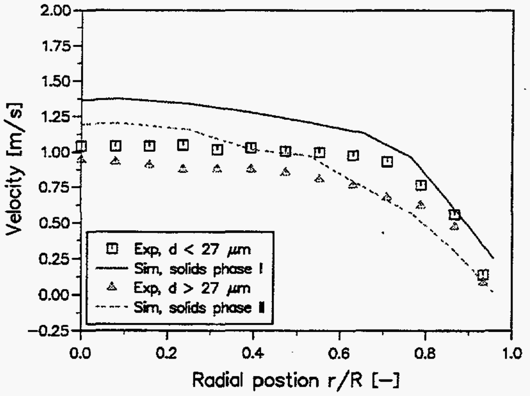

Figure 7.13: Particle velocity profiles, V_{SUP}=1.4 m/s, 0.1 kg solids.

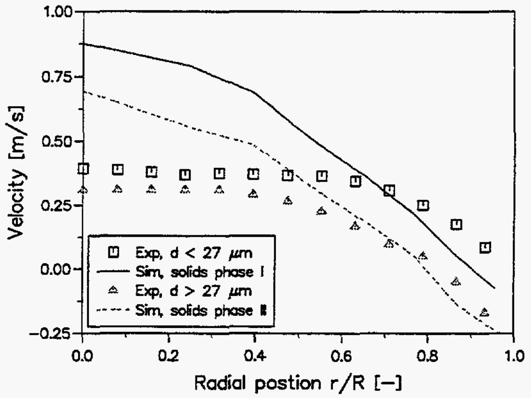

Figure 7.14: Particle velocity profiles, V_{SUP}=0.7 m/s, 0.4 kg solids.

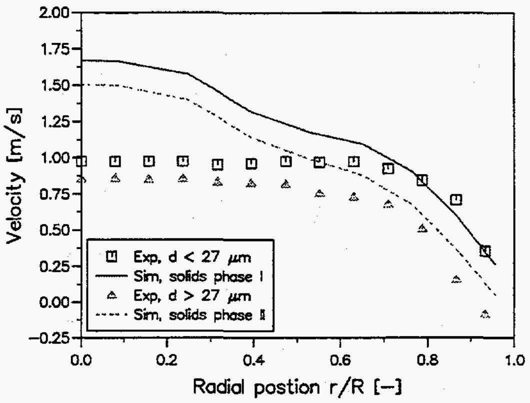

Figure 7.15: Particle velocity profiles, V_{SUP}=1.4 m/s, 0.4 kg solids.

The large discrepancies in the velocity profiles may be explained by the differences in actual and simulated geometry. Two basic simplifications of the geometry are done in the simulations. Only the riser part of the circulating fluidized bed is considered, and the riser is assumed two-dimensional.

The assumption that only the riser part of the circulating fluidized bed is considered in the simulations will have influences on the solids concentration in the riser and more important, the inlet and outlet flow conditions. In the simulations, the inlet is assumed to be an one-dimensional plug flow for the gas phase as well as the solids phases. The actual inlet and outlet conditions are non-uniform and formed as an elbow and will probably cause a non-symmetric flow behavior in the riser. A sketch of the riser with expected velocity vectors is given in *figure 7.16*. Remember that the LDA measurements are performed from the centerline to the wall perpendicular to the plane shown in *figure 7.16*, and therefore not able to capture any non-uniform flow behavior in this direction. These effects will further generate strong three-dimensional effects. A three-dimensional curve-linear or multiblock approach is preferable to describe geometries like this.

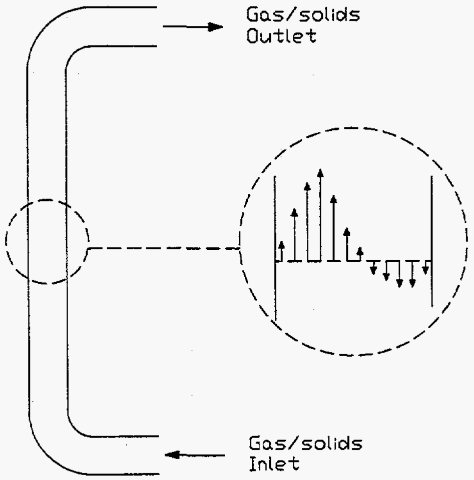

Figure 7.16: Sketch of geometry with expected velocity vectors.

The uncertainty in the determination of the mean diameter of the particle size distribution may also be a reason for the deviations between measurements and simulations. In gas/solids flow systems, small errors in the mean diameter may give rise to significant errors in the drag term. To demonstrate this, a closer discussion of the drag term is discussed next.

Solids with small and/or low density, classified as Group A and C according to Geldart classification of particles will normally follow the gas phase effectively. Thus there will be a very low relative velocity between the gas and the solids phases and further a very low Reynolds number. The drag coefficient is very sensitive in this range and increases exponentially with the inverse of the Reynolds number. The three most commonly used drag coefficients in gas/solids modelling are examined. The dimensionless drag coefficients are all related to the drag by the following equation, Wan and Yu (1966):

$$\Phi_{sg} = C_d \frac{3}{4} \frac{\alpha_s \alpha_g \rho_g |\vec{u}_g - \vec{u}_s|}{\psi_s d_s} \qquad (7.3)$$

The drag coefficient used in this work are based on Rowe (1961):

$$C_d = \frac{24}{Re}(1 + 0.15 Re^{0.687}) \alpha_g^{-2.65} \qquad (7.4)$$

whereas Gibilaro et al. (1985) proposed:

$$C_d = (\frac{17.3}{Re} + 0.336) \alpha_g^{-2.80} \qquad (7.5)$$

Syamlal and O'Brien (1987) derived a drag coefficient based on Dalla Valle (1948), and Garside and Al-Dibouni (1977):

$$C_d = \left(\frac{0.63 + 4.8\sqrt{u_{rs}/Re}}{u_{rs}} \right)^2$$

$$u_{rs} = \frac{1}{2}\left(A - 0.06Re + \sqrt{(0.06Re)^2 + 0.12Re(2B-A) + A^2} \right) \qquad (7.6)$$

$$A = \alpha_g^{4.14}$$

$$B = 0.8\alpha_g^{1.28} \qquad if\ \alpha_g \leq 0.85$$

$$B = \alpha_g^{2.65} \qquad if\ \alpha_g > 0.85$$

For a constant gas volume fraction of 0.99 the three drag coefficients are plotted in *figure 7.17* for Reynolds number ranging between 0 and 10.

The drag coefficients proposed by Rowe (1961) and Syamlal and O'Brien (1987) are almost identical, whereas the model by Gibilaro et al. (1985) has a somewhat lower value. More interesting than the small differences in the drag coefficients, is to study the exponentially increases of the drag coefficient at low Reynolds number.

In the simulations considered in this chapter, the relative velocity between the gas phase and solids phase I ($d = 40\ \mu m$) is typically 0.05 m/s. Thus a Reynolds number of 0.13 and a dimensionless drag coefficient of 197. In this area, the drag coefficient is very sensitive and a small decrease of the Reynolds number will give rise to a significant increase of the drag coefficient. With a particle diameter of 25 μm, the relative velocity, Reynolds number and drag coefficient are found to be 0.02 m/s, 0.03 and 833 respectively. Hence, by decreasing the diameter with 37.5 %, the drag coefficient increases with over 320 %. A further reduction of the diameter will lead to even more drastically increases of the drag coefficient.

It is also easy to show that the total drag coefficient Φ_{sg} is inversely proportional to the diameter squared, when the gas/solids flow is very dilute and for low Reynolds numbers.

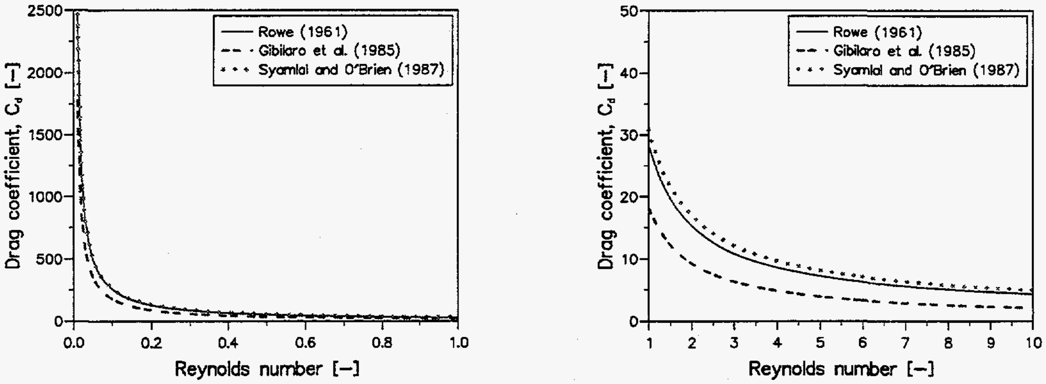

Figure 7.17 Drag coefficients for different Reynolds numbers.

This short discussion of the drag coefficient shows that more important than the choice of drag model are the specification of a correct mean diameter. It is very important to be aware that a too low specified diameter may give rise to a significant too large drag term and that this may totally control the gas/solids flow behavior. As discussed previously, the definition of the diameter of non-spherical particles are by no means a simple task. In the most commonly used particle size analyzers which are based on light intensity from a laser source, the techniques to convert the light intensities to particle size distribution are normally secret information. The manufacturers also use different techniques which give different results.

7.3.4 RMS Velocity Profiles

Figure 7.18, 7.19, 7.20 and *7.21* show the particle RMS velocity profiles for each particle group as well as the computed RMS velocities. The computed RMS velocities include contributions from both the small and large scale fluctuations.

For a very dilute gas/solids flow system that are considered in these experiments, the particle collisions are of less importance. Therefore the fluctuating velocity or the turbulence is mainly produced by the shear and particle collisions with the wall. The RMS velocity in such a case increases from center of the riser toward the wall.

The experimental results show that the particles RMS velocity is in the same order of magnitude for all flow conditions. However, in the wall region the turbulence is increasing when the superficial gas velocity increases, due to higher velocity gradients.

Overall the experimental results show that the RMS velocity is highest for the particles of largest size in a very dilute (e.g. 1-3 %) gas/solids flow system. The experimental data does not support the behavior reported in the literature, where large particles normally are assumed to have a less fluctuating behavior.

The gas turbulence will normally be less than the solids turbulence. Smaller particles will follow more easily the gas flow than larger particles. This may explain why in a flow system with very little particle collisions (e.g. dilute system) and relative small and light solids, larger particles show more fluctuating behavior than smaller particles.

The computed turbulent velocity have the same form and tendency as the experimental data. A relative RMS velocity between different sizes are obtained and the largest particles have correctly the largest RMS velocity. The computed turbulence also show the correct increase in the shear layer near the wall.

However, the fluctuating velocity has a too low value in all simulations. In the turbulent kinetic energy equation a dissipation term due to interaction between gas and solids phases are included, whereas the corresponding production term is neglected. Ding and Gidaspow (1990) assumed that the correlation between the gas phase fluctuation velocity and the solids phase fluctuation velocity is negligible and hence the production term. They pointed out that such an assumption is valid when the particle response time is much larger than the time scale characteristic of the mean fluid motion. This means that the assumption is valid when the particle are large and heavy. There may be reasons to believe that this term should be included, specially when dealing with relatively small and light particles, such as FCC catalysts. It should be noted that to include the production term is rather complicated and may require a turbulence model for the gas phase in the presence of the solids phase.

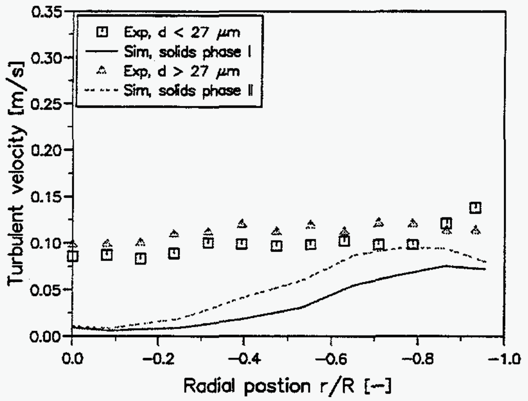

Figure 7.18: RMS velocity profiles, V_{SUP}=0.7 m/s, 0.1 kg solids.

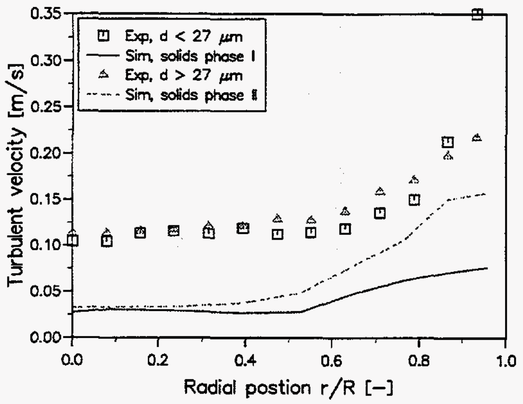

Figure 7.19: RMS velocity profiles, V_{SUP}=1.4, 0.1 kg of solids.

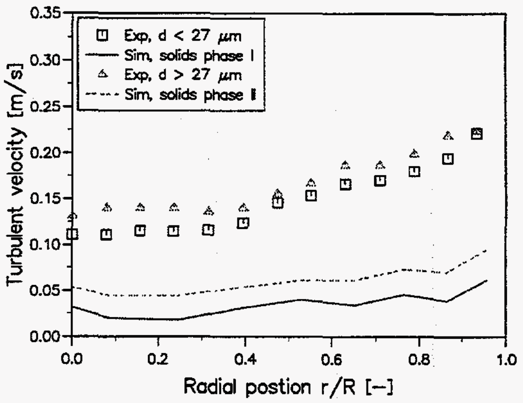

Figure 7.20: RMS velocity profiles, V_{SUP}=0.7 m/s, 0.4 kg solids.

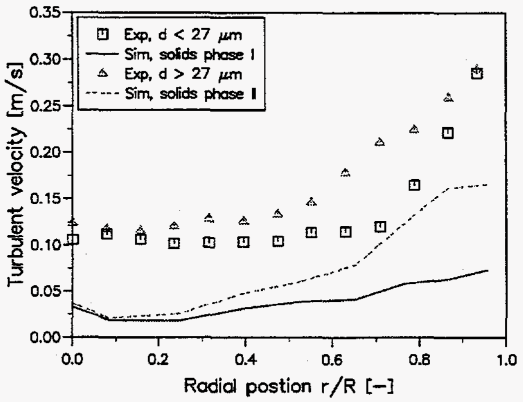

Figure 7.21: RMS velocity profiles, V_{SUP}=1.4 m/s, 0.4 kg solids.

7.4 Summary

An experimental study of the flow behavior of group A particles in the riser section of a laboratory scale circulating fluidized bed using LDA is successfully conducted. Particle diameter as well as mean and fluctuating velocity for different particle sizes are measured for different flow conditions. The experimental results are discussed and analyzed, and may be summarized as follows:

- There are no significant agglomeration in the gas/solids flow system.
- A annulus-core flow behavior is observed.
- A relative velocity between particles of different sizes is measured. This relative velocity remains almost constant across the radius.
- A relative fluctuating velocity between different sizes is observed as well, where the largest particles have the highest turbulent velocity. This behavior is explained by significant gas/solids interactions.
- A significant radial segregation of the mean diameter is observed. The mean diameter increases from the center of the riser toward the wall.

A computational study of the riser section of the circulating fluidized bed is performed. Relatively large discrepancies from the experimental data are observed. However the model are able to calculate core-annulus flow with a correct relative velocity between the solids phases. The discrepancies between simulations and experimental results may be explained by the differences in actual and simulated geometry. Whereas the simulations are performed with a two-dimensional Cartesian description, the actual geometry will produce strong three-dimensional effects. It is also pointed out the importance of using a correct particle diameter and that small deviation from this may give rise to significant error in the drag coefficient and further the velocity profiles.

The computed mean diameters have a constant value across the riser and shows that the model are not able to calculate the radial segregation of the mean diameter.

The computed turbulent velocity is too low according to experimental data, but has the same form and tendency. The model calculate correctly the highest turbulence level for the largest particles. This is the opposite behavior observed in chapter 5 where the smallest particles had the highest turbulence level, in the measurements as well as in the computational results. This shows that the turbulence levels for small/large particles are a function of the particle diameter and density. In a dilute gas/solids flow system, the smallest particles will have the smallest turbulence level when dealing with relatively small and light particles (group A), but have the highest turbulence level when the mean diameter and density are large (group B).

CHAPTER 8

3D MODELLING OF A PILOT SCALE RISER

In chapter 6 a pilot scale circulating fluidized bed was modelled and simulated using a two-dimensional Cartesian coordinate system. In this chapter the riser section of the same cold flow pilot scale circulating fluidized bed is computed in three dimensions. This is done to capture three-dimensional effects in order to obtain more detailed information of the processes involved. A simulation with three solids phases is conducted. A qualitative analyses of the computational results is performed, where a discussion of three-dimensional and transient effects are emphasized. No comparison against experimental data are done, but two and three dimensional results are compared.

8.1 Numerical Flow Parameters, Initial and Boundary Conditions

The numerical flow parameters, initial and boundary conditions are corresponding to those in chapter 6. Three solids phases are used to describe the real particle size distribution, which have a mean particle diameter and a standard deviation of the particle size distribution of 120 and 18 μm respectively. 12.5 volume percent of the particles have a diameter of 84 μm, 75 volume percent have the mean diameter of 120 μm and the last 12.5 volume percent are assumed to have a diameter of 156 μm.

Since the actual riser section of the circulating fluidized bed is rectangular, a three-dimensional Cartesian geometry approach should give a favorable description of the riser. A sketch of the calculation domain with grid nodes is shown in *figure 8.2*. As the figure shows, the grid is uniform in axial direction, whereas a non-uniform grid is adopted in both radial directions. To cover the calculation domain, $26\times26\times52$ grid points are used.

Uniform one-dimensional plug flow for the gas is assumed at the inlet. The inlet flux of the solids phases are assumed to be equal to the outlet flux of each phase. At the outlet which are located at the top of the riser, all the dependant variables of the solids phases are extrapolated downstream. To ensure that the overall continuity condition is satisfied, the gas phase velocities are calculated from a total mass balance at the outlet. As in chapter 6, a no-slip condition is used for the gas phase as well as the solids phases.

The simulation are performed with a superficial gas velocity of 0.9 m/s and a solids volume concentration of 3 %. The simulation have been run for only ten seconds, since the simulation requires very large computer resources. The time averaged results are obtained from the two last seconds.

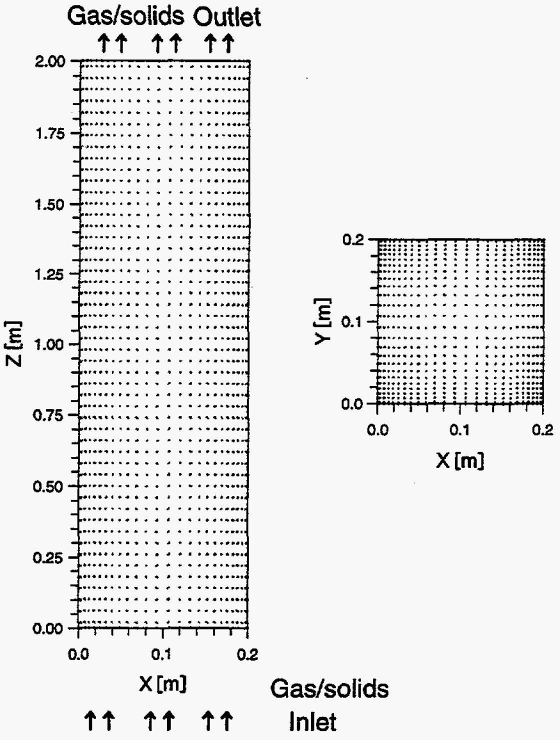

Figure 8.1: A sketch of calculation domain with grid nodes.

8.2 Numerical Results

8.2.1 Volume Fraction

In *figure 8.2*, the time averaged solids volume fraction for the three solids phases is presented. The volume fractions are plotted at height 0.3, 1.0 and 1.6 m above the gas/solids inlet respectively. Solids phase I has the smallest diameter (84 μm), solids phase II has the intermediate diameter (120 μm) whereas the solids phase III has the largest size (156 μm).

The figure evidently shows that the total concentration of solids decreases with the height above inlet. It is clearly observed that particles of larger size have a more non-uniform concentration distribution in axial direction than smaller solids. The smallest solids fluidize easily and follow the gas effectively, and the concentration of this group decreases slightly from the bottom of the riser toward the top. For the intermediate particles more evident segregation occur, whereas almost all the largest particles are located in the dense turbulent bubbling bed zone.

The small and the intermediate particles have a radial volume fraction distribution which are very similar. At the locations where the concentration of the smallest particles increases or decreases, the intermediate particles seem to have the same behavior. The largest particles does not follow the same clear trend, and the concentration distribution of solids phase III seems to be nearly independent of solids phase I and II.

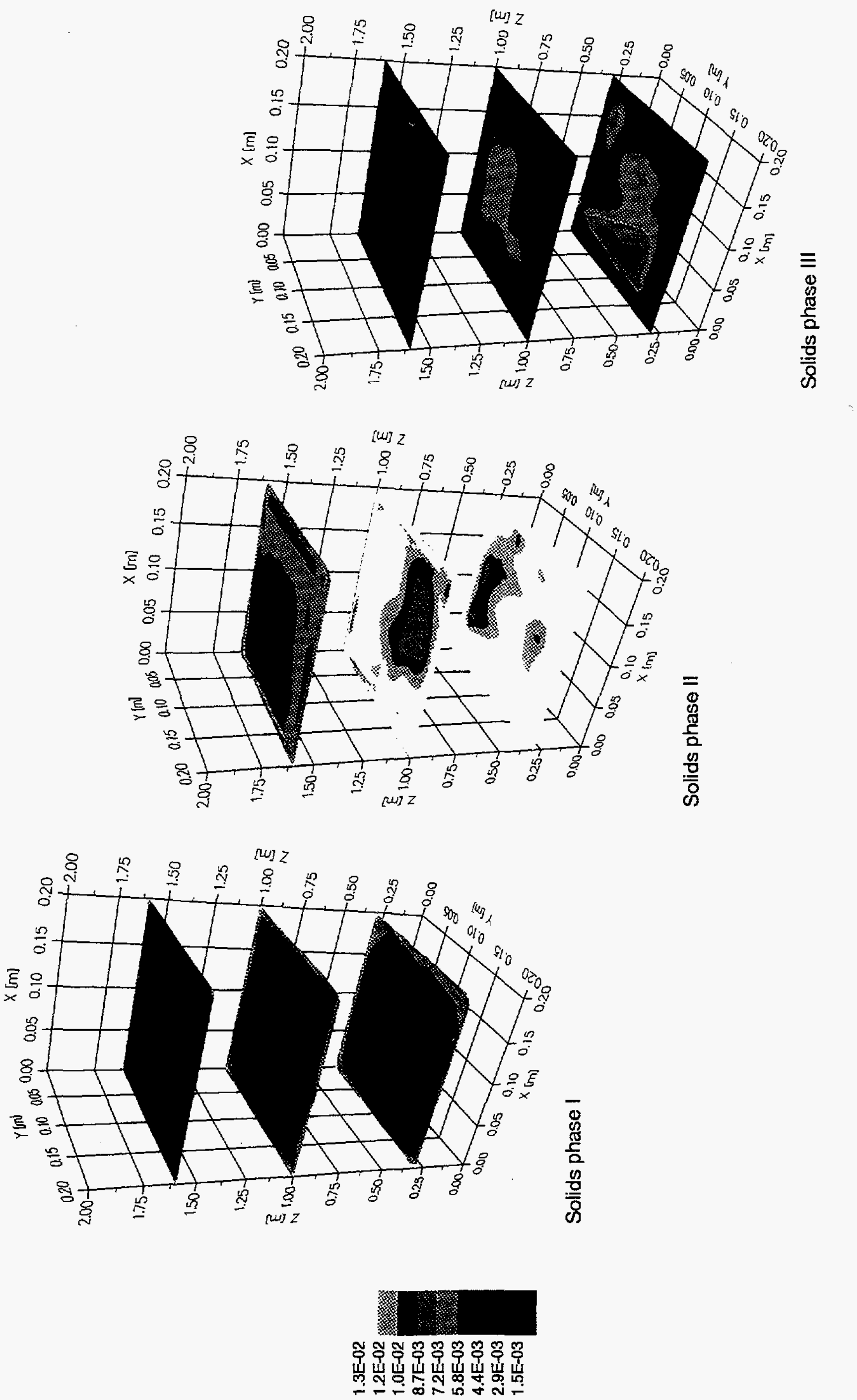

Figure 8.2: Time averaged volume fraction for the three solids phases.

At all heights the concentration of solids is most dense in the wall regions, particular for the smallest and intermediate particles. Hence, the mean diameter is somewhat smaller in the wall region than in the more dilute core region. This indicates that the significant increase of the mean diameter in the wall region which was observed experimentally in chapter 5 and 7, is not caused by three-dimensional effects.

For the smallest and intermediate particles the concentration of solids increases slightly in the corners as well. That the solids concentration increases more in the corners than along the wall generally is expected, and caused by stronger wall effects in this region.

The fluctuating behavior of the gas volume fraction is shown in *figure 8.3*. The gas volume fraction is monitored at the median axis, 1.0 m above the inlet. The figure shows that the gas fraction in the riser never reach a normal steady state condition, but exhibits a fluctuating behavior. At this position, which seems to be located in the top of the dense turbulent bubbling bed zone, the solids concentration is varying between 2 and 4 %. The figure shows that the riser need around 6 seconds to reach the normal flow condition.

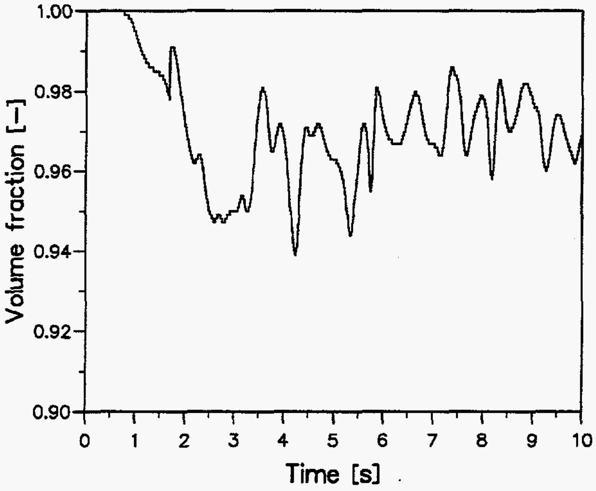

Figure 8.3: Time evolution of gas volume fraction, X=0.1 m, Y=0.1 m, Z=1.0 m.

In *figure 8.4*, a short time series of the total volume fraction of solids is presented. The horizontal as well as the vertical plot are made after 6.0, 8.0 and 10.0 seconds real time. The horizontal planes are plotted 0.3, 1.0 and 1.6 m above the inlet, and the vertical plot for Y=0.1 m. The volume fraction distribution is chaotic and random at all heights, but most clear in the dense turbulent bed. The dense region seems to be somewhat higher than 1.0 m.

The random concentration gradient observed in the horizontal planes are isotropic and have no preferred direction. However, a more dense region near the wall is clearly observed.

There are relatively large concentration gradient which are related to the bubble formation in the riser. Inside the bubbles there are relative low fraction of solids, whereas the solids concentration is very high in the emulsion phase. There exist also considerable flow of the gas as a combination of bubble and emulsion phase. Small bubbles are formed in the corners as well as in the rest of the cross-section area, particular at the lowest height.

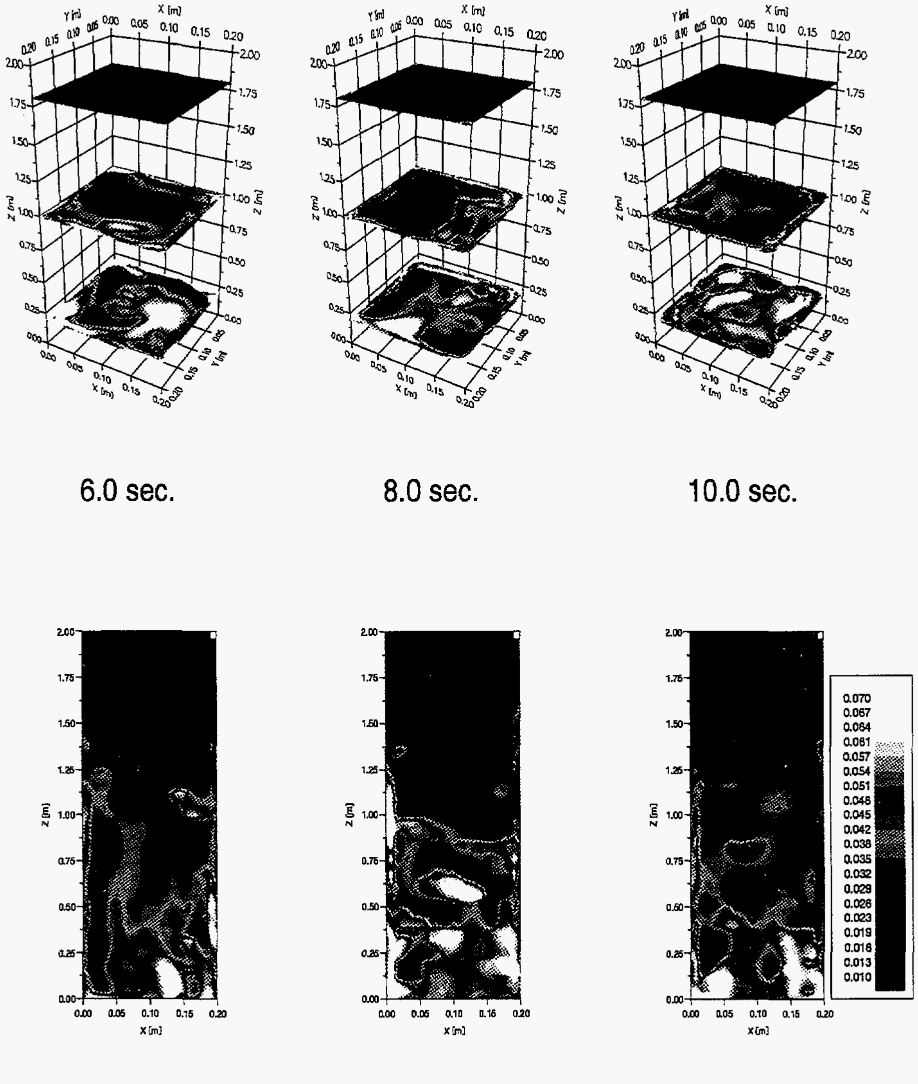

Figure 8.4: Time series of total solids volume fraction.

8.2.2 Particle Velocity

Time averaged axial velocity contours for the three solids phases are plotted in *figure 8.5*. The figure shows very clearly the multiphase flow behavior that will occur in a gas/solids system with a multisize particle size distribution. A typical core-annulus flow is observed for all solids phases, which means a nearly constant upflow of particles in the core and negative velocities in the wall regions.

The smallest particles have a significant higher particle velocity in the core region than the intermediate and larger particles. The particle velocity decreases with increasing particle diameter, due to a reduced gas-particle drag.

For all solids phases the velocity contours become flatter when the height above the inlet increases. In some cases the maximum velocity deviates from the center of the riser.

The particle velocity plot show that the flow behavior of particles with unequal diameter is very similar. At locations where the particle velocity increases/decreases for one solids phase, similar changes are observed for the two other particle phases as well.

The figure shows very clearly that the width of the annulus regions are significantly different for various particle diameters. The smallest particles have a relative narrow annulus and a wide core region, whereas the intermediate and large particles have a considerable larger annulus zone. Three-dimensional effects are easily observed in the corners, where the annulus region are significantly wider than along the wall.

In *figure 8.6* the velocities are shown after 6, 8 and 10 seconds for the three solids phases. The color contours show the axial velocity, whereas the vectors show the radial velocities. The largest vectors have a radial velocity of about 0.2 m/s. The axial velocity shows relatively large deviation from the time averaged values in *figure 8.7*. Also for the snapshots, the relative velocity between different solids phases are almost constant.

The axial and the radial velocity show a random and chaotic flow behavior. The axial velocity are significant and hence a relatively large axial mixing of solids. There are no significant differences in the order of magnitude of the axial velocity at different heights. The velocities have the same chaotic flow in the upper part of the riser as in the dense turbulent bed region.

The velocity vectors for Y=0.1 m are plotted in *figure 8.7* at the same time and for each solids phase. The figure confirms a stochastic flow behavior in the riser. However, the particles velocity is almost always negative close to the wall. In the central part of the riser, the oscillating velocity includes negative and positive values, but a much higher fraction of the particles are flowing upward than downward. The radial velocities are relative small, compared to the axial velocities.

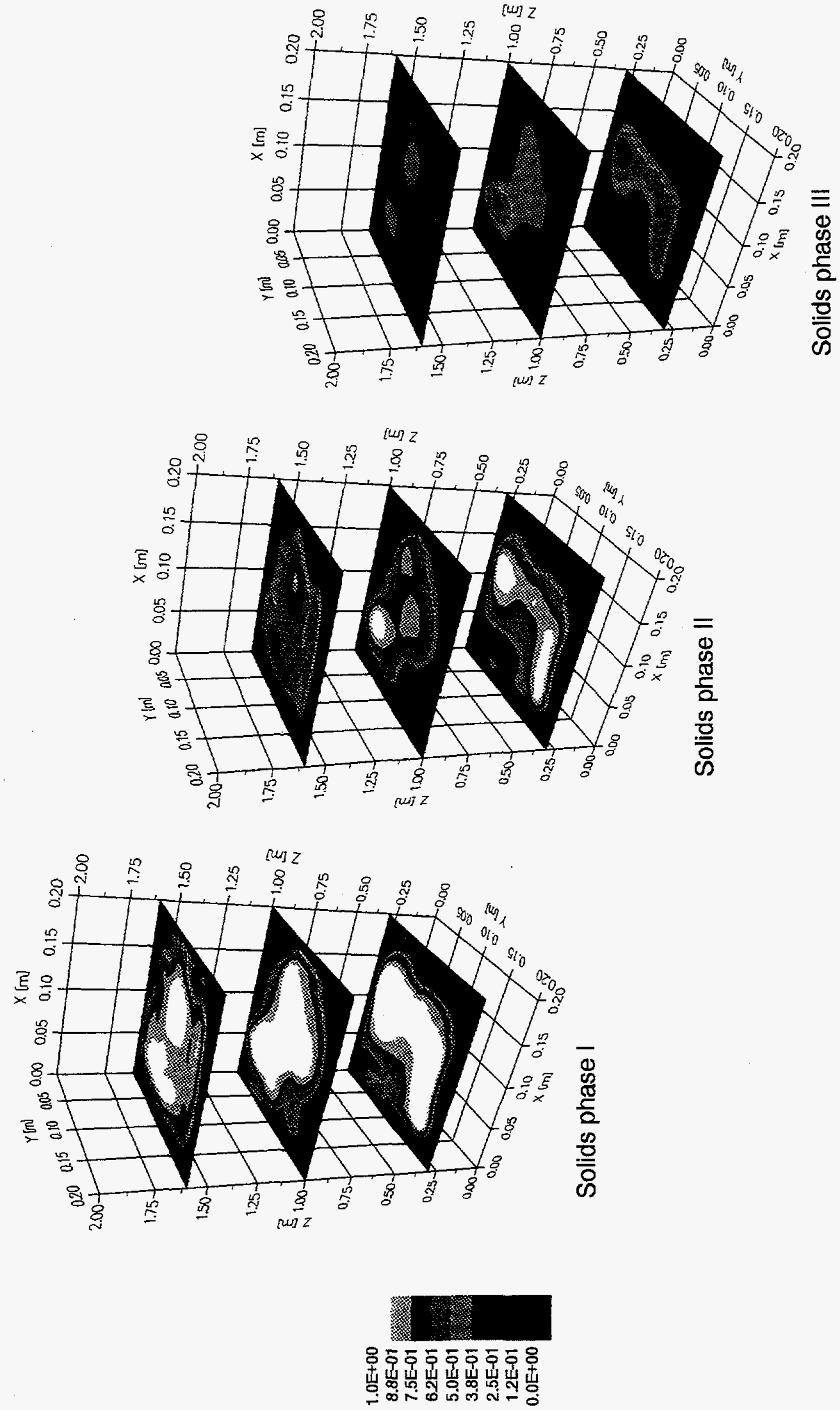

Figure 8.5: Time averaged particle velocity for different solids phases.

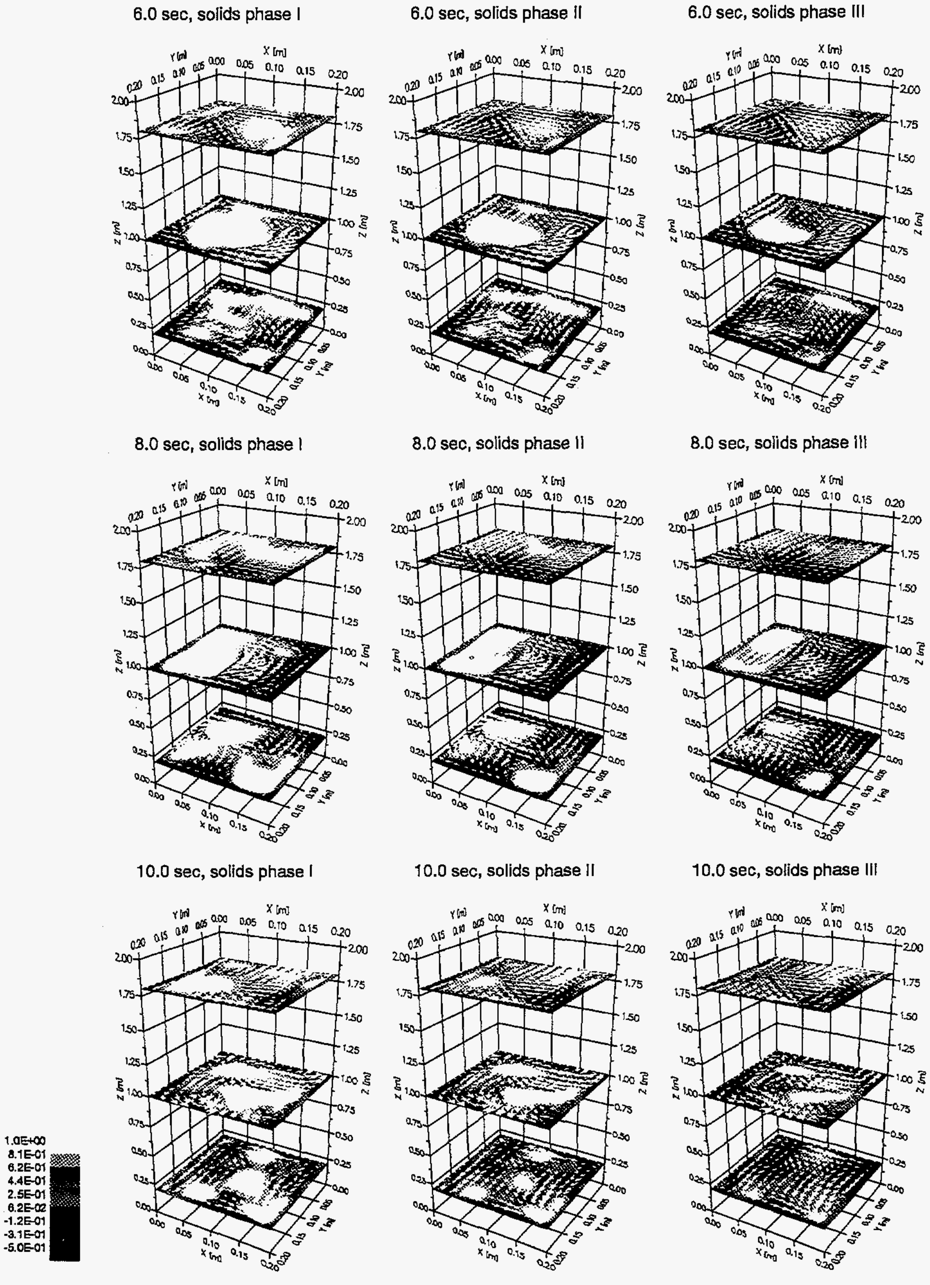

6.0 sec, solids phase I

6.0 sec, solids phase II

6.0 sec, solids phase III

8.0 sec, solids phase I

8.0 sec, solids phase II

8.0 sec, solids phase III

10.0 sec, solids phase I

10.0 sec, solids phase II

10.0 sec, solids phase III

Figure 8.6: Time series of particle velocities.

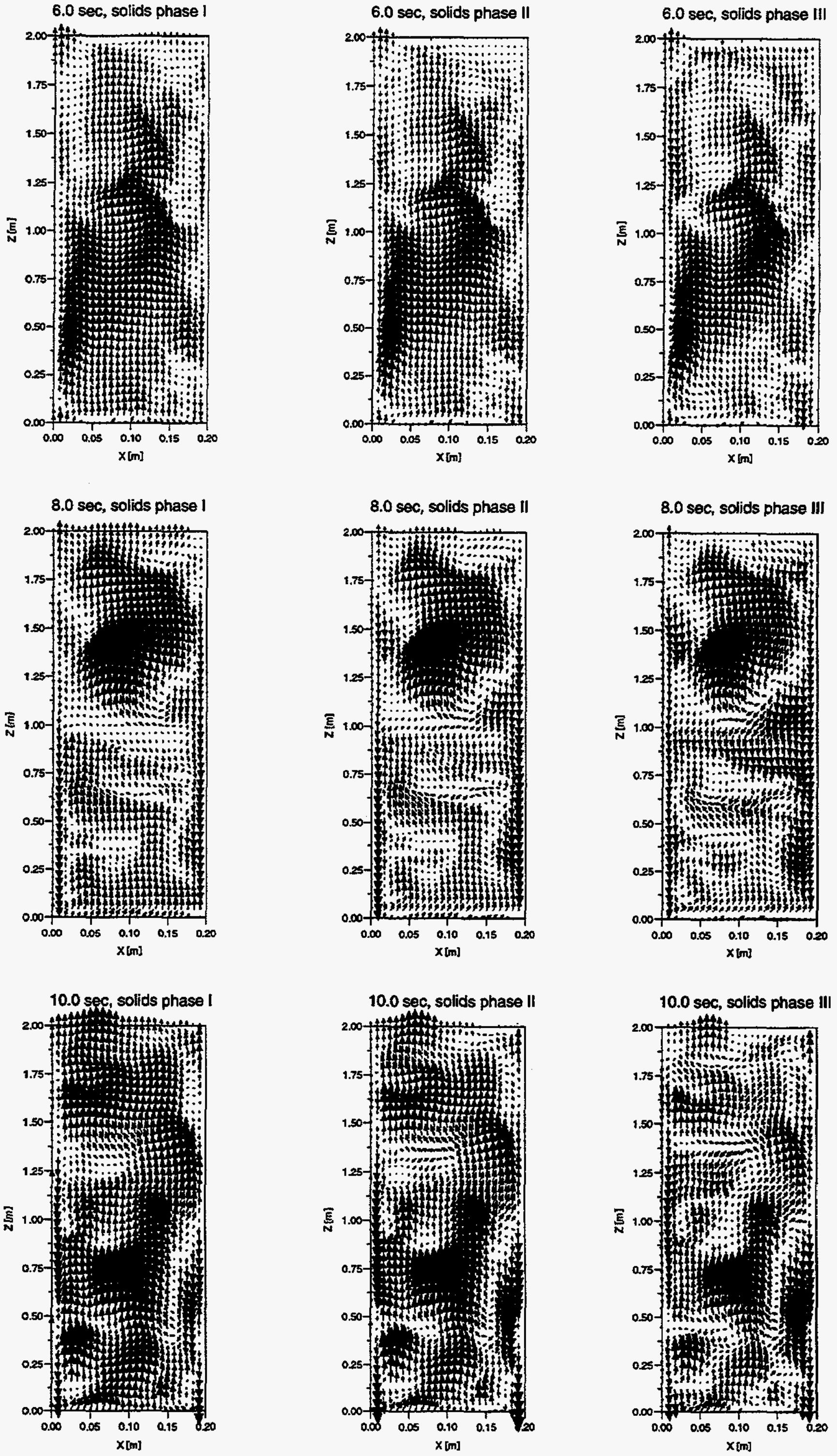

Figure 8.7: Short time series of velocity vectors.

8.2.3 Particle RMS Velocity

The time averaged turbulent velocity for each solids phase is shown in *figure 8.8*. The turbulent velocity is derived from the granular temperature and does not include contribution from the large scale fluctuations.

For a dilute gas/solids flow system that is considered in this simulation, the gas-particle interaction are of greater importance than the particle collisions. Hence the turbulence is mainly produced by the shear. The turbulence in such a case is almost constant in the central part of the riser and increases in the wall region. This behavior is clearly observed in *figure 8.8*.

Generally the turbulence increases slightly more in the corners than along the wall. This is caused by the larger velocity gradients in these regions. Other significant three-dimensional effects are not observed.

An interesting observation as well, is that the largest particles have a considerable higher turbulent velocity than the small and intermediate particles. This behavior was found experimentally and numerically for relative small and light FCC catalysts in chapter 7. The phenomena was explained by that the gas turbulence will normally be lower than the particle turbulence, and that smaller particles will follow the gas flow more easily than larger particles. Whether this theory are valid for larger and heavier solids such as glass spheres or not, can only be determined by experimental investigations.

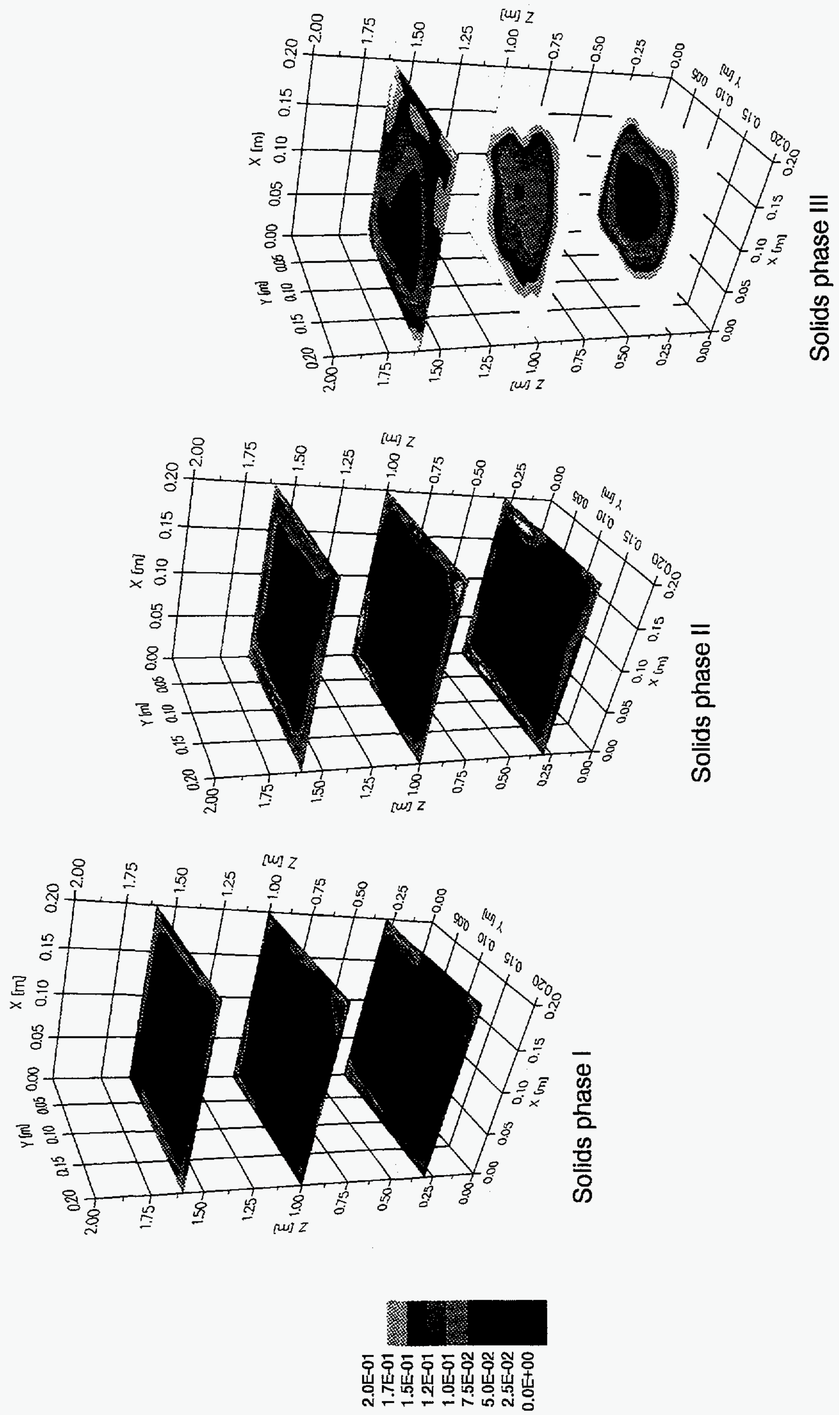

Figure 8.8: Time averaged turbulent velocity for different solids phases.

8.2.4 Comparison of 2D and 3D

The riser section of the circulating fluidized bed is also computed with a two-dimensional Cartesian geometry description. The numerical flow parameters, initial and boundary conditions are held constant and are the same as for the three-dimensional approach.

The time-averaged solids volume fraction profiles for two and three-dimensional approaches are compared in *figure 8.9*. The profiles are made 1.0 m above the inlet and for Y=0.1 m for the three-dimensional situation. Although some deviations are observed, the particle concentration profiles have the same form and order of magnitude. The time averaged results are unsymmetrical and this may indicate that the time averaged results should have been obtained over a longer time interval.

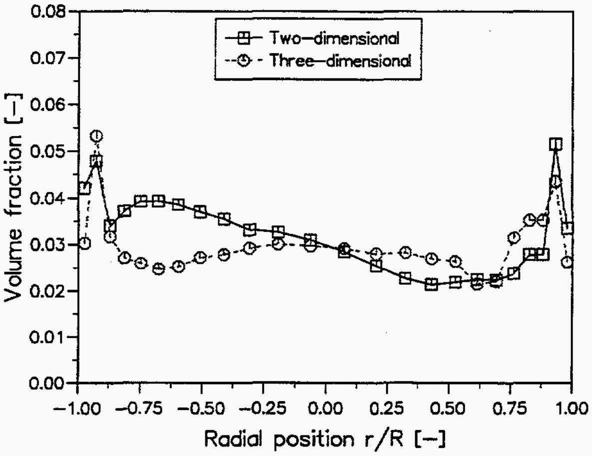

Figure 8.9: Solids volume fraction profiles for 2D and 3D situations.

In *figure 8.10* the number averaged particle velocity profiles are shown at the same position. Both for the two and three-dimensional situation a typical core-annulus flow is observed. The particle velocity profiles are in the same order of magnitude, but for the three-dimensional simulation a more smooth profile and a somewhat higher particle velocity are observed.

Figure 8.11 shows the particle RMS velocity profile for the two and three-dimensional approaches. The profiles are obtained from an averaged granular temperature and not included large scale fluctuations. The figure shows that the turbulence are almost the same in the core region, whereas some discrepancies are observed in the wall region.

Altogether, *figure 8.9*, *8.10* and *8.11* show relative small differences for the two and three-dimensional simulations, and the form and order of magnitude of the results are the same.

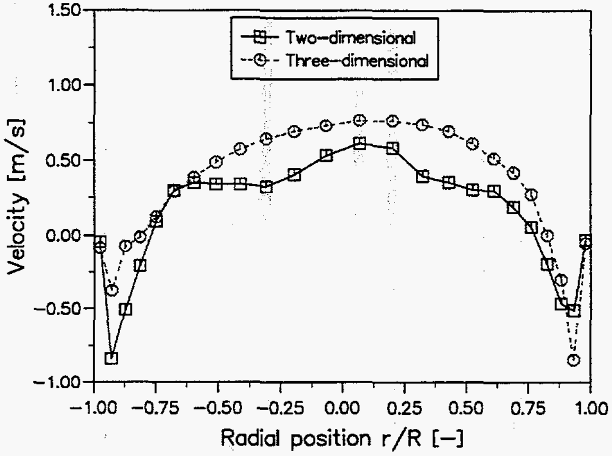

Figure 8.10: Particle velocity profiles for 2D and 3D situations.

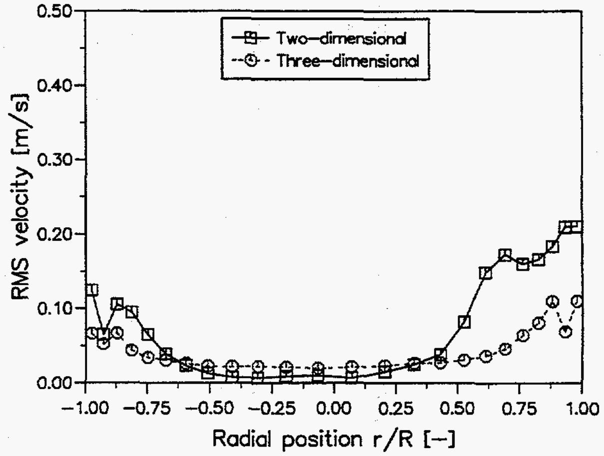

Figure 8.11: Particle RMS velocity profiles for 2D and 3D situations.

8.3 Summary

A three-dimensional simulation of the riser section of a pilot scale circulating fluidized bed is performed. Three-dimensional plots of time averaged variables and short time series of them are presented. The results show that the mathematical model is able to calculate reasonable flow pattern in three-dimensional geometries with one gas and three solids phases.

The results show a significant higher concentration of solids in the wall region than in the center of the riser. Generally the solids concentration is slightly higher in the corners than along the wall.

A typical core-annulus flow is observed for all three solids phases. The annulus region is wider for larger solids than for smaller ones. The width of the annulus increases in the corners due to the wall effects.

Short time series of the solids volume fraction and velocity components show a random and stochastic gas/solids flow behavior in the riser.

The turbulent velocity is highest for the largest particles. For all solids phases the turbulence is almost constant in the center of the riser, but increases considerably in the wall region and particular in the corners.

Altogether the flow pattern in this riser show relative small three-dimensional effects. The obtained results show that when considering geometries like this, a two-dimensional assumption is reasonable and will not cause too large discrepancies.

CHAPTER 9

CONCLUSIONS AND RECOMMENDATIONS

The main objective of this work has been to provide a better understanding of the complex flow behavior in gas/solids circulating fluidized beds. Both experimental and computational studies of different circulating fluidized bed systems are conducted. Great importance are given to investigate different particle diameters and particle size distributions influences of the gas/solids flow behavior. The conclusion of this work and obtained results, and recommendations for further work are following next.

9.1 Conclusions

Based on earlier works at Telemark Institute of Technology, a three-dimensional Computational Fluid Dynamics (CFD) model for turbulent gas/solids flow is developed and presented. The model uses an Eulerian description of the phases and the conservation equations for the solids phases are based on kinetic theory for granular flow with basis on the work of Jenkins and Savage (1983), Lun et al. (1984), Ding and Gidaspow (1990), Gidaspow (1994) and further extended to binary mixtures by Manger (1996). The model is generalized for one gas phase and N number of solids phase to enable description of realistic particle size distributions. Each solids phase is characterized by a diameter, form factor, density and restitution coefficient. The granular temperature and momentum equations are solved for each phase.

An experimental study has been performed on two different circulating fluidized bed systems. In both cases, LDA is used to measure mean and fluctuating velocity for different particle sizes. A LDA technique is also used to estimate the particle size of non-spherical FCC catalysts, whereas PDA is used to measure diameter and volume fraction of dispersed spherical glass particles.

An extensive experimental study of the flow behavior of group B particles in a cold flow laboratory scale circulating fluidized bed is performed in chapter 5. Mean and RMS particle velocities are obtained for two distinct different particle sizes. In addition, solids volume fraction and mean diameter are estimated. The experimental results are analyzed and may be summarized as follow:

- A typical core-annulus flow behavior is observed in the riser.
- A relative particle velocity between small and larger particles is measured. The relative velocity is largest in the center of the riser and decreases toward the walls.
- The turbulent velocity is almost constant in the central part of the riser and increases in the shear layer.
- A relative particle RMS velocity is observed in the lower part of the riser. Smaller particles fluctuate more than larger ones. In the upper part of the riser, the turbulent velocity seems to be nearly independent of the particle diameter.
- The solids concentration are dilute in the core region and denser in the annulus zone.
- An axial segregation by size is shown. The axial segregation decreases when the superficial gas velocity increases.

- A significant radial segregation of the mean diameter is shown, a behavior which seems not to be observed or reported in earlier studies of gas/solids flow. The mean diameter is almost constant in the center of the riser and increases drastically toward the walls. The radial diameter distribution is most uniform in the most dense region.

The same circulating fluidized bed loop is simulated using a two-dimensional Cartesian coordinate system. Two solids phases are used to describe the two distinct particle groups. The simulations are in a fairly good agreement with the measurements. The core-annulus flow is correctly computed and the solids concentration seems to be relative well predicted. However the relative velocity between the solids phases is somewhat overpredicted. This may be due to the underestimated turbulent kinetic energy in the lower part of the riser, since the particle-particle drag is proportional to the square root of the granular temperature. In the upper part of the riser, the computed turbulence has a correct form and magnitude, although the turbulence in the shear layer is somewhat too low.

For different superficial gas velocities the mathematical model is capable of estimating the axial segregation by size very well. But the model is not able to predict the significant radial variation of the mean diameter. The underestimation of the turbulence in the lower part may be a reason for the deviation between measured and simulated mean diameter in the wall region. The radial segregation may also be a result of external forces which are not included into the mathematical model.

The large scale fluctuations which occur in a gas/solids flow system are calculated and added to the small scale fluctuations predicted by the granular temperature. Although the large scale fluctuations seemed significant, they increased the total particle RMS velocity slightly in this case. The model calculate correctly highest turbulence for the largest particles.

A closer investigation of wall effects is done. The wall effects change the particle velocities in the annulus region significantly, but did not change the flow behavior, segregation by size or had other considerable effects on the flow pattern.

It is shown that the magnitude of the restitution coefficient is not important in a dilute gas/solids system. In a very dilute gas/solids flow system that is considered in these simulations, dissipation is mainly caused by interactions with the gas and not by particle-particle collisions.

In chapter 6, two-dimensional simulations of a pilot scale circulating fluidized bed are performed. The computational results are compared against experimental results reported in the literature. The simulations are performed with different superficial gas velocities, initial solids concentrations and standard deviations of the particle size distribution. Most emphasis is given to study the effects of different particle size distributions and to study the fluctuating behavior of the dilute gas/solids flow system. Altogether the simulation results are in very good agreement with experimental data.

It is shown that the CFD model is able to capture the large scale fluctuations which will evidently be present in a circulating fluidized bed system. The large scale fluctuations of mean velocities, volume fractions and mean diameter are monitored and compared against experimental results. Both the frequency of the fluctuations and the size of the oscillations are in the correct order of magnitude.

Axial and radial large scale fluctuations are calculated and added to the small scale turbulence from the isotropic granular temperature. The computed small scale turbulence are significantly too small according to the experimental data. By adding the large scale fluctuations a correct order of magnitude is obtained, although some deviations are still observed. The calculations confirm that the axial fluctuations are much larger than the radial fluctuations and hence the fluctuating behavior of the circulating fluidized bed is evidently not isotropic.

Simulations are performed with two different particle size distributions and compared against experimental data along the median axis of the riser. The computed mean diameters are in good agreement with the experimental data both in form and magnitude. For the narrow size distribution, the particle diameter is almost constant along the median axis, whereas for the wide-ranging size distribution a significant segregation by size is correctly obtained.

The axial velocity along the median axes are calculated for the two different particle size distributions as well. The simulations show the same tendency as the experiments, although some discrepancies are observed. A higher velocity is correctly obtained for the large particle size distribution.

Mean particle velocity profiles are obtained at three different heights with only insignificant deviations from the measurements. A typical core-annulus flow is calculated with a nearly constant velocity in the central part of the riser and a down flow of particles in the wall region. As in the experimental data, the velocity profiles became flatter when the height above the inlet increases.

A mean radial velocity is calculated. The agreement with experimental velocity is very good and the results show that the radial velocity is approximately zero at the centerline, then increases toward the shear layer and further decreases to the wall.

Net mass flux profiles are computed and presented. The calculated flux profiles show a fairly good agreement with the experimental data. Best agreement is obtained in the upper part of the riser and the total flux circulating in the loop seems to be reasonably predicted. At lower heights, larger deviations are obtained. The CFD model compute a little too high flux upward in the core region, whereas a little too high negative net flux is computed in the annulus region. The results indicate that the model calculate a too large axial mixing of particles.

In chapter 7, an experimental study of the flow behavior of group A particles in the riser section of a laboratory scale circulating fluidized bed using LDA is successfully conducted. Particle diameter as well as mean and fluctuating velocity for different particle sizes are measured for different flow conditions. The experimental results are discussed and analyzed, and may be summarized as:

- No significant agglomeration in the gas/solids system is observed.
- A core-annulus flow behavior is observed.
- A relative velocity between particles of different sizes is obtained. This relative velocity remains almost constant across the radius.
- A relative fluctuating velocity between different sizes is observed as well, where the largest particles have the highest turbulent velocity. This behavior is explained by significant gas/solids interactions.
- A significant radial segregation of the mean diameter is observed. The mean diameter increases from the center of the riser toward the wall.

A computational study of the riser section of the circulating fluidized bed is performed. Relative large discrepancies from the experimental data are observed. However the model are able to calculate core-annulus flow with a correct relative velocity between the solids phases. The deviation between simulations and experimental results may be explained by the differences in actual and simulated geometry. Whereas the simulations are performed with a two-dimensional Cartesian description, the actual geometry will produce strong three-dimensional effects. It is also pointed out the importance of using a correct particle diameter and that small deviation from this may give rise to significant error in the drag coefficient and further the velocity profiles.

The computed mean diameters have a constant value across the riser and shows that the model are not able to calculate the radial diameter distribution.

The computed turbulent velocity is too low according to experimental data, but has the same form and tendency. The model calculate correctly highest turbulence for the largest particles.

In chapter 8 a three-dimensional simulation of the riser section of a pilot scale circulating fluidized bed are performed. Three-dimensional plot of time averaged variables and short time series of them are presented. The results show that the mathematical model is able to calculate reasonable flow pattern in three-dimensional geometries with one gas and three solids phases.

The results show a significant higher concentration of solids in the wall region than in the center of the riser. The solids concentration is slightly higher in the corners than along the wall generally.

A typical core-annulus flow is observed for all three solids phases. The annulus region is wider for larger solids than for smaller ones. The width of the annulus increases in the corners due to the wall effects.

Short time series of the solids volume fraction and velocity components show a random and stochastic gas/solids flow behavior in the riser.

The turbulent velocity is highest for the largest particles. For all solids phases the turbulence is almost constant in the center of the riser, but increases considerably in the wall region and particular in the corners.

The flow pattern in this riser shows relative small three-dimensional effects. The obtained results show that when considering geometries like this, a two-dimensional assumption is reasonable and will not cause too large discrepancies.

Altogether the computational results show a very good agreement with experimental data in situations where a two-dimensional Cartesian geometry description is reasonably. This indicates that the multiphase gas/solids model works fairly well. However, as in chapter 7 where complex geometries and large three-dimensional effects are considerable, larger discrepancies between experimental and computational results are observed. This indicates further that the geometry description seems to be the weakness of the developed CFD model.

9.2 Recommendations for Further Work

From the main conclusion, the recommendations for further work should be clearly:

- A better geometry description are evidently required. One possibility is body-fitted coordinate description, but this is probably not enough. Hence a multiblock approach may have to be incorporated, or unstructured grid systems should be considered.

Three-dimensional simulations require very large computer resources and when moving to more complex systems the computation time become a restriction, so:

- Better and more effective numerical solution algorithms and optimization toward parallel and/or vector configurations are necessary.

However, the multiphase gas/solids model are far from perfect and a lot of improvement may be done:

1.) The effects of particle-wall collisions may play a significant role at the flow behavior and should be more extensively studied.
2.) In the presented model, only an effective gas viscosity is computed based on a Sub Grid Scale model. A gas phase turbulence model which includes the turbulent gas-particle interactions should be considered. Hence a production term due to gas/particle interaction may be incorporated in the turbulent kinetic energy equations. This extension is most important when dealing with dilute gas/solids flow systems.
3.) To include a theoretical obtained and more correct radial distribution function are essential when considering dense gas/solids flow.
4.) In order to obtain sharp interfaces, higher order discretizations schemes should be incorporated in the model.
5.) The multiphase granular model which solves a granular temperature for each solids phase is based on the assumption that the mean velocity differences is relatively small. The binary kinetic theory should be developed without this restriction.
6.) Chemical reaction, heat and mass transfer should be included in the model to improve the application of the CFD code to chemical reactors.

Both to give a better understanding of the complex flow behavior in circulating fluidized bed and to get experimental data to verify the CFD model, more experimental work of circulating fluidized bed systems are obviously important.

The experimental study in this thesis is performed in a dilute laboratory or pilot scale gas/solids circulating fluidized bed with a relative low superficial gas velocity. To verify the dense part of the model, experimental data which includes information about diameter distributions in a bubbling bed are needed. Also experimental data in dilute gas/solids flow systems with higher superficial gas velocities are desirable, as well as experimental data from large scale reactors of industrial interests.

REFERENCES:

Ahmadi, G., and Shahinpour, M., (1983a).
A Kinetic Model for Rapid Flows of Granular Materials. Int. J. of Non-Linear Mechanics, vol. 19, no. 2, pp. 177-186.

Ahmadi, G., and Shahinpour, M., (1983a).
A Note on Collision Operators in Rapid Granular Flows of Rough Inelastic Particles. Powder Tech., vol. 35, pp. 119-122.

Anderson, T.B., and Jackson, R., (1967).
A Fluid Mechanical Description of Fluidized Beds, I&EC Fundam., Vol. 6, 527-534

Andrews, D.G., and Seifert, H.S., (1971).
Investigation of Particle-Size Determination from the Optical Response of a Laser Doppler Velocitymeter. SUDAAR No. 435.

Angelino, H., Couderc, J.P., Gibert, H., and Laguerie, C., (1974).
Fluidization and Its Application, Proc. Int. Symp., Ste Chimi Industrielle, Paris.

Arastoopour, H., and Shao, S., (1996).
Laser Doppler Anemometry: Application in Multiphase Flow Systems. Lecture Notes, Illinois Institute of Technology, Chicago, Illinois, USA.

Arastoopour, H., and Yang, Y., (1992).
Experimental Studies on Dilute Gas and Cohesive Particles Flow Behavior Using Laser Doppler Anemometer. Fluidization VII, Eds.: Potter, O.E. and Nicklin D.J.

Azario, E., Tadrist, L., Santinini, R., and Pantaloni, J., (1995).
Velocity Analysis of the Solid Phase in Circulating Fluidized Bed. Proceedings of The 2nd International Conference on Multiphase Flow, Vol. 4, '95-Kyoto, April 3-7, 1995, Kyoto, Japan.

Bachalo, W.D., and Houser, M.J., (1984).
Phase Doppler Spray Analyzer for Simultaneous Measurements of Drop Size and Velocity Distributions. Opt. Engineering, Vol. 25, No. 5, pp. 583-590.

Bachalo, W.D., and Houser, M.J., (1985).
Experiments in Polydispersed Two-Phase Turbulent Flows. 2nd. Int. Symp. on Laser Anemometry, Miami, ASME, FED, 33, pp. 135-141.

Bagnold, R.A., (1954).
Experiments on a Gravity-Free Dispersion of Large Solid Spheres in a Newtonian Fluid Under Shear. Proc. Roe. Soc. Vol. A255, pp. 49-63.

Berkelmann, K.G., and Renz, U., (1989).
Applications of Laser Anemometry to Fluid Mechanics, Eds.: R.J. Adrian, T. Asanuma, D.F.G. Durao, F. Durst, J.H. Whitelaw, Spring-Verlag.

Birchenough, A., and Mason, J.S., (1976).
Local Particle Velocity Measurements with a Laser Anemometry in an Upward Flowing Gas-Solid Suspension. Powder Tech., Vol. 14, pp. 139-152.

Boemer, A., (1996)
Consistency of the Granular Multiphase Model, Private Communication.

Burge, S.W., (1991).
FORCE2 - A Multidimensional Flow Program for Gas Solids Flow: Vol. I, User's Guide; Vol II, Theory Guide, Report No. RDD: 91:4911-10-01:01&02, Babcock & Wilcox, Alliance, OH.

Chapman, S., and Cowling, T.G., (1970).
The Mathematical Theory of Non-Uniform Gases. Third edition, Cambridge Univ. Press..

Chen, C.P., (1985).
A Turbulence Closure Model for a Dilute Gas-Particle Flows. The Canadian Journal of Chemical Engineering, vol. 63, pp. 349-360.

Courant, R., Isaacson, E., and Rees, M. (1952).
On the Solution of Non Linear Hyperbolic Differential Equations by Finite Differences. Comm. Pure Appl. Math., Vol. 5, p. 243

Dalla Valle, J.M., (1948).
Micromeiritics, Pitman, London.

Dantec Elektronic (1990).
Phase Doppler Anemometry as Implemented by Dantec, User Guide.

Davidson, J.F., (1961).
Symposium on Fluidization - Discussion, Trans. Inst. Chem. Eng., Vol. 39, pp. 230-232.

Davidson, J.F., and Harrison, D., (1963).
Fluidized Particles, Cambridge: The university Press, London.

Deardorff, J.W., (1971).
On the Magnitude of the Subgrid Scale Eddy Coefficient. Journal of Computational Physics, Vol. 7, pp. 120-133.

De Groot, J.H., (1967).
Proc. Int. Symp. on Fluidization, Netherlands University Press, Eindhoven, pp. 348.

Ding, J., and Gidaspow, D., (1990).
Bubbling Fluidization Model Using Kinetic Theory of Granular Flow. AIChE Journal, Vol. 36, No. 4, pp. 523-538.

Doeblin, E.O., (1990).
Measurements Systems, Application and Design. Mc-Graw Hill.

Driscoll, J.F., and Mann D., (1978).
Submicron Particle Size Measurements in an Acetylene/Oxygen Flame. 3rd Int. Workshop on Laser Velocimetry, Purdue University.

Dunning Jr. J.W., (1967).
Application of Laser Homodyne Spectrometer to Particle Size Measurements. Ph.D. Thesis, School of Engineering, Case Western Reserve University, Cleveland, Ohio.

Durst, F., and Zare, M., (1975).
Laser-Doppler Measurements in Two-Phase Flows. Proceedings of the LDA-Symposium, Copenhagen, pp. 403-429.

Elghobashi, S.E., and Abou-Arab, T.W., (1983).
A two-equation turbulence model for two-phase flow. Phys. Fluids, Vol. 26, no. 4, pp. 931-938.

Ergun, S., (1952).
Fluid Flow Through Packed Columns, Chem. Eng. Prog., Vol. 48, pp. 89-94.

Farmer, W.M., (1972).
Measurement of Particle Size, Number Density and Velocity Using a Laser Interferometer. Appl. Opt., Vol. 11, No. 11, pp. 2603-2612.

Farrell, M., Lun, C.K,K., and Savage, S.B., (1986).
A simple Kinetic Theory for Granular Flow of Binary Mixtures of Smooth, Inelastic Spherical Particles. Acta Mechanica, Vol. 63, pp. 45-60.

Froment, G.F., and Bischoff, K.B., (1990).
Chemical reactor Analysis and Design. Second Edition. Wiley.

Garside, J., and Al_Dibouni, M.R., (1977).
Velocity-Voidage Relationships for Fluidization and Sedimentation, I&EC Proc., Vol. 16, pp. 206-214.

Geldart, D., (1973).
Types of Gas Fluidization. Powder Technology. Vol. 7, pp. 285-295.

Gidaspow, D., (1986).
Hydrodynamics of Fluidization and Heat Transfer: Supercomputer Modelling. Appl. Mech. Rev., Vol. 39, No. 1, pp. 1-23.

Gidaspow, D., (1994).
Multiphase Flow and Fluidization. Continuum and Kinetic Theory Descriptions. Academic Press.

Gidaspow, D., Huilin, L., and Manger, E., (1996).
Kinetic Theory of Multiphase Flow and Fluidization: Validation and Extension to Binary Mixtures. XIXth International Congress of Theoretical and Applied Mechanics. August 25-31, Kyoto, Japan.

Gibilaro, L.G., Di Felice, R., and Waldram, S.P., (1985).
Generalized Friction Factor and Drag Coefficient Correlation for Fluid-Particle Interaction.", Chemical Engineering Science, Vol. 40, No. 10, pp. 1817-1823.

Goldsmith, V.W., (1978).
Measurements in Two-Phase Flow. Proceeding of the Dynamic Flow Conference, pp. 228-319.

Grehan, G., Gouesbet., G., Kleine, R., Renz, U., and Wilhelmi, J., (1982).
Proc. of 3rd International Symposium on Appl. of Laser Doppler Anemometry to Fluid Mechanic, Paper 20.5.

Hardalupas, Y., Taylor, A.M.K.P., and Whitelaw, J.H., (1988).
Depth of Field Considerations in Particle Sizing Using the Phase Doppler Technique. Applications of Laser Anemometry to Fluid Mechanics, Eds.: R.J. Adrian, T. Asanuma, D.F.G. Durao, F. Durst, J.H. Whitelaw, Ladoan Instituto Superior Technico, Lisboa, Portugal.

Hewitt, G.F., (1978)
Measurements of Two Phase Flow Parameters. Academic, New York.

Hishida, K., Maeda, M., Imaru, J., Hironaga, K., and Kato, H., (1984).
Measurements of Size and Velocity of Particle in Two-Phase Flow by a Three-Beam LDA System, Laser Anemometry in Fluid Mechanics, Eds.: R.J. Adrian, D.F.G. Durao, F. Durst, H. Mishina, J.H. Whitelaw, Ladoan Instituto Superior Technico, Lisboa, Portugal.

Hjertager, B.H., (1993)
Numerical Analysis of Multiphase Flows. Lecture Notes, Telemark Institute of Technology, Porsgrunn.

Hjertager, B.H., and Samuelsberg, A., (1992).
Computer Simulation of Flow Processes in Fluidized Bed Reactors. KONA, Powder and Particle, No. 10, pp. 96-103.

Jackson, R., (1963).
The Mechanics of Fluidized Beds: Part I: The Stability of the State of Uniform Fluidization, Trans. Inst. Chem. Eng., No. 41, pp. 13-21.

Jackson, R., (1970).
The Present Status of Fluid Mechanical Theories of Fluidization, Fluidization Fundamentals and Application , Chemical Engineering Progress, AIChE Symposium Series, 66, No. 105, pp. 3-13.

Jackson, T.A., and Samuelsen, G.S., (1988).
Droplet Sizing Interferometry: A Comparison of the Visibility Technique and Phase Doppler Technique. Applications of Laser Anemometry to Fluid Mechanics, Eds.: R.J. Adrian, T. Asanuma, D.F.G. Durao, F. Durst, J.H. Whitelaw, Ladoan Instituto Superior Technico, Lisboa, Portugal.

Jahing, C.E., Grace J.R., and Matsen, J.M., (1980).
Fluidization III Eds. 3, Plenum, New York.

James, R.N., Babock, W.R., and Seifert, H.S. (1968).
A Laser Doppler Technique for the Measurement of Particle Velocity. A/AA Journal, Vol. 6, pp. 160-162.

Jenkins, J.T., and Mancini, F., (1987).
Balance Laws and Constitutive Relations for Plane Flows of a Dense Binary Mixture of Smooth, Nearly Elastic Circular Disks. Journal of Applied Mechanics, Vol. 54, pp. 27-34.

Jenkins, J.T., and Savage, S.B., (1983).
A theory for the rapid flow of identical, smooth, nearly elastic, spherical particles. J. of Fluid Mechanics, Vol. 30, pp. 187-202.

Johnson, K.L., (1985).
Contact Mechanics, Cambridge, UK, University Press.

Kuipers, J.A.M., van Duin, K.J., van Beckum, F.P.H., and van Swaaij, W.P.M., (1993).
Computer Simulation of the Hydrodynamics of a Two-Dimensional Gas-Fluidized Bed. Computers Chem. Eng., Vol. 17, pp. 839-899.

Kunii, D., and Levenspiel, O., (1991).
Fluidization Engineering, Second Edition, Butterworth-Heinemann.

Lahey, R.T., (1995).
CFD Modelling of Phase Distribution and Separation Phenomena, Part 17B, Multiphase Flow and Heat Transfer, Computational Modelling, Swiss Federal Institute of Technology, Zurich, Switzerland, March 20-24.

Lazaro, B.J., (1991).
Evaluation of Phase Doppler Particle Sizing in the Measurement of Optically Thick, High Number Density Sprays, United Technologies Research Center, East Hartford, Connecticut, UTRC91-11

Lebowitz, J.L., (1964).
Exact Solution of Generalized Percus-Yevick Equation for a Mixture of Hard Spheres, The Physical Review, Vol. 133, No. 4A, pp. 895-899.

Lee, S.L., and Srinivasan, J., (1978).
Measurements of Local Size and Velocity Probability Density Distribution in Two-Phase Suspension Flows by Laser Doppler Techniques. Int. Journal of Multiphase Flow, Vol. 4, pp. 141-155.

Lesinski, J., Mizera-Lesinska, B., Fanton, J.C., and Boulos, M.I., (1981).
Laser Doppler Anemometry Measurements in Gas-Solid Flow. AIChE Journal, Vol. 27, No.3, pp. 358-364.

Lun, C.K.K., and Savage, S.B., (1987).
A Simple Kinetic Theory for Granular Flow of Rough, Inelastic Spherical Particles. Journal of Applied Mechanics, Vol. 57, pp. 47-53.

Lun, C.K.K., Savage, S.B., Jeffrey, D.J., and Chepurniy, N., (1984).
Kinetic Theories for Granular Flow: Inelastic Particles in Couette Flow and Slightly Inelastic Particles in a General Flowfield. Journal of Fluid Mechanics, Vol. 140, pp. 223-256.

Lyczkowski, R.W., and Bouillard, J.X., (1989).
Interim User's Manual for FLUFIX/MOD1: A Computer Program for Fluid-Solids Hydrodynamics. Argonne National Laboratory, Report ANLK/ESS-TM-361, Argone, IL.

Ma, D., and Ahmadi, G., (1988).
A Kinetic Model for Rapid Granular Flows of Nearlyelastic Particles Including Interstitial Effects. Powder Tech., Vol. 56, pp. 191-207.

Ma, D., and Ahmadi, G., (1990a).
A Thermodynamical Formulation for Dispersed Multiphase Turbulent Flows I. Int. Journal of Multiphase Flows, Vol. 16, no. 2, pp. 323-340.

Ma, D., and Ahmadi, G., (1990b).
A Thermodynamical Formulation for Dispersed Multiphase Turbulent Flows II. Int. Journal of Multiphase Flows, Vol. 16, no. 2, pp. 341-351.

Manger, E., (1996).
Modelling and Simulation of Gas/Solids Flow in Curvilinear Coordinates. PhD-thesis, Telemark Institute of Technology, Norway.

Mathiesen, V., Solberg, T., Manger, E. and Hjertager, (1996).
Modelling and Predictions of Multiphase Flow in a Pilotscale Circulating Fluidized Bed, 5th International Conference on Circulating Fluidized beds, May 28-31, Beijing, China.

Murray, J.D., (1965).
On the Mathematics of Fluidization Part 1. Fundamental Equations and Wave Propagation, Journal of Fluid Mech., Vol. 22, 57-80.

Ose, S., (1996).
Measurement of Particle Size Distribution, methods and instruments, In norwegian, internal note, Tel-Tek, Kjølnes Ring, N-3914 Porsgrunn, Norway.

Patankar, S.V., (1980).
Numerical Heat Transfer and Fluid Flow. Hemisphere Publishing Corporation.

Patankar, S.V., and Spalding, D.B., (1972).
A Calculation Procedure for Heat, Mass and Momentum Transfer in Three-Dimensional Parabolic Flows. Int. Journal of Heat Mass Transfer, vol. 15, p. 1787.

Pigford, R.L., and Baron, T., (1965).
Hydrodynamic Stability of a Fluidized Bed, I&EC, Vol. 4, 81-87.

Reddy, K.V.S., (1967).
Particle Dynamics in Solid-Gas Flow in a vertical Dust. PhD Thesis, University of Waterloo.

Rowe, P.N., (1961).
Drag Forces in a Hydraulic Model of a Fluidized Bed, Part II. Trans. Inst. Chem., Vol. 39, pp. 175-180.

Ruckenstein, E., and Tzeculescu, M. (1967).
On the Hydrodynamics of Hydrodynamics of the Fluidized Bed. International Symposium on Fluidization, Eidhoven, Ed., A.A.M. Drinkhenburg, Netherlands University Press, 180-188.

Rudd, M.J., (1969).
A New Theoretical Model for the Laser Dopplermeter. Journal of Physics. E: Sci. Instrument Vol. 2, No. 55.

Saffmann, M., Buchhave, P., and Tanger, H., (1984).
Simultaneous Measurements of Size Concentration and Velocity of Spherical Particles by a Laser Doppler Method. Laser anemometry in Fluid Mechanics - II, Eds.: Adrian, R.J., Durano, D.F.G., Durst, F., Mishina, H. and Whitelaw, J.H, Ladoan Instituoto Superior Tecnico, Lisboa, Portugal.

Samuelsberg, A., (1994).
Modelling and Simulation of Fluidized Bed Reactors. PhD-thesis, Telemark Institute of Technology, Norway.

Samuelsberg, A., and Hjertager, B.H., (1996a)
An Experimental and Numerical Study of Flow Patterns in a Circulating Fluidized Bed Reactor. Int. Journal of Multiphase Flow, Vol. 22, No. 3, pp. 575-591.

Samuelsberg, A., and Hjertager, B.H., (1996b)
Computational Modelling of Gas Particle Flow in a Riser. AIChE Journal, Vol. 42, No. 6, pp. 1536-1546.

Sekoguchi, K., Takeishi, M., Kano, H., Hironaga, K., and Nishiura, T., (1982).
Paper 16.1, 1st. Int. Symp. on Appl. of Laser Anemometry to Fluid Mech. Lisboa, Portugal.

Shao, S., and Arastoopour H., (1995).
The Flight Time Technique for Simultaneous Measurements of Particle Flow Parameters using a Laser Doppler Anemometer (LDA). Proceedings of FLUIDIZATION VIII, May 14-19, Tours, France.

Sinclair, J.L., and Jackson, R., (1989).
Gas-Particle Flow in a Vertical Pipe With Particle-Particle Interactions. AIChE Journal, Vol. 35, No. 9, pp. 1473-1486.

Solberg, T., (1994).
A PEA-Algorithm Generalized to M Phases. Private Communication.

Soo, S.L., (1967).
Fluid Dynamics of Multiphase Systems. Blaisdell-Ginn, Waltham, MA.

Soo, S.L., Trzek, G.J., Dimick, R.C., and Hohnstreiter, G.F., (1964).
Concentration and Mass Flow Distribution in a Gas-Solid Suspension. I&EC Fundam. 3, No.2, pp. 98-106.

Spalding, D.B., (1983).
Developments in the IPSA Procedure for Numerical Computation of Multiphase-Flow Phenomena with Interphase Slip, Unequal Temperatures, Etc.", Numerical Properties and Methodologies in Heat Transfer, pp. 421-476, Hemisphere Publishing Corporation.

Spalding, D.B., (1985).
Computer simulation of two-phase flows with special reference to nuclear reactor systems.", Computational techniques in heat transfer, Ed.: R.W. Lewis, K. Morgan, J.A. Johnson and W.R. Smith, Pineridge Press, pp. 1-44.

Squires, A.M., (1986).
Circulating Fluidized Bed Technology. Basu, P. ed., Pergamon, New York.

Syamlal M., and O'Brien, T.J., (1987)
A Generalized Drag Correlation for Multiparticle Systems, Morgantown Energy Technology Center DOE Report.

Syamlal, M., Rogers, W., and O'Brien, T.J., (1993).
MFIX Documentation Theory Guide. Technical Note DOE/METC-94/1004, Morgantown, West Virginia, USA.

Tadrist, L., Azario, E., and Cattieuw, P., (1993).
Analysis of Two-Phase Flow in a Circulating Fluidized Bed, Proceeding, 4th International Conference on Circulating Fluidized Bed, Vol.2, pp. 702-707.

Tadrist,L., and Van den Moortel T., (1996).
Experimental Analysis of the Two-Phase Flow Structures in a Circulating Fluidized Bed by Image Processing. Preprinted for publication, Laboratire de l'Institut Universitaire des Systemes Thermiques Industriels (IUSTI), U.M.R. 139 Universite de Provence - Centre de St Jerome - Case 162, Avenue Escadrille Normandie Niemen 13397 Marseille CEDEX 20 - France.

Tsuji, Y., (1993).
Discrete Particle Simulation of Gas-Solid Flow. KONA Powder and Particle, No. 11, pp. 57-68.

Tsuji, Y., Morikawa, Y., and Shiomi, H., (1984).
LDV Measurements of an Air-Solid Two-Phase Flow in a Vertical Pipe. Journal of Fluid Mech., Vol. 130, pp. 417-434.

Tsuo, Y.P., and Gidaspow, W., (1990).
Computation of Flow Patterns in Circulating Fluidized Beds. AIChE Journal, Vol. 36, no. 6, pp. 885-896.

Van Den Moortel, T., Santini, R., and Tadrist, L., (1996).
Measurement of Local Mass Flux in a Circulating Fluidized Bed Using a Phase Doppler Particle Analyzer: A New Post-Processing Data Algorithm. Proceedings, ASME Heat Transfer Division, Vol. 3, pp. 239-250.

Wen, C.Y., and Yu, Y.H., (1966).
Mechanics of Fluidization, Chem. Eng. Prog. Symp. Series, Vol. 62, pp. 100-111.

Yakhot, Y., and Orszag, S.A, (1986).
Renormalization Group Analysis of Turbulence. 1. Basic Theory. Journal of Scientific Computing, Vol. 1, No. 1, pp. 3-51.

Yang, Y., (1991).
Experiments and Theory on Gas and Cohesive Particles Flow Behavior and Agglomeration in the Fluidized Bed Systems., PhD-thesis, Illinois Institue of Technology, Chicago, Illinois, USA.

Zamankhan, P., (1995).
Kinetic Theory of Multicomponent Dense Mixtures of Slightly Inelastic Spherical Particles. Phys. Rev. E., Vol. 52, No. 5, pp. 4877-4891.

Zenz, F.A., and Othmer, D.F., (1960).
Fluidization and Fluid-Particle Systems, Reinhold, New York.

Zhang, Y.F., (1992).
Particles Flow Behavior in the Riser of a Circulating Fluidized Bed., PhD-thesis, Illinois Institute of Technology, Chicago, Illinois, USA.

Zhang, Y.F., and Arastoopour, H., (1995).
Dilute FCC Particles/Gas Flow Behavior in the riser of a Circulating Fluidized Bed. Powder Tech., Vol. 84, No. 3, pp. 221-229.